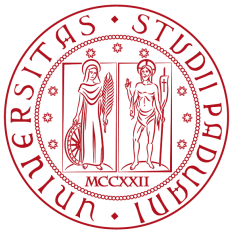

UNIVERSITÀ DEGLI STUDI DI PADOVA

Dipartimento di Fisica e Astronomia “Galileo Galilei”

Corso di Laurea Magistrale in Fisica

Tesi di Laurea

FLUKA Monte Carlo calculations for the design of the NEPIR fast neutron facility at LNL

Relatore

Prof. Riccardo Rando

Correlatore

Prof. Jeffery Wyss

Laureando

Enrico Mazza

Anno Accademico 2018/2019

Contents

1 Abstract

The NEPIR (NEutron and Proton IRradiation) project foresees the construction of a fast neutron (E_n > 1 MeV) irradiation facility at the SPES cyclotron of the INFN Legnaro National Laboratory. The initial configuration of the facility (NEPIR-0) is financed, in an advanced state of design, and construction will start soon. NEPIR-0 will use a relatively simple low power neutron production beryllium target placed inside the existing shield wall that separates the cyclotron hall from the experimental hall. The facility will be immediately used to test microelectronic components and devices and neutron shielding materials. In the final configuration (NEPIR-1) the capability of the facility will be significantly extended by adding an independent target bunker, two new specialized targets (one of which is high power) and a high power beam dump. In this work, the FLUKA Monte Carlo code is used to study the final NEPIR-1 configuration, in particular the propagation, shielding and absorption of the neutrons generated by the new targets and the beam dump. The code is used to evaluate the activation of the air in the experimental hall and the residual dose due to the activation of the targets and surrounding materials. The methods used are then applied to study the imminent initial configuration of NEPIR, in particular the activation of the Be target, the air and the concrete walls of the experimental hall.

2 Introduction

Our electronics and information technology era is characterized by a very fast diffusion of electronic devices in all aspects of everyday life, from the mundane (cell phones, automotive and domotic applications, trivial gadgets) to industrial (automation); from essential (avionics, computers, servers) to even life sustaining (medical devices); and of course the role of electronics in science and space exploration continues to deepen.

The diffusion of electronics in our era has been possible thanks to the miniaturization of components, the reduction of bias voltage and the related energy consumption. However this miniaturization has increased the chances of radiation damage induced by ionizing particles hitting a device. Some radiation induced effects are cumulative so the damage, measured as shifts in device parameters (leakage current, threshold voltage, etc.), worsen as the device is exposed to increasing amounts of radiation. On the other hand, there are Single Event Effects (SEE), stochastic instantaneous anomalous behaviors (temporary or permanent) of devices, caused by a single ionizing particle.

The Commercial Off the Shelf (COTS) electronic products on the market are intrinsically more resistant to cumulative radiation damage effects and this has brought about a more aggressive use of state-of-the-art COTS for applications in extreme or artificial radiation hostile environments, such as in High Energy Physics experiments and Outer Space. However they are potentially more vulnerable to SEE induced by energetic protons and neutrons and this requires tests for the expected levels of radiation; these tests are typically carried out at accelerator-based irradiation facilities.

The issue of radiation damage is traditionally of great interest to the experimental High Energy Physics (HEP) and Space communities. In HEP experiments, semiconductor devices (detectors and frontend electronics) are exposed to very high levels of artificial radiation and need to maintain their functionality over years. In space, outside the protection of the Earth's atmosphere, the radiation environment is also severe: cosmic rays from Sun and galactic sources and trapped particles belts can compromise the electronic systems of the spacecraft, as well as the health of astronauts. But on Earth we are not immune from such problems.

In particular, the effects caused by fast neutrons (E_n > 1 MeV) are gaining more and more attention. Fast neutrons are ubiquitous, very intrusive (very difficult to shield against) and can have profound effects. As they are neutral, they can undergo nuclear collisions with the nuclei of a microelectronic device or in human tissue and generate additional charged particles that

will ionize surrounding atoms and molecules; this in-depth anomalous ionization may then perturb the normal functioning of the microelectronic device or alter the normal biochemical activity of human cells.

Fast neutrons are produced in high-energy nuclear reactions (e.g. proton or ion-induced nuclear breakup and hadron showers; photo-nuclear reactions). They are the problematic part of the prompt and secondary radiation fields at HEP accelerators and experimental halls. Fast neutrons are also unavoidably present in accelerator-based radiotherapy setups where they are produced in the collimators of the beam delivery system and in the body of the patient itself. In Space environments, fast neutrons are produced in nuclear interactions of very high energy Galactic Cosmic Radiation with spacecraft materials, the bodies of astronauts, Lunar/Martian rocks and soils, any shielding materials. On Mars they are also produced in its atmosphere. Indeed, they form a significant component of the radiation fields inside spacecraft and future colonization habitats. But fast neutrons are found in our normal-life Earth bound environments too. They are an important component of cosmic ray air showers produced by very energetic galactic cosmic rays in the upper layers of the Earth's atmosphere. At flight altitudes, air shower fast neutrons can compromise the electronic systems of aircraft and indeed the avionics industry has always been at the forefront of the growing concern of the electronics industry for the effects of air shower neutrons. But some air showers are very energetic and extensive and fast neutrons are found at sea level too and may affect the electronics in sensitive and vital applications that need high levels of reliability (information technology, medical, etc.).

To summarize, fast neutrons are a potential source of problems for both the electronics industry in diverse fields of applications and for radiation health:

- air shower neutrons are problematic for sensitive avionics at flight altitudes and at sea level in high-reliability electronic systems;
- secondary fast neutrons pose a serious health threat for deep space and colonization enterprises;
- in radiotherapy, secondary fast neutrons substantially contribute to the dose deposition in body regions of the patient not at all directly crossed by the actual therapeutical beam (photons, protons, ^{12}C ions) and increase the risk of secondary malignant neoplasms.

Facilities with well-characterized fast neutron fields are needed to study the physics of neutron interactions in these applications, in particular concerning dosimetry, radiation protection and neutron-induced SEE effects in avionics and sensitive electronics.

The study of neutron-induced SEE in commercial electronics is of strategic importance, not only for avionics, but for digital electronic industries that are increasingly flooding the market with memory and logic components. Neutron-effect studies, tests and validations of industrial electronics are now typically carried out at accelerator-based facilities where high intensity neutron beams are available: here a short irradiation time is sufficient to reproduce the effects of a much longer radiation exposure in the natural environment.

The SPES[1] project at the INFN Legnaro National Laboratory (LNL) with a high current variable energy cyclotron opens the possibility to build in Italy a facility dedicated to neutron-induced SEE studies on electronics. The proposed NEPIR (NEutron and Proton IRradiation) facility is based on two different neutron production targets to generate high flux neutron beams for different applications. One multipurpose target system will produce a Quasi Mono-energetic Neutron beam (QMN) with controllable energy peak in the 20-70 MeV range. The second specialized target will produce a fast neutron beam with a continuous energy distribution which, in the accessible energy range (cyclotron cutoff 70 MeV), resembles that of atmospheric neutrons, air-shower neutrons naturally present at sea-level. Direct proton irradiation is also foreseen to study the effects of solar protons.

NEPIR has been partially funded within the Italian SPARE (Space Radiation Shielding) project. Health risks due to cosmic radiation are a major showstopper for safe colonization and shielding is the only practical countermeasure, but it is poorly effective against very high energy nuclei from galactic sources. SPARE consists in a test campaign of shielding materials using high energy protons and QMN neutrons at the complementary accelerator facilities in Trento (TIFPA) and LNL (NEPIR). Since the available funds from SPARE are insufficient to complete the construction of NEPIR, a phase-0 version with a single target is under design. The NEPIR-0 target will produce a high flux of neutrons with a continuous energy spectrum with a small proton current.

This thesis work concerns part of the radiation protection issues related to the construction of the NEPIR facility: activation of air and irradiated materials, sizing of collimators and shielding systems.

[1] Selective Production of Exotic Species

3 Fast Neutrons effects in electronics

3.1 Radiation damage in electronics: Single Event Effects

Radiation damage in electronic semiconductor devices occurs when some energy is released inside it in the form of atomic displacement and/or ionization. Displacement Damage Dose (DDD) effects in the semiconductor bulk or Total Ionization Dose (TID) effects in the insulator layers and interfaces are cumulative, whereas Single Event Effects (SEE) have a stochastic nature.

Single Event Effect is a collective term to gather many possible effects caused by a single energetic particle that strikes an electronic device. In the classification of SEE there is a first distinction in soft errors and hard errors: the former cause non-destructive effects, temporary and reversible (like loss of information and/or control) whereas the latter lead to catastrophic device failure and permanent physical damage (destruction). Soft Errors, also called Single Event Upsets (SEU), can be recovered from in different ways: some by simply rewriting the data using software or hardware mitigation solutions, while some may require more substantial actions such as power cycling.

In digital electronics, a Soft Error (SE) will occur when the amount of charge produced by any ionizing particle, collected at a junction or sensitive node, is larger than the information carrying charge stored in the device. A single proton or fast neutron (E_n > 1 MeV) may induce a SEU after an interaction with a constituent nucleus of the device which recoils or breaks up in ionizing fragments (Figure 3.1). If boron-10 atoms are present, for example, the capture of very slow thermal neutrons is very likely to cause Soft Errors (SE) too; the thermal neutron capture reaction $^{10}B(n,\alpha)^{7}Li$, gives rise to two ionizing particles that lose all their energy in a path of a few microns in silicon (Figure 3.2).

This thesis work will focus on Soft Errors as NEPIR will focus on them. They are of primary concern for commercial digital terrestrial applications: at sea level, atmospheric neutrons may induce SE and consequent failure rates higher than all other reliability mechanisms combined. Important hard SEE such as Latch-up (SEL), Burnout (SEB) and Gate Rupture (SEGR) require high energy neutrons (E_n > 100 MeV) and are usually not observed at compact neutron source facilities like NEPIR.

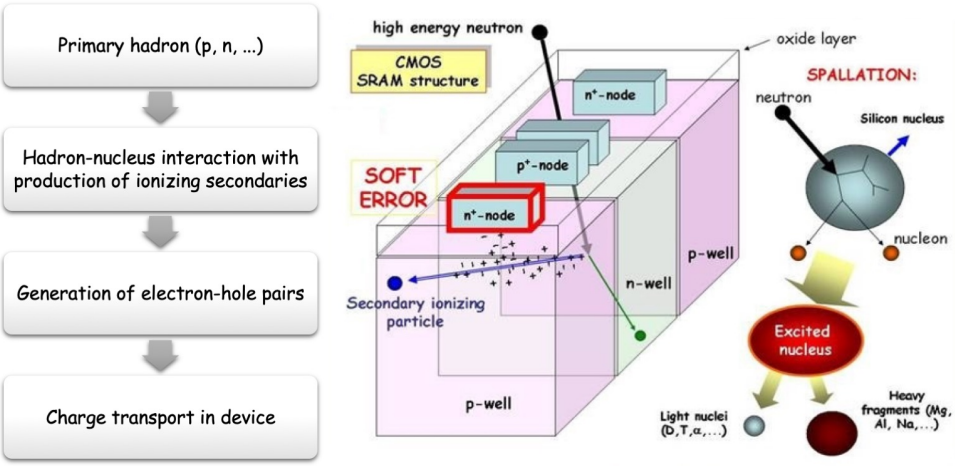

Figure 3.1 Schematic representation of the mechanism a neutron can induce a SEU in a CMOS memory cell: a nuclear interaction produces charged particles that can deposit charge in sensitive volumes. If the deposited charge is large enough, it can alter the electrical behavior of the device.

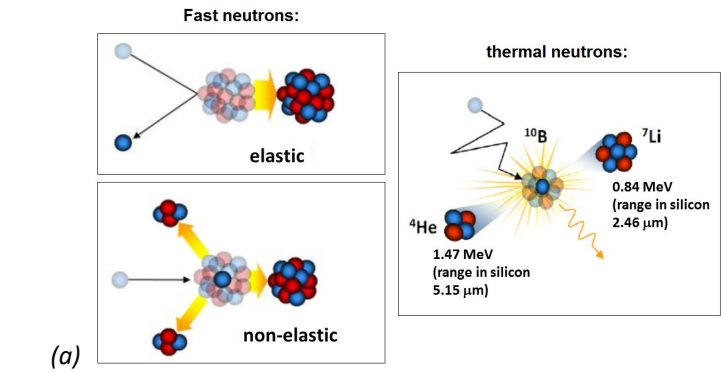

(a)

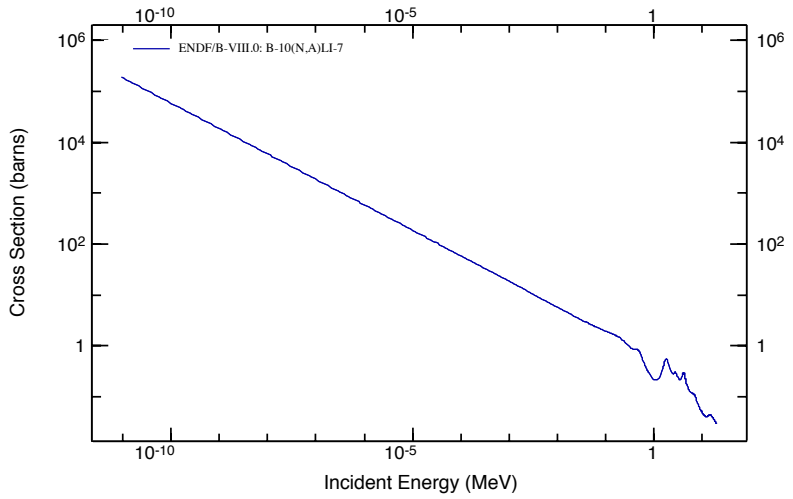

(b)

Figure 3.2 (a) Typically only a fast neutron can cause a SEU if some recoiling fragments deposit enough charge near a sensitive volume. In presence of ^{10}B atoms a slow neutron can very likely induce a break-up reaction with the production of two ionizing fragments that can cause SEE, too. (b) Cross-section as a function of energy for the reaction $^{10}B(n,\alpha)^{7}Li$.

3.2 SEE cross-section

Fast neutrons induce SEE indirectly. SEE are stochastic events: the sensitivity of a device to a specific type of SEE is a probability expressed as a cross-section σ (cm^2) that depends on the energy of the incident neutron (Figure 3.3).

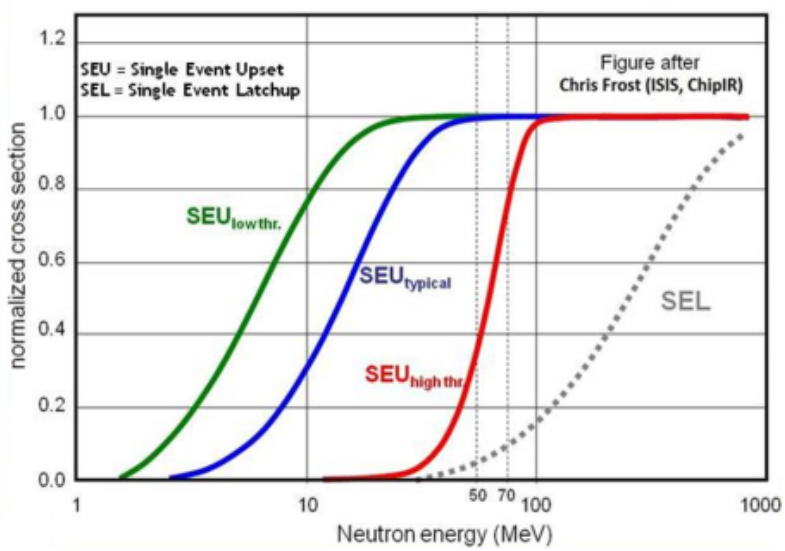

Figure 3.3 Typical cross-section curves describing the sensitivity of a device to different kinds of neutron induced SEE. A reference value for plateau SEU cross-sections is $\sigma_P = 10^{-14}$ cm^2/bit (Chris Frost, 2010 LNL-workshop).

The mechanisms involved in a SEE in a device are threshold phenomena. The energy dependent cross-section function σ(E) is described by four parameters: the threshold energy E_{thr}, the saturation cross-section σ_p and two shaping parameters W and S to better fit the experimental data. It is generally called Weibull function:

$$\sigma(E) = \sigma_p\left\{1 - \exp\left(-\left(\frac{E - E_{thr}}{W}\right)^S\right)\right\}$$

In Figure 3.4 are shown the normalized Weibull curves for a range of values of the fitting parameters. The QMN system of NEPIR (described in section 8.5) will deliver quasi mono-energetic neutrons with energy peaks in the 20-70 MeV range. Devices with a threshold lower than 20 MeV can be characterized if the shaping parameters allow enough experimental points to extrapolate a good fit to a Weibull curve[2].

[2] At the 15 MV Tandem of Legnaro, it might be possible to produce directional and kinematically focused neutrons, effectively monochromatic with energies below 20 MeV, by using the inverse reactions. The reaction $p(^{11}B,n)^{11}C$ is routinely used at the Tandem in Munich (Germany). However, for SEE applications, the achievable neutron flux is a crucial aspect. This interesting possibility is presently under investigation.

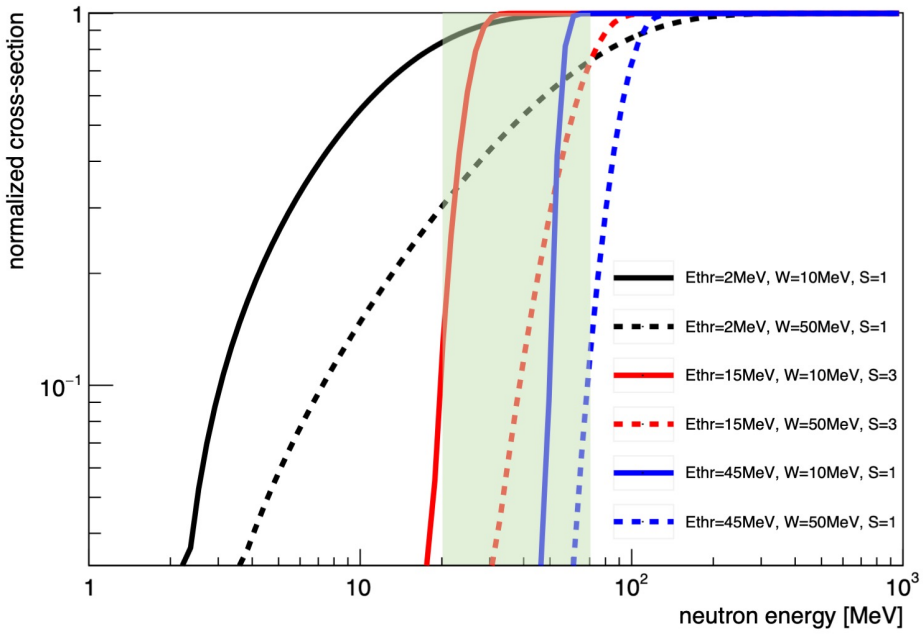

Figure 3.4 Examples of normalized Weibull curves with different values of the shaping parameters; the green area indicates the QMN energy range at NEPIR. Also a device with threshold lower than 20 MeV can be characterized if enough experimental points are available to extrapolate a good fit of its Weibull curve.

In an irradiation test, the neutron SEE cross-section σ(E) is evaluated as the number of SEE observed divided by the fluence Φ(E) of incident neutrons of the corresponding energy:

$$\sigma_{dev}(E) = \frac{N_{SEU}}{\Phi(E)}$$

Ideally, with neutrons of well-defined energy, it is possible to reconstruct the Weibull cross-section curve that completely characterizes the SEU response of a given device. However, as the name suggests, the quasi mono-energetic neutrons of NEPIR are not perfectly monochromatic, but there are established techniques to estimate the number of SEU due to wrong energy neutrons and correct the raw data.

In general, to predict the Soft Error Rate (SER) of a digital device in the field, the cross-section is weighted by the neutron energy distribution of the particular environment in which the device is operated. The SER is then expressed in units of FIT (Failure In Time). One FIT is equivalent to one failure in 10^9 device-hours.

At sea level, the integral flux of fast neutrons produced by cosmic rays is

$$\Phi(E_n > 1\,\mathrm{MeV}) = 21\,\mathrm{n/cm^2/h}$$

If the cross-section curve of the sensitive nodes (bits) of a digital device is known, the SER of a Mbit device induced by neutrons can be calculated according to the following expression:

$$(\mathrm{FIT/Mb})_{\mathrm{atm\text{-}sea}} = (10^6\,\mathrm{bits})(10^9\,\mathrm{h}) \int_{E_{thr}}^{\infty} \sigma_{\mathrm{bit}}(E)\,\phi_{\mathrm{sea}}(E)\,dE$$

where $\phi_{sea}(E)$ is the neutron differential energy spectrum at sea level. As an example, considering a device with a fictitious step-function cross-section per bit of $\sigma_{bit} = 5\times10^{-14}$ cm^2/bit with a 10 MeV threshold, being ≈13 n/cm^2/h the integral flux of atmospheric neutrons above threshold, the FIT/Mb of this device is equal to FIT/Mb = 650.

A typical SE failure rate for a digital component can be about 1-50 FIT and the overall SE failure rate of an integrated circuit may be 50-200 FIT/chip. However, due to the very high density of sensitive nodes in a complex chip, the SER can easily exceed 50,000 FIT/chip without mitigation, which corresponds to about one SE in two years assuming 24 h/day operations.

Industrial standard facilities for testing commercial products produce intense neutron beams with continuous energy spectra that variously resemble the energy spectrum of atmospheric neutrons present at sea level that extends beyond 1 GeV. However more than 60% of fast atmospheric neutrons have energies below 50 MeV. Just a couple decades ago, the minimum recommended neutron energy for soft error (SEU) testing was 20 MeV. As of 2006 the Joint Electron Device Engineering Council (JEDEC) recommends testing with neutrons below 10 MeV too [1]. Indeed, as sensitive nodes have become smaller, modern digital devices and systems are sensitive to neutrons in the 1-10 MeV energy range with neutron threshold energies for soft errors close to the thresholds of the nuclear reactions at the origin of the errors.

3.3 Sea-level neutrons from cosmic rays

The charged cosmic radiation that reaches the Earth atmosphere consists of different components: 98% of nuclei (divided in 88% protons, 11% alpha particles and about 1% heavier nuclei) and 2% of electrons. The energy of nuclei ranges up to over 10^{14} MeV.

When cosmic rays reach the upper atmosphere, they undergo nuclear spallation and evaporation processes with the nuclei of the upper atmosphere (nitrogen, oxygen, carbon dioxide, rare gases) to produce extensive air-showers, cascades of secondary light particles including protons, neutrons, electrons, photons, muons, pions, kaons (and even exotic particles), that can reach the surface of the Earth (Figure 3.5). All the neutrons produced by the interactions of cosmic rays in the atmosphere are called “Atmospheric Neutrons”.

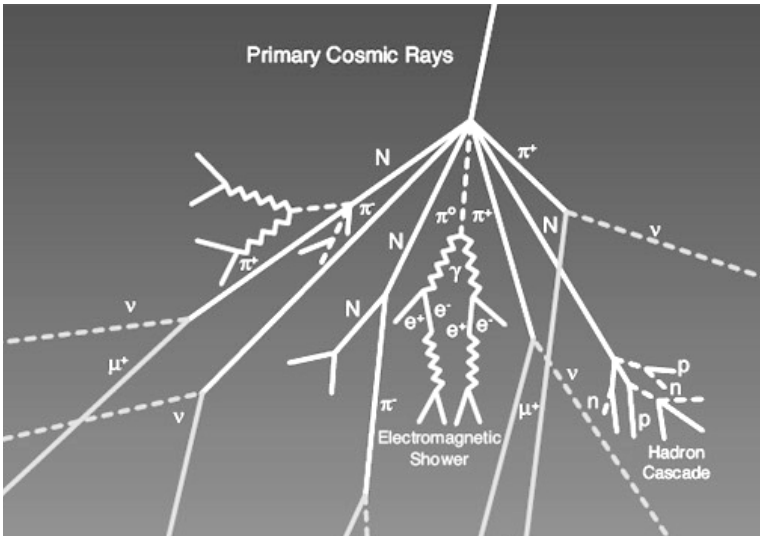

Figure 3.5 Air-showers induced by cosmic rays. Neutrons are produced in hadronic cascades.

The atmosphere attenuates both the cosmic rays and the atmospheric neutron flux. The variation of the neutron flux with altitude comes from the competition between various production and removal processes: the result is a maximum in the flux at about 18000 m, called the Pfotzer maximum. Typical commercial airliners operate up to about 12000 m, where the flux density is in the range of 300 to 450 times greater than at sea level, resulting in greater incidences of SEEs for avionic equipment compared to similar ground-based equipment.

Although altitude is the largest single factor driving atmospheric neutron flux, latitude is also important. Cosmic rays are deflected more strongly near the equator since the lines of geomagnetic field are parallel to the surface of the Earth and hence the bending of trajectories of the primary particles depends on the geomagnetic latitude on the Earth. This effect is responsible for a six-fold increase in flux between equatorial latitudes and the polar regions.

The neutron flux is also modulated by solar activity and solar eruptions. When the solar magnetic field is stronger, the paths of the charged primary cosmic particles are bent more and fewer reach the Earth, so a maximum in the solar activity causes a neutron flux minimum and conversely.

Figure 3.6 shows the sea level neutron differential energy spectrum for neutrons with $E_n > 1$ MeV [2]: this spectrum is the standard reference used by the JEDEC, an independent semiconductor engineering trade organization and standardization body. The energy spectrum extends from thermal energies up to 10 GeV and is the product of three different generation processes: a thermal energy peak, an evaporation peak around 1 or 2 MeV and a spallation peak centered around 100 MeV and extending up to about 10 GeV.

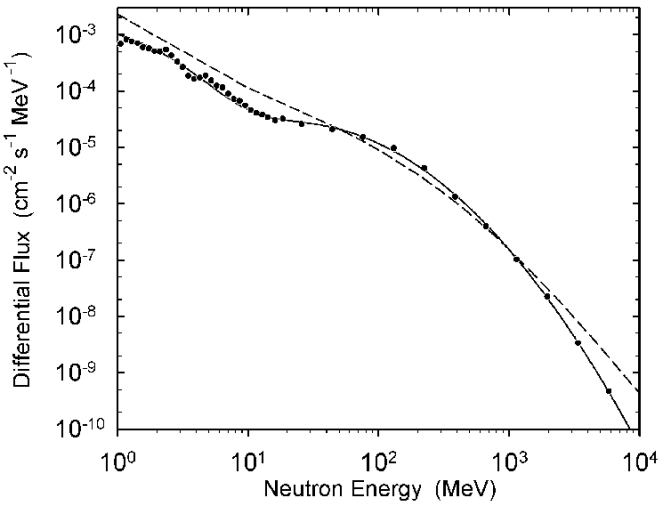

Figure 3.6 The black curve (fitted to data points [2]) is the JEDEC 2006 reference differential energy spectrum of fast (E_n > 1 MeV) atmospheric neutrons at sea level (New York city, mid-level Solar activity, outdoors); 65% of them are in the 1-65 MeV energy range.

3.4 Neutron test facilities

The most direct way to determine the SER due to atmospheric neutrons of a given device is to perform a field test: expose the device (or many identical ones) to the terrestrial radiation and wait for soft-errors with relevant statistics. The availability of compact proton accelerator gives the possibility to produce intense beams of neutrons: testing a device in this artificial neutron field will greatly shorten the time to observe a significant number of SEE. At these facilities, energetic protons are directed onto specially designed neutron production targets where nuclear spallation reactions take place. Nuclear reactors are also typical neutron sources for academic studies, but they are of limited interest for SEE tests because the continuous energy spectrum of reactor neutrons does not reach the threshold energy.

Two types of neutrons sources for SEE testing can be distinguished:

- broad-band, continuous energy spectrum facilities, that use thick targets to produce an energy spectrum as similar as possible to that of the atmospheric neutrons;
- narrow band, quasi mono-energetic (discrete) neutron sources using thin lithium or beryllium targets.

The experimental methods to determine the susceptibility of electronics to atmospheric neutrons are summarized in Table 3-1 (after E. Ibe).

Type of irradiation	Experimental procedure	Merits/demerits
Neutron Field Tests	Keep a large number of Devices Under Test (DUT) at a certain location for a long time. To speed things up, the tests are performed onto high mountains.	Expensive, time consuming. Realistic and reliable. Few corrections necessary (related to altitude and location). No sensitivity to energy dependence.
Mono-energetic neutrons	Irradiate the DUT with mono-energetic neutrons produced from protons on thin Li or Be targets. Vary energy of the incident protons to study energy dependent effects.	Facilities limited. Versatile, interdisciplinary. Actually, the neutrons are only quasi mono-energetic; corrections are necessary to account for significant fraction of neutrons with wrong energy.
Spallation Neutrons	Irradiate the DUT with neutrons with a broad energy spectrum produced from protons on a thick target. Moderators are then used to shape the neutron spectrum.	High fluxes. High-energy facilities are limited. No sensitivity to energy dependence. Continuous (white) spectrum needs to be somewhat similar to the atmospheric one.
Reactor Neutrons	Irradiate the DUT with thermal neutrons at experimental reactors.	Facilities limited (research reactors are phasing out). Very low usefulness for fast (E_n > 1 MeV) neutron SEE testing due to a great difference in neutron spectra with atmospheric one. Useful for testing for SEE due to thermal neutron capture by any ^{10}B in the device.
Proxy mono-energetic protons	Irradiate DUT with mono-energetic protons. Vary the energy of the protons to study energy dependent effects.	Many facilities are available. However, there is only pseudo equivalence with neutrons total ionization dose effects in DUT.

Table 3-1 Experimental methods to study the sensitivity to atmospheric neutrons of electronic devices.

3.4.1 Continuous energy spectrum facilities

Thick broad-band production targets, made of heavy elements such as tungsten, provide neutrons with a continuous range of energies (white energy spectrum). The primary proton beam is completely stopped inside the target with considerable amount of delivered power. The main goal of these facilities is to obtain the best similarity between the produced neutron spectrum and the atmospheric one. In this regard, the cutoff energy is set up by the maximum proton energy available at the accelerator, so the main challenge remains the shaping of the spectrum, which represents an important figure of merit of the facility.

In these accelerator-driven facilities, the neutron flux can reach intensities 10^9 higher than the natural one: the SER can be of the order of 1 error/second, a great advantage to collect statistics in a short amount of time. The measured SER value of a *Mbit* device at a continuous energy neutron irradiation facility is

$$(\mathrm{SER/Mb})_{\mathrm{acc}} = (10^6\,\mathrm{bits}) \int_{E_{thr}}^{E_{cutoff}} \sigma_{\mathrm{bit}}(E)\,\phi_{\mathrm{acc}}(E)\,dE$$

where $\phi_{acc}(E)$ is the neutron differential energy flux at the facility and E_{cutoff} is the highest neutron energy the generator can deliver. If the shape of the neutron energy spectrum is very similar to the atmospheric reference, $\phi_{acc}(E) \approx F \times \phi_{sea}(E)$ where *F* is called the acceleration factor.

The worldwide facilities that furnish fast neutrons with continuous energy spectra for SEE studies and reliability tests are here listed and then compared in Table 3-2.

- The ICE House at Los Alamos Neutron Science Centre (LANSCE) in New Mexico, USA, is probably the best broadband source in the world (with energies up to 800 MeV) with a white atmospheric-like spectrum, but limited thermal neutron flux.
- Tri-University Meson Facility (TRIUMF) at the University of British Columbia, Canada, has a high flux atmospheric-like spectrum (up to 450 MeV), but with limited accessibility for electronic components testing and a lower flux large area source suitable for large devices and systems testing.
- The Svedberg Laboratory (TSL), now closed[3], at Uppsala University in Sweden had a standard acceleration factor of 3×10^8 produced from a simple 24 mm thick target (ANITA facility).
- ISIS CHIP-IR at the Rutherford Appleton Laboratory, United Kingdom: it delivers a fast neutron spectrum that mimics the atmospheric one up to hundreds of MeV, with an acceleration factor F = 10^9. There will be two modes of operation: a collimated neutron beam within a containment blockhouse (this is a standard approach adopted also by other facilities) and a beam line that additionally provides a large, reasonably isotropic flood of neutrons by using additional movable secondary scatterers. The last option will be unique to Chip-IR allowing very large systems (up to 1 m in diameter), completely powered and monitored, to be verified for SEE tolerance at extreme radiation levels.

Facility	**LAB**	**Country**	**Neutron flux (n/cm^2/s) E_n>10 MeV[4]**	**Cut-off energy (MeV)**	**STATUS**
LANSCE ICE House	LANL	USA	4×10^5	800	Operating
TNF	TRIUMF	Canada	3×10^6	500	Operating
ANITA	TSL	Sweden	$10^1\div10^6$	180	Closed
ISIS Chip-IR	RAL	UK	$10^6\div10^7$	800	Operating

[3] Its old accelerator, used primarily for proton therapy, was shut down because of running costs in 2015, when a new proton therapy accelerator center was opened.

[4] The flux of neutrons with energy higher than 10 MeV reported in column 4 is still occasionally quoted in tables like this, but it is now inadequate because of lower threshold sensitivities in modern microelectronic devices (in the range 1-10 MeV).

SNS RID	ORNL	USA	$10^7 \div 10^8$	1000	Proposed
European Spallation Source (ESS)	LUND	Sweden	up to 2×10^8	2500	Proposed
NEPIR (ANEM)	LNL	Italy	up to 5×10^6	70	Proposed

Table 3-2 List of white spectrum neutron facilities worldwide.

Figure 3.7 shows the differential neutron spectra for neutrons with $E_n > 1$ MeV at the mentioned neutron irradiation facilities: none of those facilities do more than approximate the atmospheric neutron spectrum. Figure 3.7 also shows the energy spectrum of Atmospheric Neutron EMulator (ANEM), the neutron production target under development for the final configuration of NEPIR. The ANEM target is optimized to produce an intense beam of fast neutrons with a very atmospheric-like energy spectrum in the 1-65 MeV energy range (cyclotron cutoff at 70 MeV), interval that comprises ≈65% of the atmospheric neutrons with energies greater than 1 MeV. Acceleration factors higher than $F = 1\times10^9$ will be accessible: this corresponds to a neutron integral flux of $\Phi \approx 4\times10^6$ n/cm^2/s in the 1-65 MeV energy range and implies that 1 hour of irradiation is equivalent to an exposure of about 300-400 years at flight altitudes and more than 10^5 years at sea level. Large acceleration factors are useful to well measure the sensitivity of high reliability components and systems with small cross-sections, especially those produced in very large numbers more typical of commercial ground-based electronics industry.

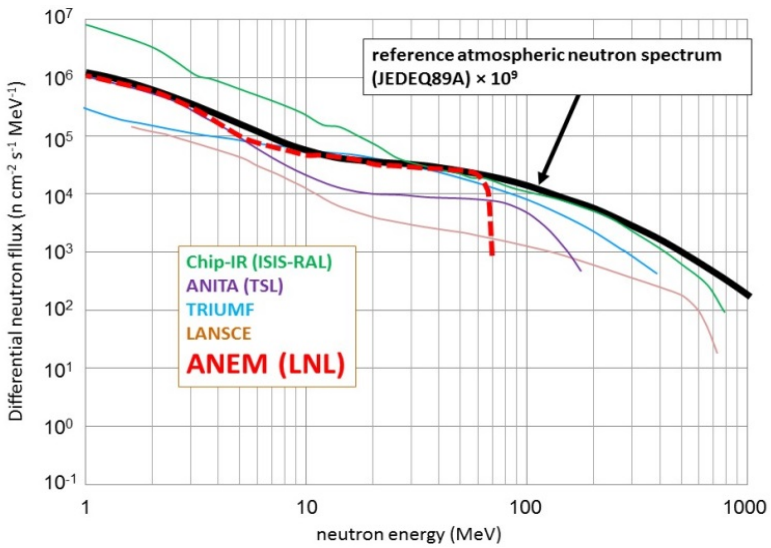

Figure 3.7 The neutron differential energy spectra at facilities used for accelerated neutron SEE testing. The JEDEC reference spectrum multiplied by an acceleration factor $F = 1\times10^9$ is the black curve. In red, the expected neutron differential flux at the NEPIR facility for 3 μA proton current, 3 m downstream the production target.

3.4.2 Discrete energy spectrum facilities

Mono-energetic protons or quasi mono-energetic neutrons (QMN) are used to directly measure the energy dependence of the SEE cross-section: as already mentioned, the characterization of the Weibull curve of a device, by precisely fitting the data points corresponding to different QMN peaks, allows to predict the SER in any neutron field.

QMN reference field facilities are few and difficult to access: at present, there are four working facilities worldwide [3]: three of them are in Japan (TIARA, CYRIC, RCNP) and one in South Africa (iThemba Labs). A fifth facility, NFS, limited to energies below 40 MeV, is under construction at GANIL (France). The one in Sweden (TSL, in Uppsala) was closed in 2015.

Energetic QMN fields are produced using thin lithium and beryllium targets, according to the reactions ^{7}Li(p,n) (Q-value -1.64 MeV) and ^{9}Be(p,n) (Q-value -1.85 MeV). The protons that pass through the thin targets without causing nuclear reactions are magnetically deflected towards a beam dump.

The resulting neutron energy spectrum in the forward direction is not purely mono-energetic: it does present a high energy peak close to the energy of the incoming proton, but also a broad distribution of neutrons at lower energy (tail) coming from nuclear breakup (see for example Figure 3.8). However, the fraction of high-energy neutrons in the mono-energetic peak decreases rapidly with angle, while the continuous tail of low energy neutron changes much less. This characteristic angular dependence can be used to correct raw data taken in the forward direction by subtracting data obtained at larger angles using some sort of multi-angle collimator [4].

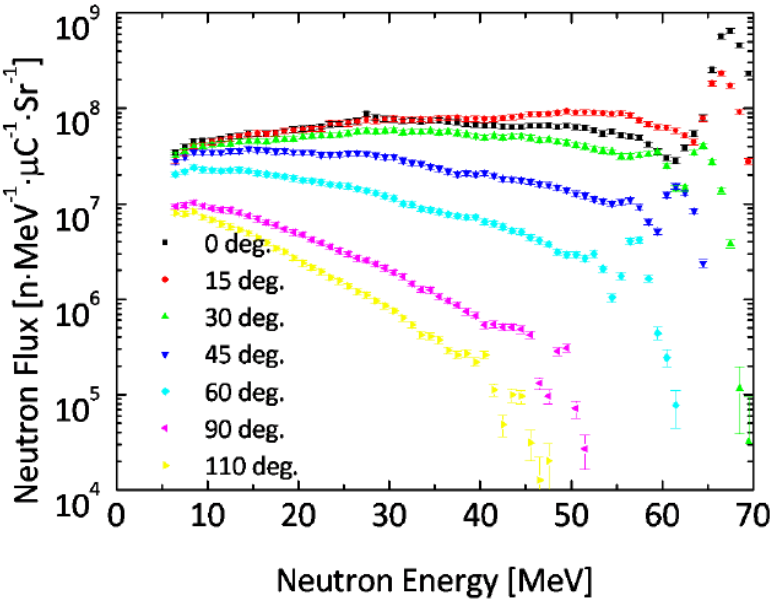

Figure 3.8 Experimental neutron differential energy spectra at different angles for the ^{7}Li(p,n) reaction with a thin target [5].

Facility	Proton energy range (MeV)	Peak neutron flux at test point (n/cm^2/s)	Collimator angles (deg)	STATUS
TYARA (Japan)	40 – 90	10^3	0	Operating
CYRIC (Japan)	14 – 80	10^6	0	Operating
RCNP (Japan)	100 – 400	10^4	0-30	Operating
iThemba (South Africa)	25 – 200	10^4	0-4-8-12-16	Operating
NFS (France)	1 – 40	10^7	0	Under construction
TSL (Sweden)	25 – 200	10^5	0	Closed
QMN (LNL)	20 – 70	10^5	Multi-angle	Proposed

Table 3-3 List of quasi mono-energetic neutron facilities worldwide.

4 Biological effects of fast neutrons

The human exposure to radiation is dangerous but inevitable, indeed on the Earth there are several sources of so called “natural radiation”, the main being natural radioactive isotopes and cosmic rays.

Different types of radiation interact with a material by different mechanisms; understanding these mechanisms is fundamental in order to estimate the induced damage in living tissues: moreover, organs can show different sensitivity to radiation. When radiation traverses a tissue, energy will be transferred to the electrons, atoms will be ionized or excited and this will initiate the chain of events that may lead to a biologic change: this process is called “direct action” and is dominant for particles with high linear energy transfer LET, such as ions and alpha particles, both direct or produced by neutrons. Alternatively, the incoming radiation can interact with other molecules in the cell (mostly water) producing free radicals (H_2O^+, H^+, OH^-, etc.) that can diffuse far away from the site of their production and damage critical targets: the latter process is called “indirect action” (Figure 4.1).

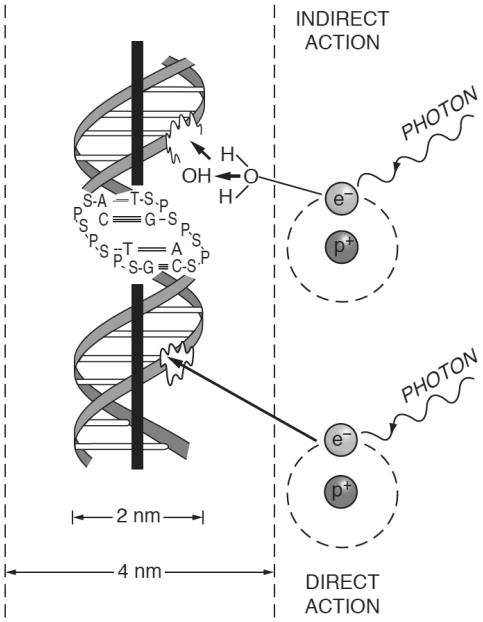

Figure 4.1 Direct and indirect action of radiation. DNA helix has a diameter of 2 nm: it is estimated that free radicals produced in a cylinder of 4 nm diameter can affect the DNA [6].

Cellular damage can prevent the cell from surviving or can modify it, retaining this change as legacy of the radiation exposure: these two possible outcomes have very different implications. Since a large loss of cells can undermine tissue functionality, the probability of such harm has a threshold and then increases with dose and the severity of the induced harm also increases with

dose: these effects are said to be deterministic. Otherwise mutations of living cells increase with dose with no threshold, but the severity of cancer is not dose-related: these are called stochastic effects. This somewhat mirrors the damage to electronics: there are predictable, incremental Total Ionization Dose and Displacement Damage Dose effects due to the cumulative effects of direct ionization and lattice displacement respectively, and there are stochastic, unpredictable Single Event Effects due to a single highly ionizing particle or a chance nuclear reaction.

Apart from natural radiation environment on the Earth which assures low levels of dose (otherwise life would have not developed), radiation exposure imposes strict limits in the design of physics experiments with accelerated beams, requiring the design of specific shielding solutions to allow safe conditions to operators and citizens around the site. At the same time, the growing interest in space missions outside the protective shields of the terrestrial magnetic field and atmosphere requires to carry on advanced studies on shielding techniques for different radiation environments, both for electronics and for astronauts.

5 Radiation environment at accelerator facilities

Charged particles kinetic energies greater than 10 MeV have enough energy to overcome the nuclear Coulomb barrier of many common materials, consequently particle accelerators with such energies will produce some induced radioactivity as a result of the interaction of the primary beam particles and any energetic secondary particles – the prompt radiation – with materials of the accelerator (beam pipe, slits, beam stoppers, targets) and the surroundings (air, concrete). This induced radiation field can remain long after shutoff of the primary beam: its precise characteristics will depend upon many factors such as the particle type, the beam intensity and materials irradiated by the primary beam and secondary radiation.

The properties of this remnant radiation field need to be carefully evaluated to correctly comply with laws on radiation protection for situations such as:

1. The exposure of personnel in the building when the accelerator is not operating;
2. The exposure of experimentalists who need to access the experimental hall;
3. The exposure of personnel for maintenance purposes;
4. The environment into which radioactive contaminants particularly in gaseous or liquid form may be generated;
5. The disposal of unwanted components.

The largest contribution to personnel dose arises from maintenance work near beam dumps, targets, collimators and generally near objects directly hit by the primary beam or located close to a beam loss point. External or internal exposure to radiation from induced radioactivity can also occur in connection with handling, transport and storage of irradiated items. Secondary radiation can also activate air, water and other fluids. The radiation exposure of personnel can be minimized by a combination of good design, online monitoring and planning.

5.1 Radiation exposure: quantities and regulations

Radiation exposure is regulated by law that usually follows directions from the International Commission on Radiological Protection (IRCP): the reference Italian law is D. Lsg. 230/95 and subsequent modifications (D. Lsg. 241/00). There also exists a more recent European law (Council directive 2013/59/EURATOM of 5 December 2013), but at the time of writing it has not yet been implemented into the national Italian legislation.

The objectives of a radioprotection system are to prevent deterministic effects and minimize risks of induced stochastic effects, considering social and economic factors. At the same time, it defines the operational quantities for dosimetry measurements.

The energy deposition by a primary particle in a medium can be described by the following quantities:

1. *Stopping power* S is the energy loss over a unit path length;
2. *Linear energy transfer* LET is the energy imparted to the medium near the site of the collision, so e.g. it differs from the stopping power when bremsstrahlung radiation carries away part of the energy lost by the particle;
3. *Kerma* (kinetic energy released in material) is the amount of energy transferred by uncharged incoming particles such as neutrons to charged particles per unit mass of the medium.

A wide variety of different quantities have historically been used to evaluate the radiation level, the ones used in this work are reported below.

1. *Activity* A: the number of disintegration per unit time of a radioactive nucleus, measured in Becquerel (1 Bq = 1 disintegration/s);
2. *Absorbed dose* D: the amount of energy deposited in a medium per unit mass, measured in Gray (1 Gy = 1 J/kg).
3. *Dose equivalent* in a tissue H_T is defined as $H_T = \sum_R W_R \, D_{T,R}$ where the weighted summation is over different type of radiation, $D_{T,R}$ is the absorbed dose and W_R is a weighting factor which characterizes the damage associated with each type of radiation (see Table 5-1). This quantity is chosen as representative of the relative biological effectiveness (RBE) of a given type of radiation and it is measured in Sievert (1 Sv = 1 Gy * W_R).

Radiation type	**Weighting factor W_R**
Photons	1
Electrons and muons	1
Protons > 2 MeV	5
α particles, fission fragments, heavy ions	20
Neutrons	See Figure 5.1

Table 5-1 Weighting factors for different type of radiation (D. Lgs. 241/00).

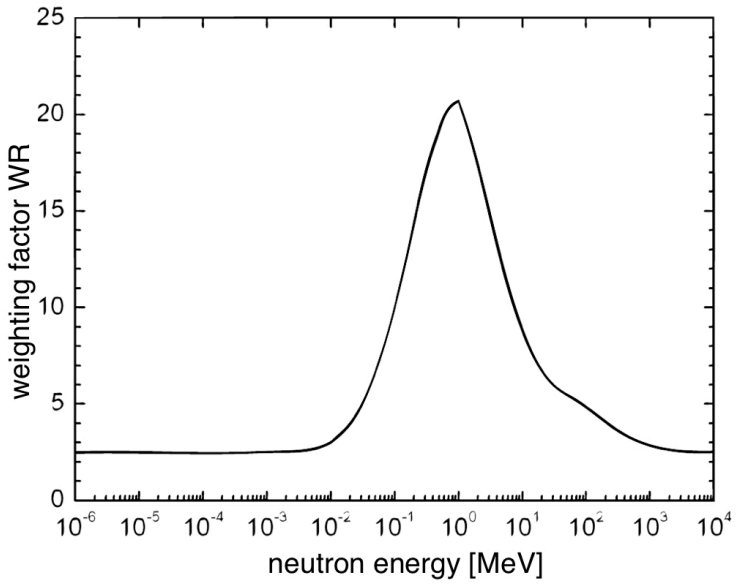

Figure 5.1 Neutron radiation weighting factor W_R as a function of the neutron energy according to the latest International Commission of Radiological Protection recommendations [7]. The most dangerous neutrons are considered those with energy around 1 MeV.

4. *Effective dose* E is defined as $E = \sum_T W_T \, H_T$ where the summation is over all human tissues, H_T is the equivalent dose in a tissue and W_T is a tissue-specific weighting factor which represents the relative contribution of each tissue to the total detriment resulting from uniform irradiation of the body (Table 5-2).

Tissue	**Weighting factor W_T**
Gonads	0.20
Lung, stomach, colon, bone marrow	0.12
Thyroid, esophagus, bladder, breast, liver and remainder	0.05
Bone surface, skin, brain, and salivary glands	0.01

Table 5-2 Tissue weighting factors. Remainder means: adrenals, brain, extrathoracic tissue, kidneys, muscle, pancreas, small intestine, spleen, thymus, uterus (D. Lgs. 241/00)[5].

The Italian law prescribes limits on equivalent dose in some tissues to prevent localized deterministic effects and on effective dose to account stochastic effects. Moreover it considers the difference between people working in radiation environment (divided in two categories) and

[5] ICRP recommendations revised weighting factors in 2007: most notable changes are gonads (from 0.20 to 0.08) and breast (from 0.05 to 0.12).

public, the former being periodically subjected to medical screening. The limits are reported in Table 5-3.

	Type-A workers	**Type-B workers**	**Public**
Effective dose E	20 mSv/year	6 mSv/year	1 mSv/year
Lens of eye H_T	150 mSv/year	45 mSv/year	15 mSv/year
Hands, foots, skin H_T	500 mSv/year	150 mSv/year	50 mSv/year

Table 5-3 Italian year limits on radiation exposure (D. Lgs. 241/00).

The aforementioned rules do not apply to practices devoid of radiological relevance, i.e. causing dose equivalent exposition of public lower than 10 μSv/year; in case of contamination of gaseous materials the radiological relevance limit is set to 1 Bq/g of mean radioisotopes concentration.

6 NEPIR at SPES

The NEPIR facility will be powered by the new high-current proton cyclotron at the INFN Legnaro National Laboratory (LNL), the driver for the Selective Production of Exotic Species (SPES) project (Figure 6.1). The accelerator can deliver two proton beams at the same time, with adjustable energies in the 30-70 MeV range and with a maximum shared current up to 750 μA.

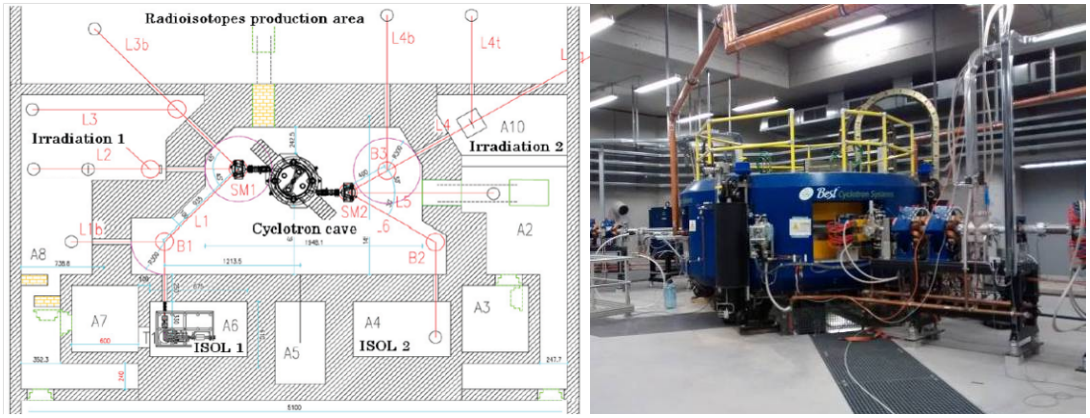

Figure 6.1 On the left, a schematic drawing of the SPES building with the cyclotron cave, two ISOL target stations and experimental halls: the one labelled "irradiation 1" is assigned to NEPIR. On the right, a picture of the cyclotron.

The NEPIR project was originally conceived to provide fast neutrons (E_n > 1 MeV) and direct protons to study radiation effects on electronic components and systems for terrestrial, avionics and space applications. The construction of the facility will occur in phases, according to the available funding. It is currently financed by SPARE (Space Radiation Shielding), an ASI/INFN project consisting of a test campaign of active and passive shielding materials for the human activity on Mars using fast neutron beams at NEPIR and protons at the TIFPA cyclotron facility with E_{proton}= 70-228 MeV.

The SPARE funds available for the NEPIR project allow the construction of a minimal version (NEPIR-0) of the facility, with only one fast neutron target station. It will provide neutrons with a continuous energy spectrum, intense enough to be useful to characterize neutron-induced effects in electronic components and small systems or measure the performance of shielding test structures.

The final stage (NEPIR-1) requires substantially more funds and foresees the development of two more fast neutron targets (the QMN source and ANEM) to provide beams with different

energy distribution for different applications. A direct proton beam irradiation chamber is also foreseen.

NEPIR at the SPES cyclotron		
	Phase 0	**Phase 1**
Proton energy	30 – 70 MeV	20 – 70 MeV[6]
Proton current	1 μA (max)	10 μA (max)
Target	Be (30 mm)	ANEM: W (5 mm) + Be (24 mm) QMN: Li
Power in the target (W)	70	700
Fast neutron energy spectrum	continuous up to 70 MeV	ANEM: continuous up to 70 MeV QMN: quasi mono-energetic with variable peak energy in the 20-70 MeV range
Neutron flux ($1<E_n<70$ MeV)	Max $\sim 10^6$ n/cm^2/s	Max $\sim 10^7$ n/cm^2/s

Table 6-1 NEPIR project main parameters.

6.1 NEPIR radiation environment

At the NEPIR facility the production of intense neutron fields requires accurate studies of the effects due to induced radiation: being clear that the access to the experimental hall will be forbidden during an irradiation, the main concern is the estimation of reactions induced by the produced neutrons which leave active nuclei in the environment, with particular emphasis on directly irradiated objects and walls.

Neutrons, being electrically neutral, are especially effective in inducing nuclear transformations; they are not repelled by Coulomb barriers and can penetrate nuclei.

A neutron traversing a medium can undergo scattering (elastic or inelastic) or it can be absorbed. Elastic scattering is very effective in slowing down neutrons in light materials: the maximum energy loss in one single interaction for a neutron of energy E travelling through a medium of mass number A is given by

[6] For the QMN system, it is foreseen that a carbon plate be used to decrease the energy of the primary proton beam (the cyclotron minimum is 30 MeV) to get QMN peaks down to 20 MeV.

$$(\Delta E)_{max} = \frac{4A}{(A+1)^2} E$$

which shows that hydrogen target nuclei give the maximum “slowing down power” per interaction.

Inelastic scattering interactions are also effective in slowing down neutrons, but they produce residual excitation which is typically released as gamma radiation. This effect is sizeable for high energy neutrons traversing heavy materials: the shielding design should consider this additional effect, but typically the amount of material required to absorb most of the neutrons is sufficient to attenuate also this induced gamma radiation.

Radiative capture reactions are very likely to occur for slow neutrons: the cross-section typically follows a *1/v* law (*v* is the neutron velocity), however some absorbers (e.g. cadmium) can exhibit resonance peaks as shown in Figure 6.2. The effect of radiative capture in the interaction of neutrons with air nuclei is of particular concern in NEPIR experimental hall that, during irradiations, is flooded by slow neutrons backscattered from the walls. Since the emitted gamma can be quite energetic and active nuclei can freely move, it can deserve attention for radiation protection purposes.

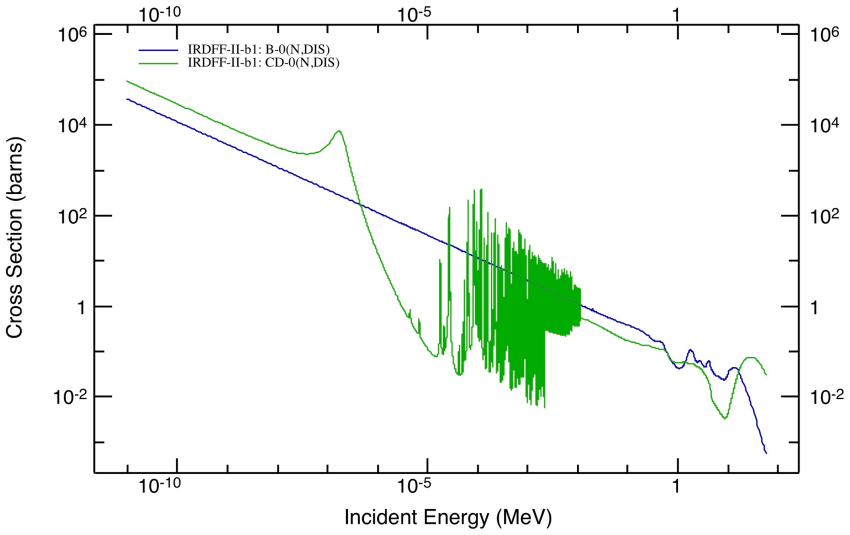

Figure 6.2 Neutron absorption cross-section versus neutron energy for boron (blue line) and cadmium (green line).

Neutron induced reaction with the emission of a charged particle typically have quite high energy threshold, but the fast neutron field produced at NEPIR can exceed the reaction thresholds for target materials that are typically used in experimental equipment and in concrete as shown in Figure 6.3.

Some reactions with charged particles in the exit channel however have relatively high cross-sections for slow neutrons: Figure 6.4 shows that the reaction $^{10}B(n,\alpha)^{7}Li$ is very effective in absorbing slow neutrons. For this reason, boron-enriched materials are used to shield neutron fields, with the advantage that the emitted alpha particle has very limited range. On the negative side, slow energy neutrons impinging on ^{14}N present in air can produce ^{14}C, a long-lived radionuclide (5700 year half-life) which emits gamma radiation (the cross-section is shown in Figure 6.4).

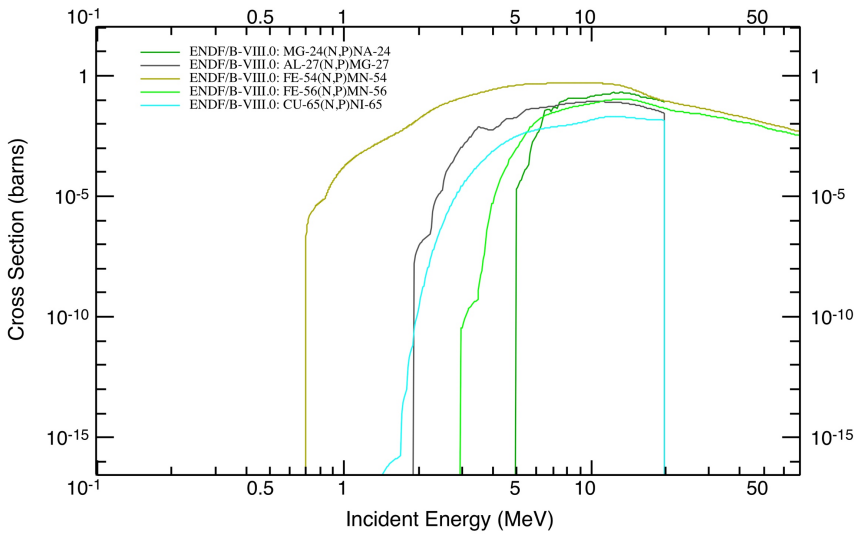

Figure 6.3 Charged particle emission reaction cross-section versus neutron energy (up to 70 MeV) for different materials typically present in experimental environment (magnesium, aluminum, iron, copper). The energetic neutron field produced at NEPIR can open this reaction channel in objects directly flood by neutrons.

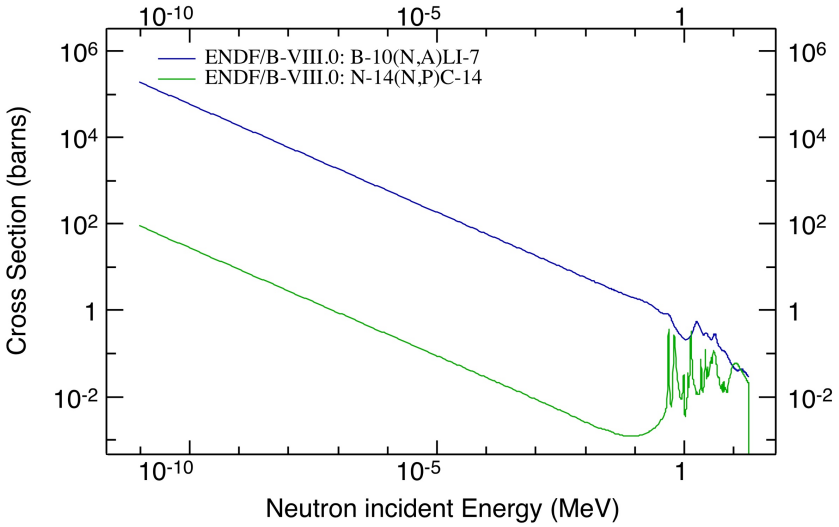

Figure 6.4 $^{10}B(n,\alpha)^{7}Li$ and $^{14}N(n,p)^{14}C$ cross-sections as a function of the neutron energy. ^{10}B is very effective in absorbing slow neutrons and it is often used in shielding design. The presence of ^{14}N in natural air and the intense field of slow neutrons due to scattering from the walls requires attention, to avoid excessive concentration of ^{14}C in the experimental hall.

6.1.1 Activity calculations

The activity of a given radionuclide refers to the number of atoms that decay per unit time and it is measured in Becquerel (Bq). The radioactive decay is a random process characterized by an average lifetime τ or, equivalently, its reciprocal λ (decay constant). In presence of N(t) particles of a single radioactive species the activity of the sample at time *t* follows the simple differential law

$$A(t) = -\frac{dN(t)}{dt} = \frac{N(t)}{\tau} = \lambda\, N(t)$$

that knowing the number of particles N(0) at time *t=0* can be integrated to obtain the activity at any future time t

$$A(t) = \lambda N(0)\, e^{-\lambda t} = A(0)\, e^{-\lambda t}$$

For historical reasons, the time required to halve the original activity, called half-life $T_{1/2}$, is commonly tabulated and it is used in this work (taken from the compilation of the National Nuclear Data Center [8]) to characterize radionuclides.

The typical experiment at accelerator facilities consists of an irradiation session going on for a period of time starting at *t=0* and ending at $t=t_{irr}$, with a constant rate of particle flux (fixed proton beam current). This is followed by a decay period, called cooling time, starting at $t=t_{irr}$

and ending at $t=t_{irr}+t_c$. The problem is complicated by the presence of multiple nuclear species that can feed each other through decay. The activity at time *t* due to a precise nuclear species *i* is expressed by the Bateman equation:

$$A_i(t) = -\frac{dN_i(t)}{dt} = \sum_{j \neq i} [\lambda_{ji} + \overline{\sigma}_{ji}\overline{\phi}] N_i(t) - \sum_{j \neq i} [\lambda_{ij} + \overline{\sigma}_{ij}\overline{\phi}] N_j(t)$$

with $\overline{\phi} = \int \phi(E) dE$ and $\overline{\sigma}_{ji} = \frac{\int \sigma_{ji}(E)\phi(E)dE}{\overline{\phi}}$

where λ_{ji} is the decay rate of the nucleus *i* into the nucleus *j*

σ_{ji} is the cross-section for the transmutation of nucleus *i* into nucleus *j*

$\phi(E)$ is the beam differential flux

the sum is carried over all possible nuclei *j* produced by the interaction of the beam particles with *i* in the first term and over all possible nuclei that can produce *i* in a reaction with the beam particles in the second term.

The activity due to a single species during an irradiation period for $t >> 1/\lambda$ reaches a saturation value which is proportional to its production rate and when the beam is switched off it decays down to zero with the same decay constant λ. These effects in a complex environment mix together and give curves for build-up and cooling activities that sum up together the contributions of all active nuclei with their own time characteristics and populations. The best way to take into account each contribution is by using software tools.

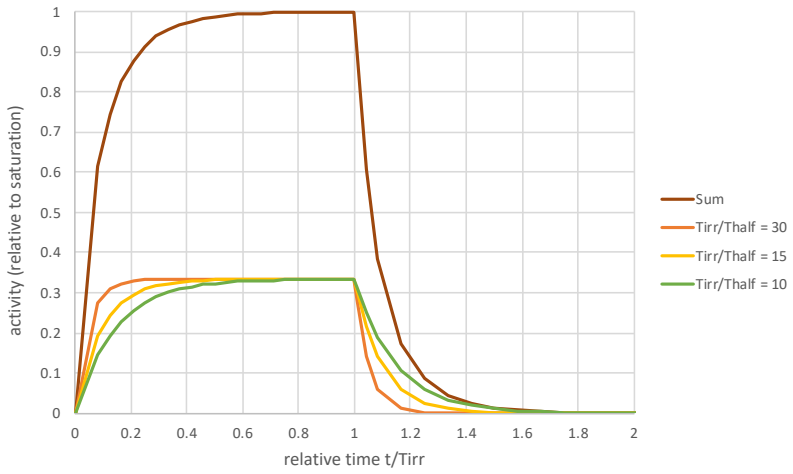

Figure 6.5 Build-up and decay of three different isotopes characterized by the ratio of the irradiation time T_{irr} and their half-lives T_{half}. In this calculation, the plateau activity of each isotope is set to account for 1/3 of the total plateau activity to better highlight the trend in time of the different curves.

7 Monte Carlo simulations: the FLUKA code

The design of a new physics facility is a very complex job because many aspects need to be handled together; sometimes, some issues are more complicated than the physics case itself. In the past, shielding design was based on analytical and numerical techniques (point-kernel formulae, build-up factors and attenuation lengths) and computers were used to run simple codes or primitive Monte Carlo with simple geometries and many physics approximations. Now the availability of fast computers allows the use of sophisticated Monte Carlo codes to handle problems of practically any degree of complexity, with detailed calculations of the history of each particle on its path through matter based on evaluated cross-section data and validated theoretical models.

In this work the FLUKA code [9] [10] is mainly used: it is a general purpose tool for calculations of particle transport and interactions with matter, covering an extended range of applications. Microscopic models are adopted whenever possible and results are verified on experimental data at each interaction level. Therefore, results in complex cases arise naturally from the underlying physical models and predictivity is provided where no experimental data are directly available. The Monte Carlo approach adopted in FLUKA samples actual physical phase space distributions and predicts average quantities and statistical moments of any order. Particle transport is handled as a Markovian process, i.e. the behavior of a particle depends only on its present properties, not on previous histories, and primary particles do not interact with each other.

In Monte Carlo codes, particle histories are sequences of various events related to physics interactions or transport information, such as boundary crossing. Events are treated in two categories: discrete and continuous. Although actual physical events are essentially discrete, certain sequences of many similar microscopic events are described as a continuous macroscopic one. A typical example is the treatment of charged particles where the energy deposition and direction changes are the results of many discrete collisions: these quantities are condensed into a sum of losses and an overall scattering angle. This approach is known as the “condensed-history” technique [11].

FLUKA can handle even very complex geometries, using an improved version of the Combinatorial Geometry (CG) package. Media and geometry are assumed to be static, homogenous, isotropic and amorphous: however, activation studies with a variation of the geometry are possible with a “two-steps” approach. In FLUKA, materials properties are not

affected by particles reactions, so the degradation of a target, due to the reactions that happen inside it, can't be considered.

The Monte Carlo analog of a measurement is called a score or tally: it merges the definition of an estimator (a measuring technique) to a well-defined region in the phase-space (a detector). FLUKA implements a variety of built-in estimators to be activated and tailored by the user: modern fast computers allow also to construct a multiple detector (a mesh detector covering a large region of real space), which is useful for example to identify shielding weaknesses.

The result of a calculation is obtained by adding up the contributions to a tally defined by the user, typically requesting a radiometric quantity. The final score is the average value of the corresponding population and it is possible to associate a statistical error to it by running several independent calculations. The variance of the mean of an estimated quantity *x* calculated in *N* batches is given by:

$$\sigma_{\bar{x}}^2 = \frac{1}{N-1}\left[\frac{\sum_1^N n_i x_i^2}{\sum_1^N n_i} - \left(\frac{\sum_1^N n_i x_i}{\sum_1^N n_i}\right)^2\right]$$

where n_i is the number of histories in the *i*-th batch and x_i the average in the *i*-th batch. The standard deviation of an estimator calculated from batches is an estimate of the standard deviation of the actual distribution, with increasing precision as $N \rightarrow \infty$.

It is important in this context to highlight that in the Monte Carlo world the meaning of a calculated statistical error is different than that in experimental data, as stated in Table 7-1 which is taken from the MCNP Manual [12]: this guideline is empirically based on experience, not on mathematical proof, but it has been generally confirmed also in other codes.

Relative error (%)	**Quality of tally**
50 – 100	Garbage
20 – 50	Factor of a few
10 – 20	Questionable
< 10	Generally reliable

Table 7-1 The meaning of statistical errors in Monte Carlo world [12].

In addition to statistical errors, Monte Carlo results are affected by systematic errors. The first source of systematic errors are code weaknesses related to the physical model used; some uncertainties are also unavoidable concerning the experimental data on which a code is based. Other systematics come from lack of information: material composition is sometimes difficult to obtain with good accuracy (for example for concrete and soil). Complicated geometries or

environmental conditions need to be simplified: for example, air contains humidity and pollutants and has a density variable with pressure, but these details are neglected in most calculations. At last the user can make mistakes since the preparation of the input for a calculation can be very complex.

A FLUKA input is an ASCII text file which consists of a variable number of commands written in one or more lines (called “cards”). The following elements need to be defined in the input file.

- Definition of the radiation source (beam particles, direction, divergence, position etc.) by means of several predefined options; more sophisticated features can be described using a user-written routine SOURCE.
- Description of the geometry by means of bodies (delimited by surfaces of first or second degree) and regions (boolean combination of bodies) that define cells of uniform material composition.
- Materials definitions and assignments to regions.
- Definition of the requested detectors, the Monte Carlo equivalent of a measurement instrument: each “score” or “tally” is designed to estimate one or more radiometric quantities and the final score is a statistical estimation of the average value of the corresponding population.
- General technical directives to the program on how the calculation shall be performed: energy cut-offs, physics effects, biasing options, call to user routines, etc.

The simulations in this work are arranged by means of Flair [13], an advanced user friendly interface to facilitate the editing of FLUKA input files, execution of the code and visualization of the output files via a GUI environment. It also provides means for building the executables, debugging the geometry, monitoring the running status, post processing the binary output files and interfacing with plotting utilities, like gnuplot.

7.1 Activation data benchmarks

The capabilities of FLUKA are unique for studies of induced radioactivity, especially regarding nuclide production, their decay and the transport of residual radiation. Particle cascades by prompt and residual radiation are simulated in parallel based on microscopic models for nuclide production and a solution of the Bateman equations for activity build-up and radioactive decay.

Predictions for the production of residual isotopes strongly depend on the models implemented in the Monte Carlo code and sometimes show differences compared to experimental data,

which, at the same time, can depend on details of the experimental method. For this reasons, some benchmark experiments [14] [15] were performed at CERN, where different samples were flooded by the stray radiation field produced by a 1.2 GeV/c hadron beam impinging on a thick copper target: specific activities and remnant dose rates of the irradiated samples were then measured and compared to FLUKA simulations. The results of these studies show a good agreement of calculated and measured data for different materials present at accelerator facilities (aluminum, copper, iron, concrete). Some discrepancies emerge for intermediate- and small-mass isotopes (as compared to the mass of the sample material) that can be attributed to deficiencies in the FLUKA simulation models. Moreover, other discrepancies can be due to trace elements in the composition of the samples.

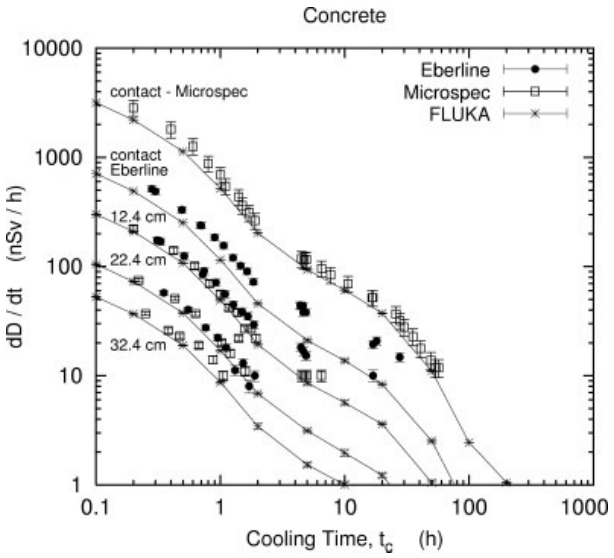

Figure 7.1 Residual dose-equivalent rate as a function of cooling time for an irradiated concrete sample. FLUKA calculations are compared to readings of two measuring instruments (by Microspec and Eberline) for different distances from the sample [15].

Regarding air activation due to neutron fields, a comparison between FLUKA calculations and experimental measurements have been made in [16]. In that case the only relevant active nucleus in air is ^{41}Ar and the FLUKA calculation gives an overestimation by a factor of 2 of the saturation yield.

8 NEPIR-1

In the final configuration, the NEPIR facility is provided with a dedicated bunker in hall A9, and two new target systems to produce:

- an intense quasi mono-energetic neutron (QMN) beam with a controllable energy peak in the 30-70 MeV energy range; a variable thickness carbon energy degrader will be used to degrade the energy of the primary proton beam below 30 MeV down to a minimum of 20 MeV;
- an intense beam of fast neutrons (E_n > 1 MeV) with a continuous energy (white) distribution like that of neutrons found at flight-altitudes and at sea-level (Atmospheric Neutron EMulator, ANEM).

An independent, low intensity direct proton beam line is also foreseen: it will be developed once the QMN and ANEM systems are completely designed and financed.

The design of the layout of NEPIR is shown in Figure 8.1: the QMN target system and the ANEM target are located in a heavily shielded bunker (in green) made up of 200 cm thick concrete walls and ceiling. The proton beam comes from the cyclotron hall (on the left) and a switching magnet selects the target station to which the beam is delivered.

When the proton beam is bent towards the QMN system, it passes through the thin lithium target of the QMN source and is further deflected by a bending magnet towards the heavily shielded beam dump, while the ANEM target is beam-stopping.

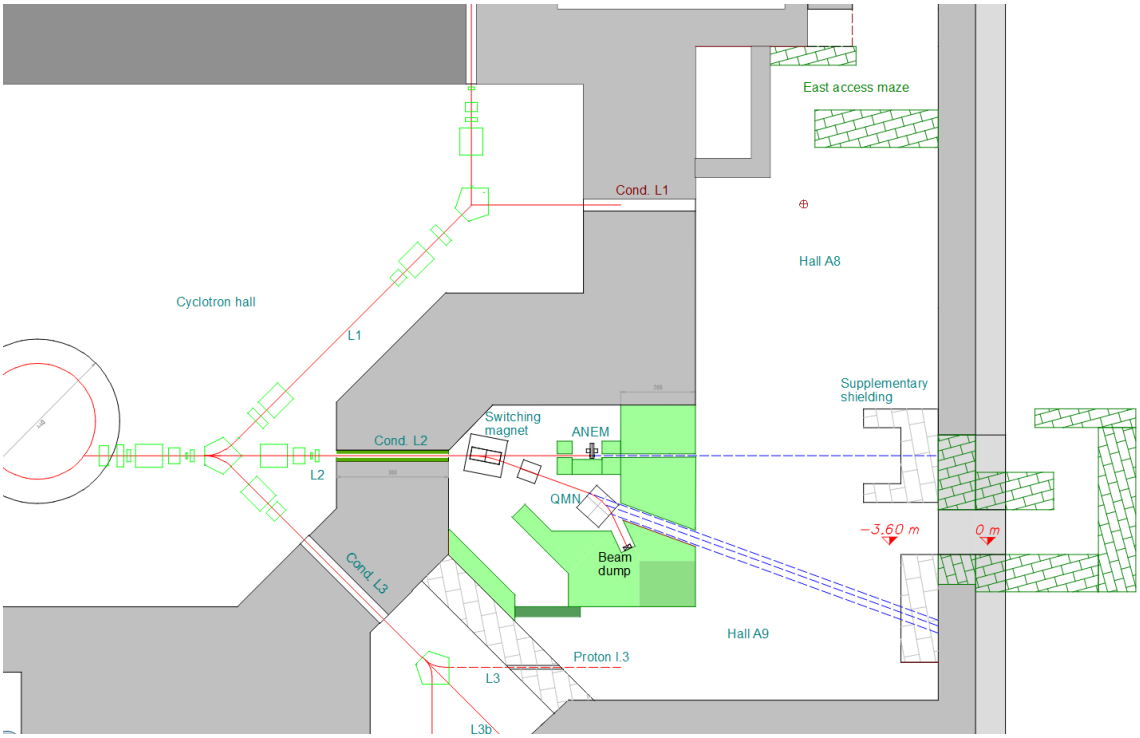

Figure 8.1 Schematic drawing of the floor plan of NEPIR-1. The proton beam from the cyclotron hall enters the target bunker and continues to the ANEM system or to the QMN target. A bending magnet deflects the spent protons emerging from the thin QMN target towards a beam dump. The building is partially underground, whereas the access maze on the right is at ground level.

8.1 White neutron beams: ANEM

The ANEM target, specifically tailored to study the effects of atmospheric neutrons in electronics, is designed to produce neutrons with an energy spectrum as much as possible similar to that of fast atmospheric neutrons in the 1-65 MeV energy range, with a high acceleration factor (F = 3×10^9).

ANEM is a rotating target system composed by a beryllium sector, followed by a coaxial tungsten disk. The 70 MeV proton beam is off the target axis and strikes the Be sector for a fraction of time during rotation, to better emulate the atmospheric neutron spectrum. The thickness of the W target (5 mm) is chosen to stop the proton beam, while the thickness of the Be sector (24 mm) has been set to avoid blistering caused by hydrogen build-up in the material: the low energy protons emerging from Be are then stopped in the more resistant W disk. Monolithic coaxial copper rings are used for mechanical and thermal coupling to the central steel drum, cooled by a helicoidal water cooling system.

The simulated spectra were obtained with MCNPX [17] (Monte Carlo N-Particle eXtended), a general purpose Monte Carlo radiation transport code of great dynamic range with excellent neutronics capabilities developed at the Los Alamos National Laboratory.

For the W target, some experimental data from the EXFOR library are available at a proton energy of 50 MeV [18]: these data are represented in Figure 8.2 compared with the calculated data using the LA-150 library, developed for proton- and neutron-induced reactions up to 150 MeV energy. LA-150 library reproduces the experimental data generally well, but in this case tends to overestimate the high energy neutron region. The good agreement in the forward direction indicates that a similar simulation using LA-150 with a 70 MeV proton beam should be quite reliable: the results calculated with this energy, on a 5 mm thick W target, constitutes the reference spectrum of the W component of the ANEM target used in this work.

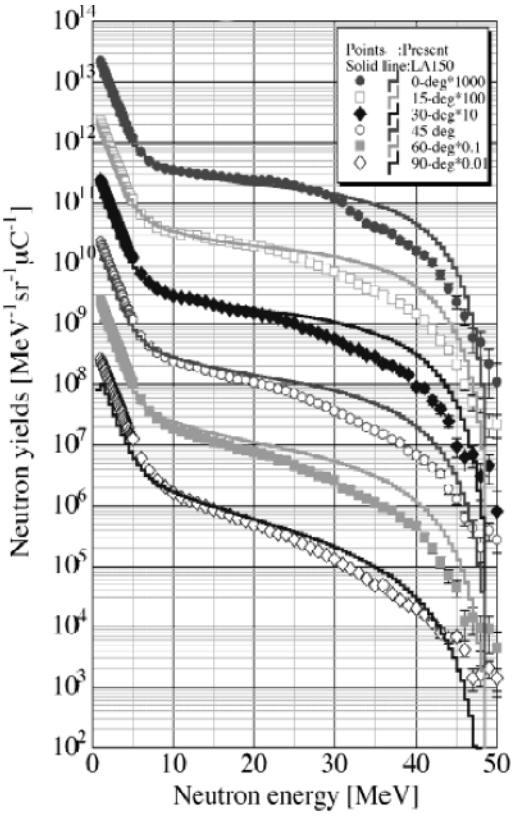

Figure 8.2 W(p,xn) spectra with angular dependence: experimental and LA-150 results comparison for a proton energy of 50 MeV [18]. The first at the top is in the forward direction: multiplicative factors are used to make the plot clearer.

For the Be component of the target, the available data are confusing both in yield and especially in shape of the neutron energy spectrum. Experimental data between 60 and 70 MeV (Figure 8.3) indicate a curved shape for neutrons with energies above 50 MeV: the FLUKA simulation is

in good agreement with these data, whereas the MCNPX calculation presents a sharp drop. To get some insight into the issue of the shape of the energy drop-off from a thick Be target, the figure includes the measured spectrum of quasi mono-energetic neutrons (QMN) produced by 70 MeV protons on a thin Be target (4 mm). In a thick Be target, the highest energy neutrons are produced in the initial layer, by the highest energy impinging protons, and a sharp drop-off is expected, consistent with the one of the QMN peak. Moreover, the overall shape should be somewhat flat, as it is the convolution of many QMN spectra produced by the proton beam penetrating and losing energy inside the target. For the same reason, the QMN and thick target yields are expected to be consistent too. Indeed the situation is very confused: on the one hand the MCNPX drop-off shape is sharp as expected, but the yield is too high; on the other side the experimental data and FLUKA shapes are not consistent with the sharpness of the QMN peak and their yields are too low.

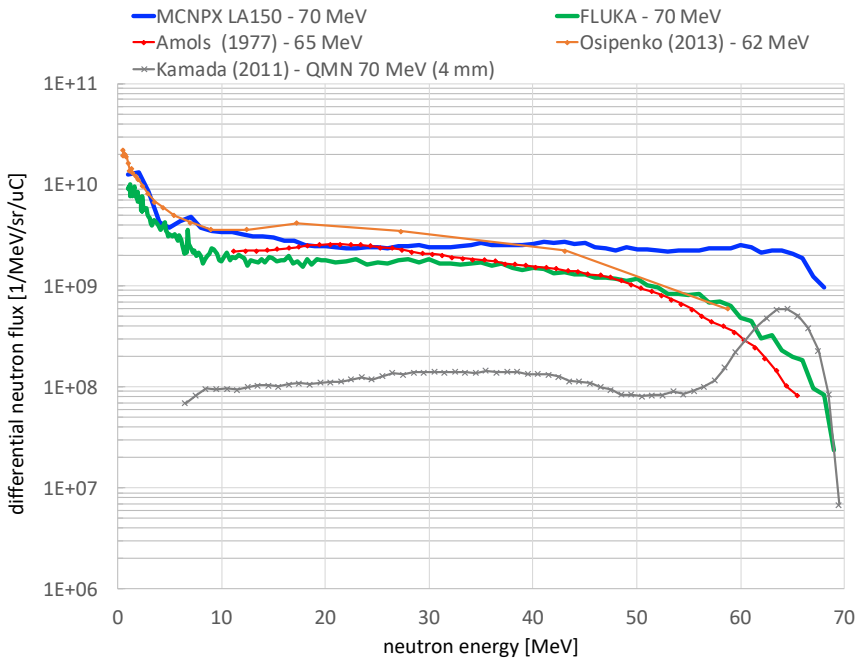

Figure 8.3 ^{9}Be(p,n) experimental (lines with markers, [19] [20] [5]) and calculated (lines without markers) differential neutron flux for beam energies between 60 and 70 MeV. Thin targets (QMN) data are also reported (crossed markers) to compare the QMN integral to the thick target yield in the same energy.

EXFOR nuclear database reports some data at 40 MeV proton energy for both a thick Be target and a thin one (Figure 8.4). In this case the thick Be experimental data points do show a sharp drop consistent with the shape of the QMN, as expected; the MCNPX calculations of the thick target show a sharp drop off, but again it overestimates the experimental yields; the FLUKA calculations do not meet any agreement.

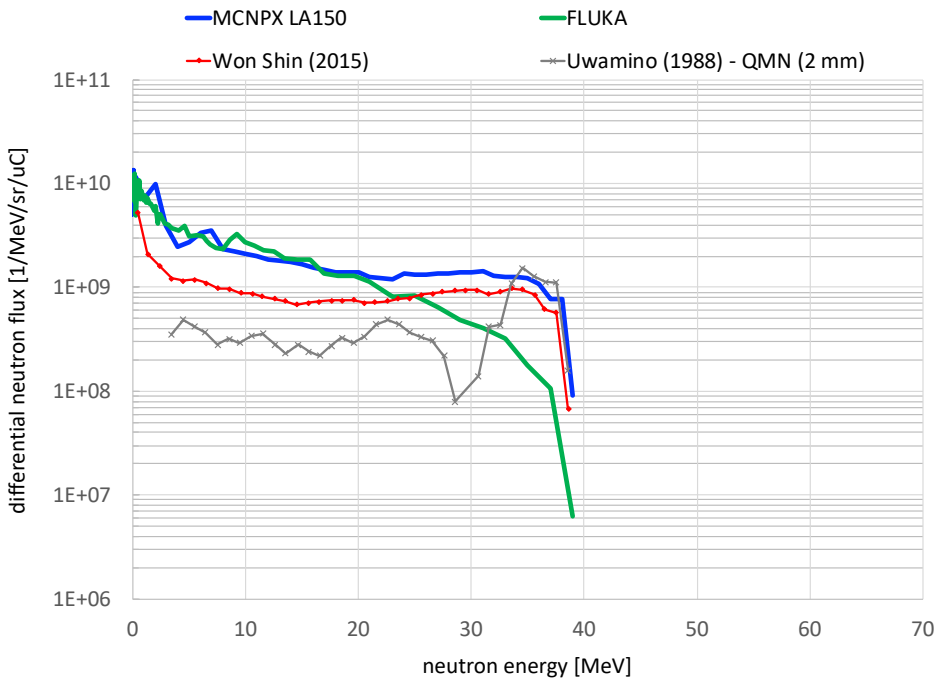

Figure 8.4 ^{9}Be(p,n) experimental (lines with markers, [21] [22]) and calculated (lines without markers) differential neutron flux for 40 MeV beam energy. Thin target data are also reported (cross markers) to compare the QMN integral to the thick target yield.

At lower proton energies, some experimental data are available at 23 MeV, better matched by the MCNPX calculation than by the FLUKA one in the region next to the drop-off (Figure 8.5).

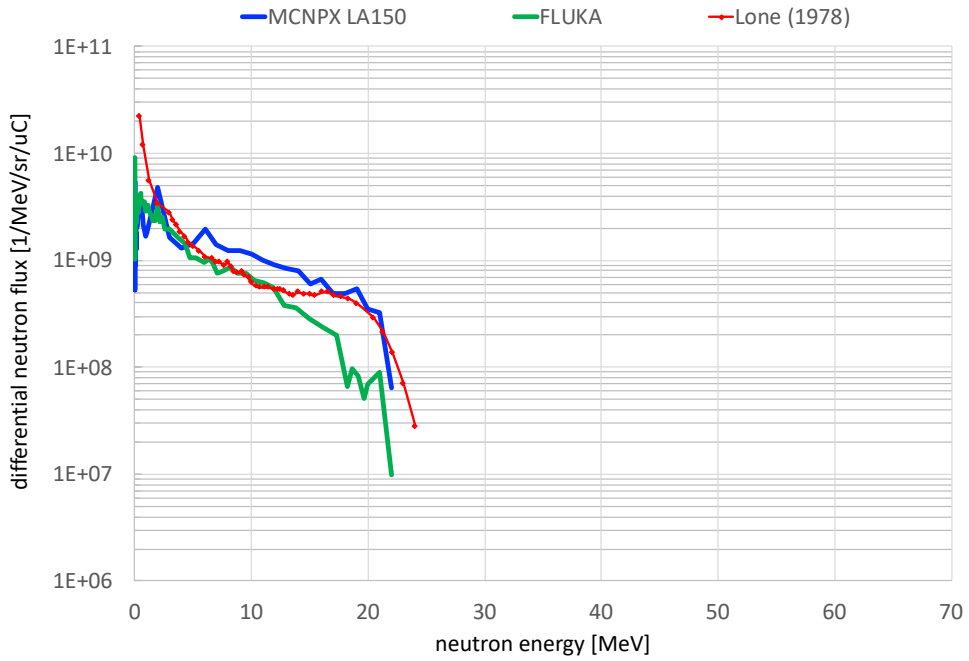

Figure 8.5 ^{9}Be(p,n) experimental (lines with markers, [23]) and calculated (lines without markers) differential neutron flux for 23 MeV beam energy. No thin target data are available in this energy range.

Since the shape of the neutron spectrum of thick Be plays a fundamental role in the design of the ANEM target, an extensive campaign of measurement is planned during the initial phase of the NEPIR facility realization. The spectra will be characterized with the MONDO detector [24], developed under the SPARE collaboration. The system is based on proton recoil technique and it is made of a matrix of orthogonal scintillating plastic fibers, read by SPAD (Single Photon Avalanche Diode) detectors. The scintillating material acts both as neutron target and tracker for the recoiling protons. The neutron tracking principle is based on the reconstruction of two consequent elastic scattering interactions with a hydrogen nucleus: by reconstructing the kinematics of the proton originated from (n,p) interaction, one can obtain the energy of the incoming neutron. If neither the neutron energy nor its direction are known, two subsequent interactions are needed to reconstruct both of them.

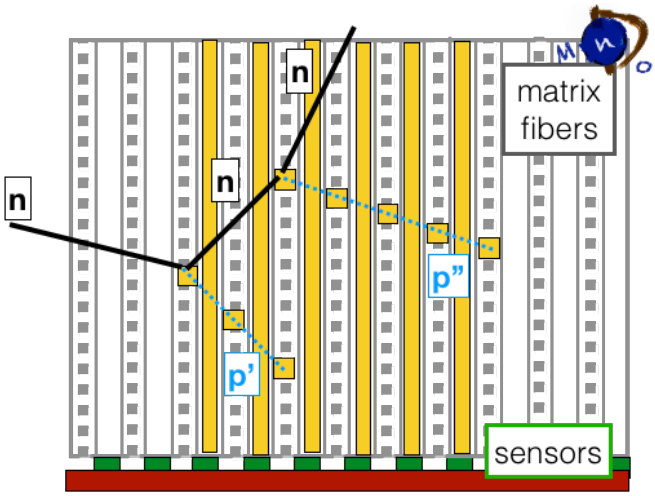

Figure 8.6 MONDO tracker design showing a neutron undergoing a double elastic scattering. Fibers activated from the proton energy release are highlighted in yellow. The entire system measures 16x16x20 cm^3.

In this work, the MCNPX calculated spectrum is used as reference, since it is harder than the others and should give a worst case scenario in induced activation and dose calculations.

The current design of the target (Figure 8.7) is also based on MCNPX results: the best agreement with the atmospheric neutron spectrum in the 1-65 MeV energy range is reached with 19% Be [25], that corresponds to a 68.4° wide circular sector.

The ANEM neutron differential energy spectrum, built as a weighted sum of the two material components, is shown in blue in Figure 8.8. The MCNPX predicted spectrum at a test point 3 m downstream the target for 10 μA beam current well matches the atmospheric neutron one in the 1-65 MeV energy range, multiplied by an acceleration factor F = 3×10^9: the integral flux over

that energy range is 1.2×10^7 n/cm^2/s. The uncertainties in the Be neutron yield at high energies reflects on the amount of necessary Be: if the yield is indeed 3 times lower, as the QMN data indicates, the amount of Be will have to be doubled (40%). On the other hand, a curved drop-off, instead of a sharp one, would limit the agreement with the shape of the atmospheric spectrum to the 1-50 MeV range.

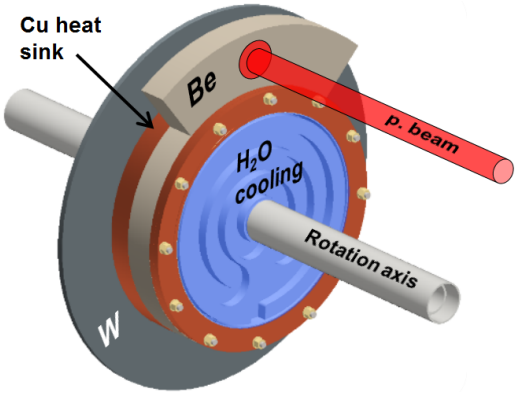

Figure 8.7 The 32 cm diameter Be and W components of ANEM intercept the 13 cm off-axis proton beam; the stainless steel rotating drum (diameter 18 cm) houses the helicoidal water cooling circuit.

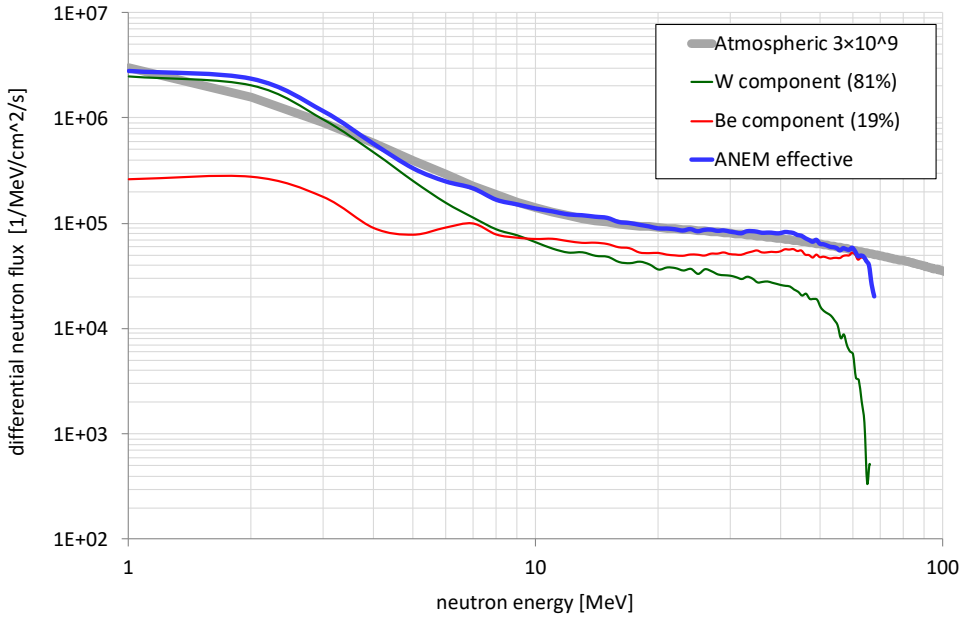

Figure 8.8 The MCNPX simulated ANEM differential neutron flux (blue) at a distance 3 m downstream the target (70 MeV proton beam, 10 μA current) compared to the reference sea-level one (grey) multiplied by an acceleration factor F = 3×10^9. The ANEM spectrum is the weighted sum of the spectra of the two target components: Be (19%, red) + W (81%, green).

This design was also simulated using finite elements calculations (ANSYS Workbench Platform [26]) to assess the thermo-mechanical properties of the target. Assuming a proton beam spot

with a Gaussian distribution (1 cm FWHM), the power safety limit of the W component was calculated to be 3.5 kW, using a 0.2 liters/s cooling water flux at a temperature of 10 °C and a target rotation frequency of 1 Hz. This maximum power corresponds to a proton current of 50 μA, a value much greater than the maximum planned at the NEPIR facility. In terms of thermal-mechanical performance, the Be sector is less problematic because of the lower amount of deposited energy, the greater thickness of material and the higher thermal conductivity, that contribute to a better power dissipation.

8.2 ANEM air activation calculations

In this work some radiation protection issues of the ANEM target station have been addressed: first of all, the activation of the air invested by the intense neutron field produced. Indeed, during accelerator operations, radioactive nuclides are produced by the interaction of neutrons and gamma radiation with the air both in the bunker and the experimental hall. In general, there can also be other sources of airborne radioactivity (dust formed by wall erosion and wear or emissions of gases from irradiated liquids). The composition of dry air is reported in Table 8-1.

	Percentage weight in air
^{nat}**C**	0.0124 %
^{nat}**N**	75.5267 %
^{nat}**O**	23.1781 %
^{40}**Ar**	1.2827 %

Table 8-1 Composition of air at normal temperature (20 °C) and pressure (1 atm).

The target bunker is airtight and the air inside, which is highly activated, is maintained at a pressure a bit lower than the neighboring rooms to avoid leakage. This air volume (about 100 m^3) is vented with two air changes per hour, to limit activation and temperature increase due to the power released by the target. The air extracted from the bunker is managed and exhausted by the air collection system of the SPES building at a central chimney equipped with activity monitor. Actually, the problem of air activation inside the target bunker is a secondary problem: access to the bunker for maintenance will be forbidden for a long period (weeks) after the end of an irradiation because many of the components will be highly activated.

The air activation in the experimental hall plays instead a crucial role in the design of the facility: a user will need to access the experimental setup after an irradiation to retrieve or change the Device Under Test (DUT). The experimental hall is not airtight and air changes are ensured by a simple ventilation to the outside world. The goal of this study is to verify the possibility to

irradiate a device up to 24 hours at 10 μA proton current without activating air more than 1 Bq/g, which is the threshold of radiological relevance (see chapter 5.1 for explanations). In this way, the leaks to adjacent halls and venting to the outside environment is legally tolerable.

8.2.1 Simulation setup

FLUKA capabilities in estimating the activation of air in a neutron field is benchmarked with experimental data in [16]. The calculated activity of the most problematic isotope (^{41}Ar) is overestimated by a factor of 2: this suggests that the here presented simulation results can be considered conservative and will be then verified with experimental measurements.

A FLUKA simulation is implemented with some important cards for activation studies:

- RADDECAY requests the simulation of radioactive decays; it is set to analytically solve the Bateman equations for an arbitrary irradiation pattern;
- IRRPROFI defines the irradiation profile (period and beam intensity);
- DCYTIMES defines the times when scoring can be requested;
- DCYSCORE associates scoring detectors with previously defined times;
- RESNUCLE produces a list of residual nuclei and their activity on a region basis;
- USRBIN can also be set to score specific activity (ACTOMASS) in a region.

Moreover, two PHYSICS cards are needed to activate evaporation of heavy fragments and coalescence treatment.

The simulation is set to directly generate neutrons with the given calculated energy spectrum, in order to avoid the CPU-intensive calculation of proton nuclear interactions in the target. This neutron beam illuminates the collimator and travels to the experimental hall. A source with a specified energy spectrum requests a FORTRAN user-written routine to be compiled and linked to the FLUKA run: with the activation of the card SOURCE, the program calls the routine whenever it starts a new history and samples the energy of the particle from the given distribution. The defaults[7] are set to NEW-DEFA as in [16]. The irradiation time is set to 24 hours. The output neutron flux at the test point (obtained with a USRTRACK tally) is normalized to the expected value obtained by previous calculations (see section 8.1), in this way the activity is scaled to the “neutron current” equivalent to 1 μA proton current.

[7] Defaults are global options available in pre-packaged sets used to reach the maximum precision for a particular type of application (at the expenses of time efficiency).

A USRBIN card is used to score specific activity (ACTOMASS) of the air volume inside the experimental hall (see Figure 8.9): some shrewdness is needed because the output is given in Bq·cm^3/g and must be divided by the region volume (about 700 m^3) during the offline analysis[8].

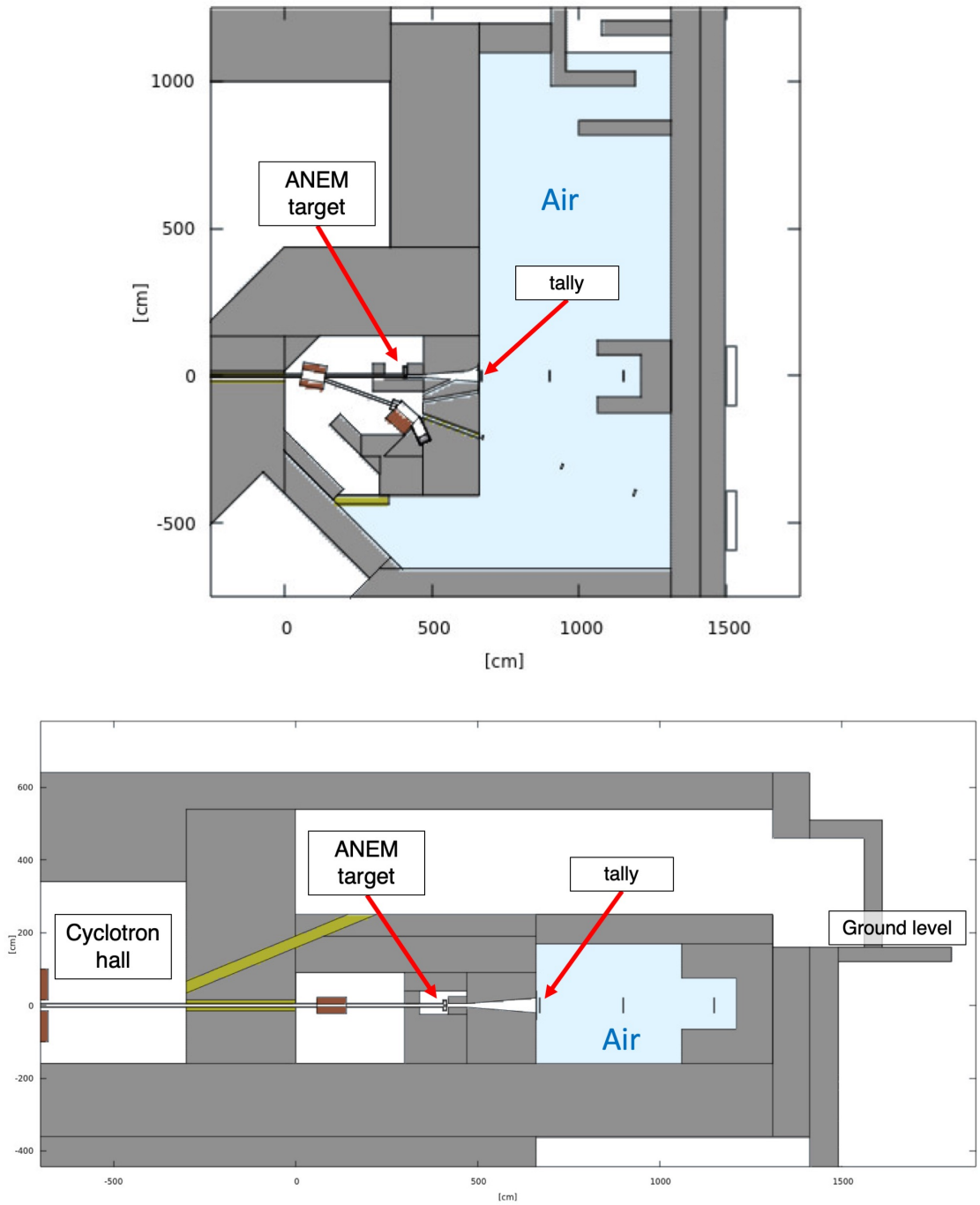

Figure 8.9 NEPIR facility map and vertical section with the position of the ANEM target and the tally for the neutron spectrum: in light blue, the volume of air in the experimental hall.

[8] See USRBIN page in FLUKA-manual [34], note 13.

Running several batches of the same problem, the required results are provided as averages with their standard deviation. The main contribution to systematics is the lack of information on the Be neutron spectrum: as explained, the neutron flux tally at the test point, just outside of the collimator, allows to calculate the normalization factor for the expected flux. The air activation estimation, obtained employing this same factor, becomes independent on possible errors in the neutron yield from Be. In this work, this estimation is conservative, since the maximum yield has been considered. If the experimental yield was found lower, more proton current would be needed to obtain the same neutron flux, so the limit can possibly become the thermo-mechanical tolerance of the target.

In the next two sections, results relative to the W and Be contributions are presented: both elements will be used in the ANEM neutron source, but the performance of a W-only target is also of interest since it could be a precursor of ANEM.

8.2.2 Tungsten target contribution

The air activation for an irradiation of 24 hours at 10 μA beam current is calculated: the build-up (beam on) and cooling (beam off) is presented in Figure 8.10 for the W component of the target. During the build-up, the limit of 1 Bq/g is rapidly exceeded and the plateau activity is reached in about 5 hours; during the cooling, the activity falls below the limit in about 1 hour. However, the limit must be respected during the entire irradiation for the above-mentioned reasons, so this configuration does not meet this requirement (even more so for the ANEM W+Be combination).

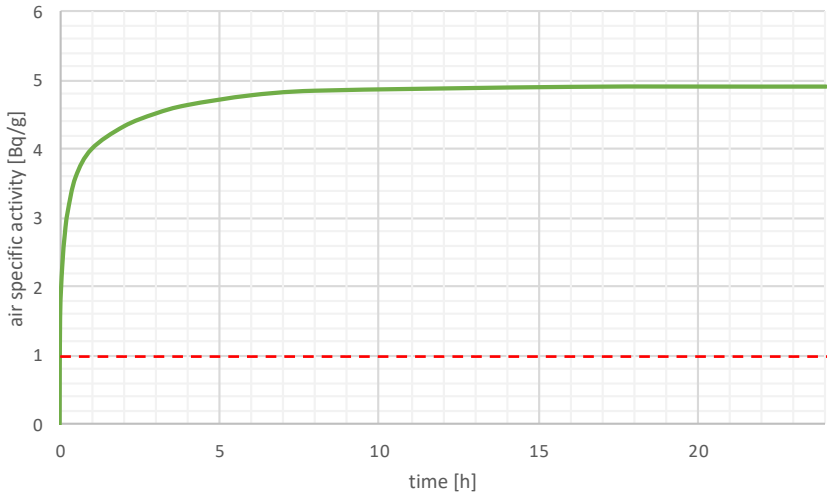

(a)

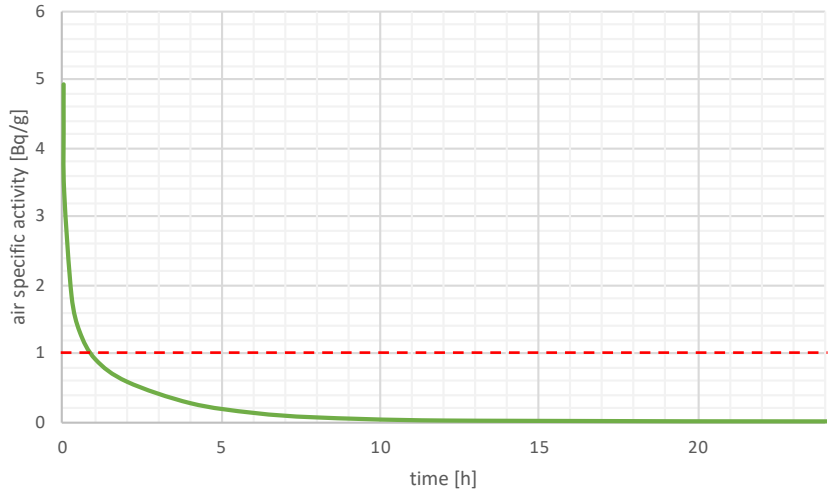

(b)

Figure 8.10 Air activation build-up (a) and cooling (b) during 24h irradiation at 10 μA beam current on W. The two periods are separated for graphic clarity: time starts when beam is turned on in (a), whereas it starts when beam is switched off in (b). Errors are < 5 %.

The possibility to reduce the activation of air decreasing the collimator aperture is explored. The collimator is made of concrete and defines a conical beam of neutrons: smaller collimators define a smaller solid angle acceptance, so the total delivered neutron flux is reduced together with the irradiated area at the test point. The build-up curves for different collimator apertures are presented in Figure 8.11, with a label indicating the beam spot diameter at the test point (2.6 m downstream the target).

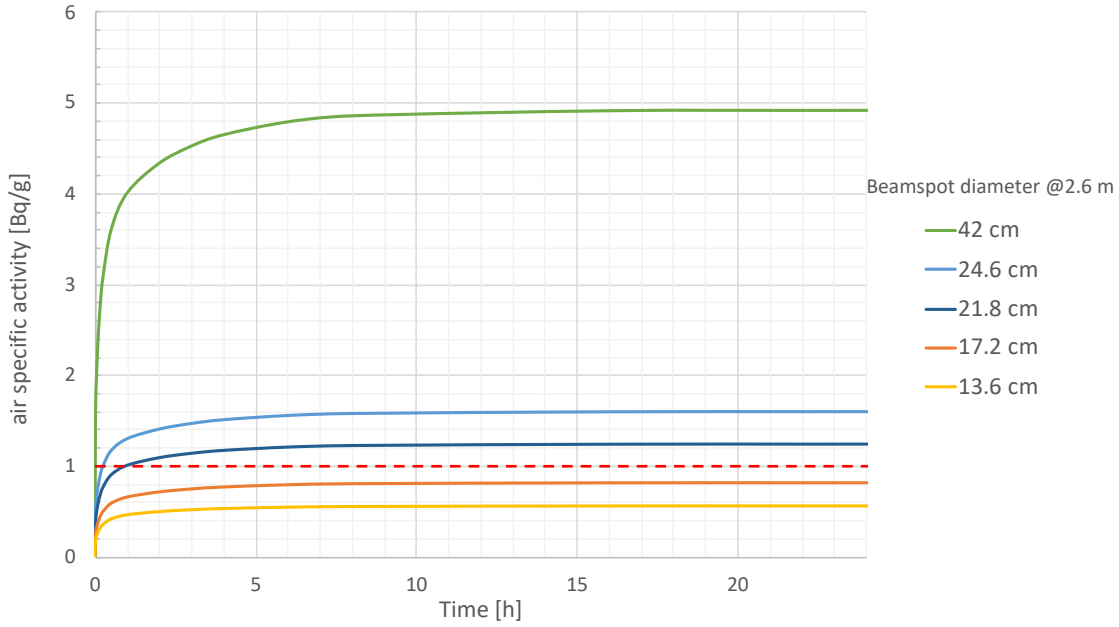

Figure 8.11 Air activation build-up with different collimator apertures (24h irradiation, 10 µA beam current on W). Errors are < 5%.

The values of the plateau activity are plotted against the beam spot area (proportional to the solid angle): Figure 8.12 confirms a linear dependence. Errors on the area consider some approximations in the design of the geometry in the simulation; errors on the activity include both a statistical term (few %) due to the simulation and a systematic term due to the considered value of the air volume in the experimental hall (about 1%). This linear fit is left free to intercept the y-axis in a non-zero position since some deviation from the simple model is expected. The positive intercepts (Table 8-2) shows that with a completely closed collimator there is still a residual activity in air: this mathematical behavior points out some second order effects that contribute to the activity but are not included in the above model based only on the directly irradiated area. For example, there could be some permeation of neutrons from the wall between the bunker and the experimental hall and there is also the contribution of albedo neutrons from the perimeter walls that is inevitable.

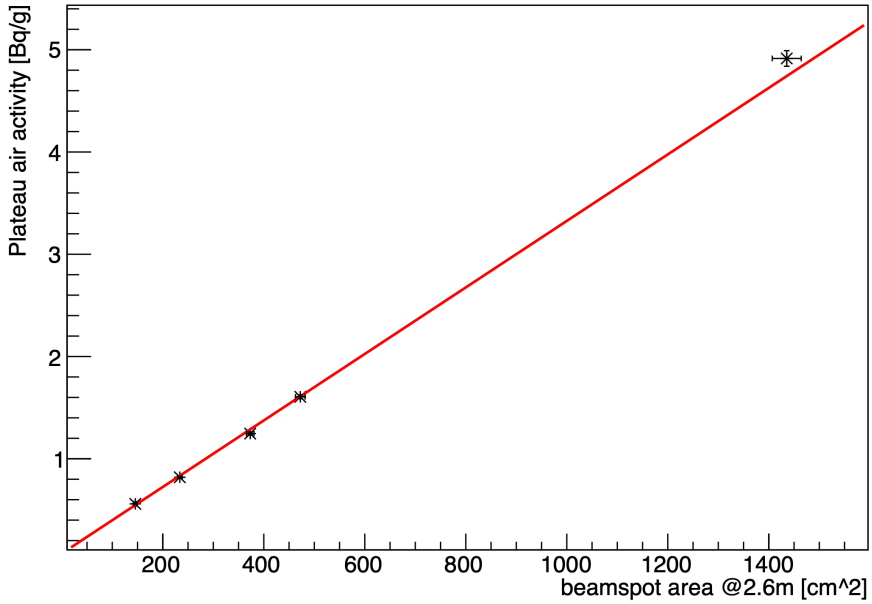

Figure 8.12 Plateau air activity as a function of the beam spot area at 2.6 m, calculated using a custom source with neutron energy spectrum from W, for 10 μA beam current.

W target	
$A_\infty = m \cdot S + q$	
m [Bq/g/cm^2]	$(3.25 \pm 0.07) \times 10^{-3}$
q [Bq/g]	0.07 ± 0.02

Table 8-2 Linear fit results: W target plateau air activity A_∞ as a function of area S (@2.6 m, 10 μA beam current).

The fitting parameters allows to extrapolate that the maximum beam spot diameter to stay below 1 Bq/g is 19.1 cm (at 2.6 m). This result refers to a W disk target (no Be).

8.2.3 Beryllium target contribution

The activation of air depends on the delivered flux of neutrons and the cross-sections of the reactions that leave some active nuclei: considering the uncertainties on the neutron flux, the worst case scenario is chosen, with the hardest available neutron spectrum from Be (MCNPX LA150 simulation).

The same procedure used above is applied to the Be target which is expected to give more activation problems due to a greater and harder neutron yield. This expectation is confirmed in Figure 8.13: a complete Be disk would produce about 6 times more activation in air than a W disk due to the higher neutron yield.

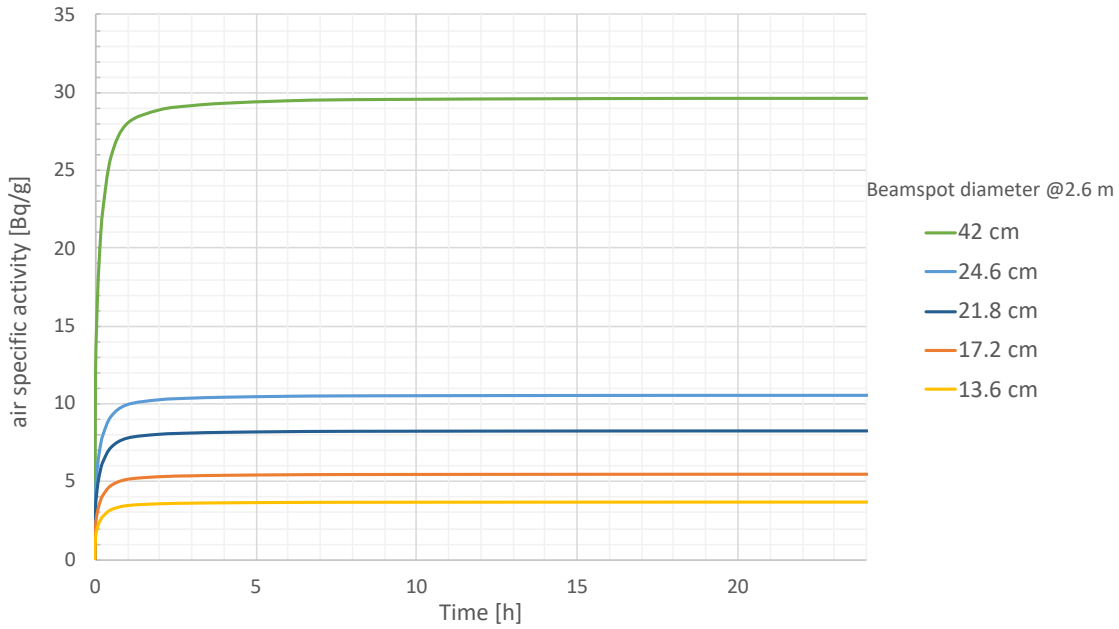

Figure 8.13 Air activation build-up with different collimator apertures (24-hours irradiation, 10 μA beam current on Be). Errors are < 3%.

The extrapolation of a maximum admissible collimator aperture for a pure Be target is not performed because the exploitation of such a target is not foreseen in this phase of the project.

8.2.4 Composite target results

Since the neutron differential flux of the composite target is the weighted sum of its components, the plateau activity should be the composition of the two previous results. However, running one single simulation using an energy spectrum that is the weighted sum of the two components, unexpectedly gives a 10% mismatch (Figure 8.14). A good portion of the discrepancy may be attributed to statistical errors. To calculate the maximum allowed diameter for the collimator of the ANEM target (current design, 19% Be sector), the weighted sum of the Be and W contributions is used and increased by 10% (worst case scenario). Results are shown in Figure 8.15.

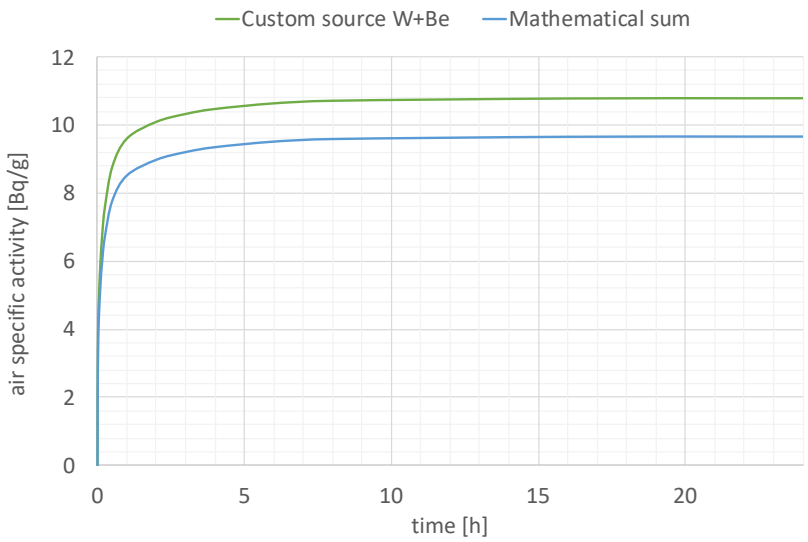

Figure 8.14 Air activation build-up (24h irradiation, 10 µA beam current, maximum collimator aperture): comparison between the weighted sum of the previous results (blue) and a simulation with a new neutron custom source with the weighted sum spectrum. Errors are < 3%.The difference in the plateau values is about 10%.

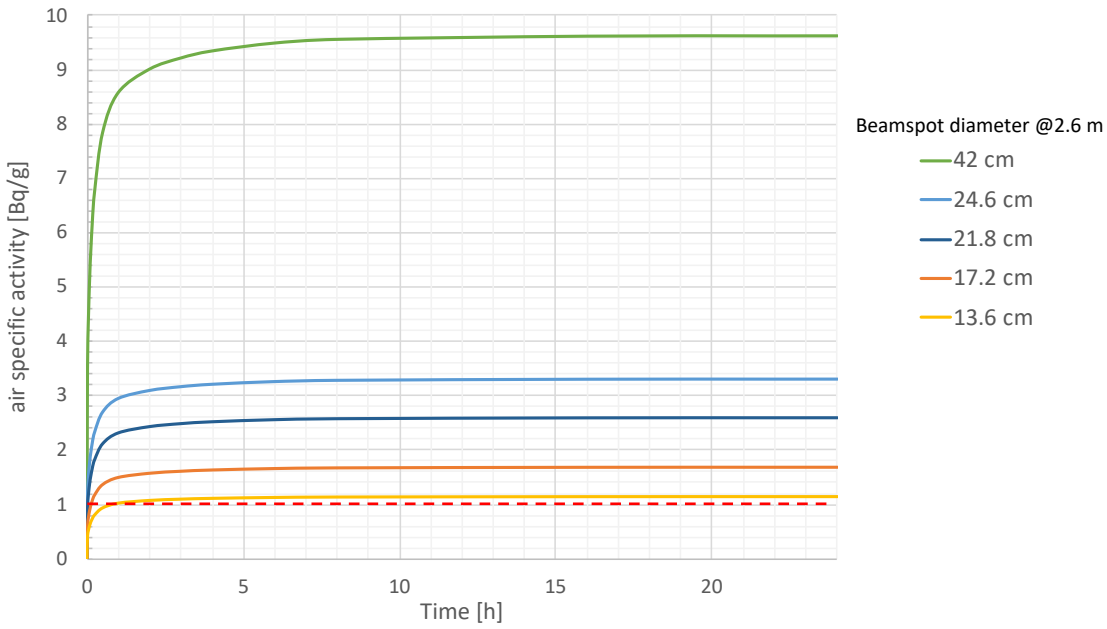

Figure 8.15 Air activation build-up estimation for the composite ANEM target with different collimator apertures (24h irradiation, 10 µA beam current). Errors are < 5 %.

These data are useful to evaluate the dependence of the plateau activity on the beam spot area (Figure 8.16) and get the linear fit parameters (Table 8-3): again the fit is left free as explained above for the W disk.

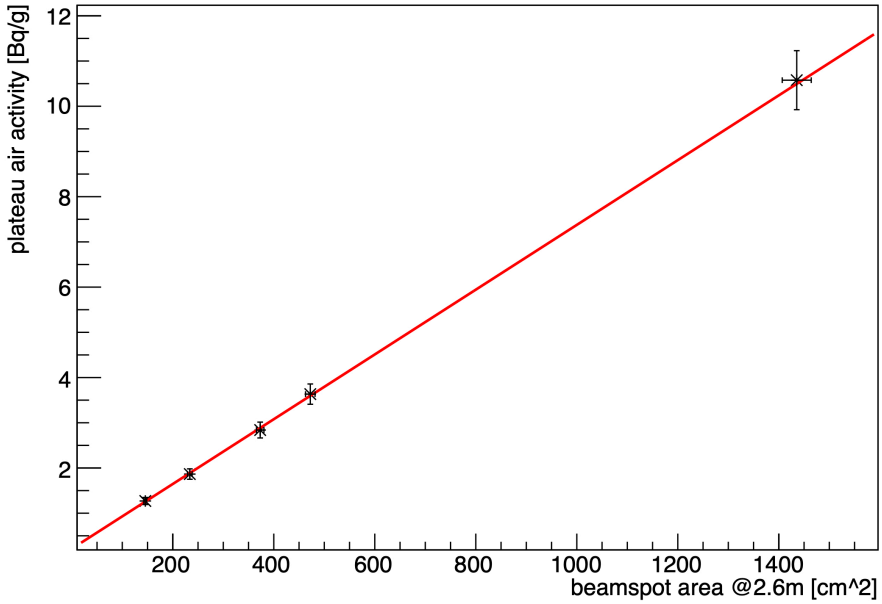

Figure 8.16 ANEM plateau air activity as a function of the beam spot area, at 2.6 m, for 10 µA beam current. Errors on the area consider some approximations in the design of the geometry in the simulation; errors on the activity include both a statistical term (< 2%) due to the simulations and a systematic term due to the procedure explained in the text (≈ 5%).

ANEM target	
$A_\infty = m \cdot S + q$	
m [Bq/g/cm^2]	$(7.2 \pm 0.4) \times 10^{-3}$
q [Bq/g]	0.2 ± 0.1

Table 8-3 Linear fit results: ANEM plateau air activity A_∞ as a function of area S (@2.6 m, 10 µA beam current).

Since the beam current is only a proportionality factor in the plateau activity, the fit parameters obtained for 10 µA are rescaled and related to different current values. Since the plateau activity is proportional both to the available solid angle (beam spot area) and the beam current, making a constraint on the activity (1 Bq/g), the other two quantities can vary on an hyperbolic curve. To better estimate this hyperbolic trend, a linear fit of beam spot area dependence on the inverse neutron flux is performed (Figure 8.17 and Table 8-4).

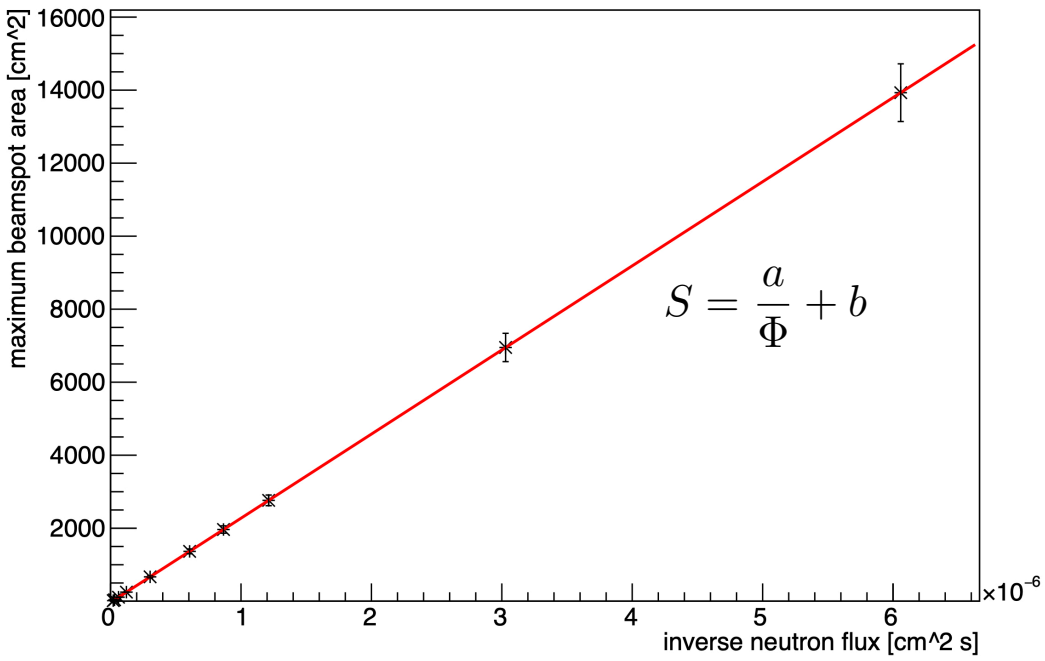

Figure 8.17 Linear fit of the maximum beam spot area as a function of the inverse neutron flux. Parameters of the fit are then used in the following plots.

S = a/Φ + b	
a [1/s]	(2.30 ± 0.05) × 10^9
b [cm^2]	-30 ± 6

Table 8-4 Linear fit results: ANEM maximum beam spot area as a function of inverse neutron flux (@2.6m, 10 μA beam current).

The results of the linear fit are then used to better visualize the activity limit of 1 Bq/g in some hyperbolic-like plots (Figure 8.18): shaded areas are forbidden for the excess of activation. The dashed red line instead indicates a value of beam spot diameter which is considered the minimum useful size for irradiation tests on electronic components[9]. These data allow to calculate analytical expressions to evaluate the most important quantities to handle (Table 8-5).

[9] Typically, the available neutron beam should be able to irradiate a 2x2 cm^2 chip (S. Gerardin, private communication).

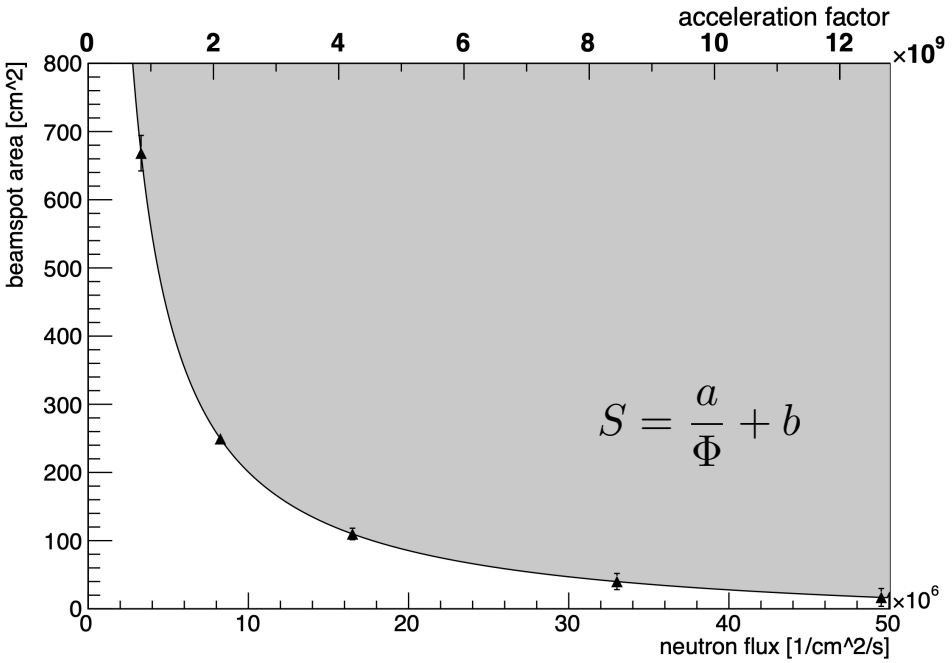
acceleration factor
0
2
4
6
8
10
12
×10^9
beamspot area [cm^2]
800
700
600
500
400
300
200
100
0
$S = \frac{a}{\Phi} + b$
×10^6
0
10
20
30
40
50
neutron flux [1/cm^2/s]

(a)

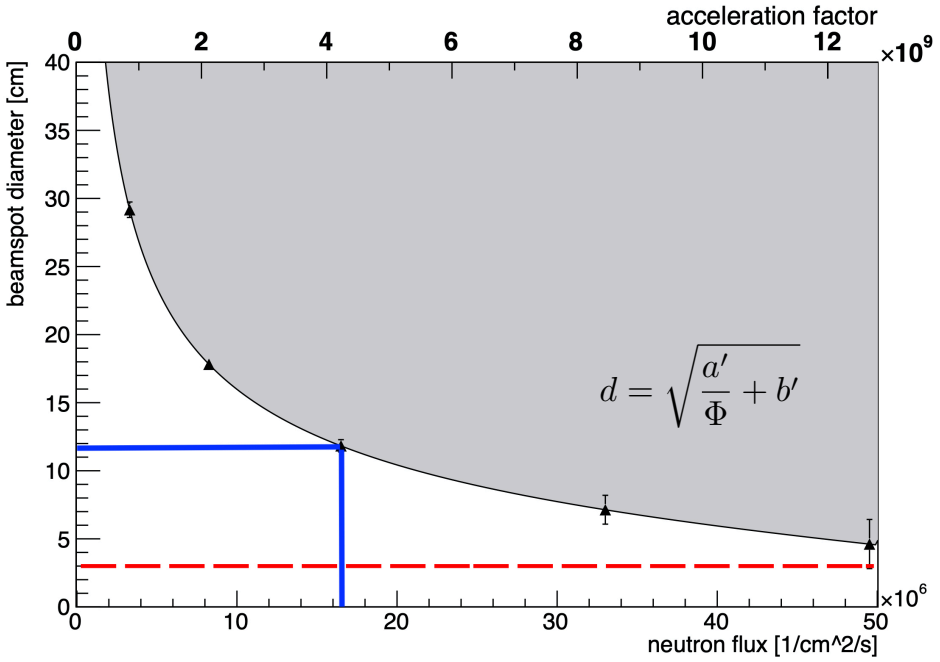
acceleration factor
0
2
4
6
8
10
12
×10^9
beamspot diameter [cm]
40
35
30
25
20
15
10
5
0
$d = \sqrt{\frac{a'}{\Phi} + b'}$
×10^6
0
10
20
30
40
50
neutron flux [1/cm^2/s]

(b)

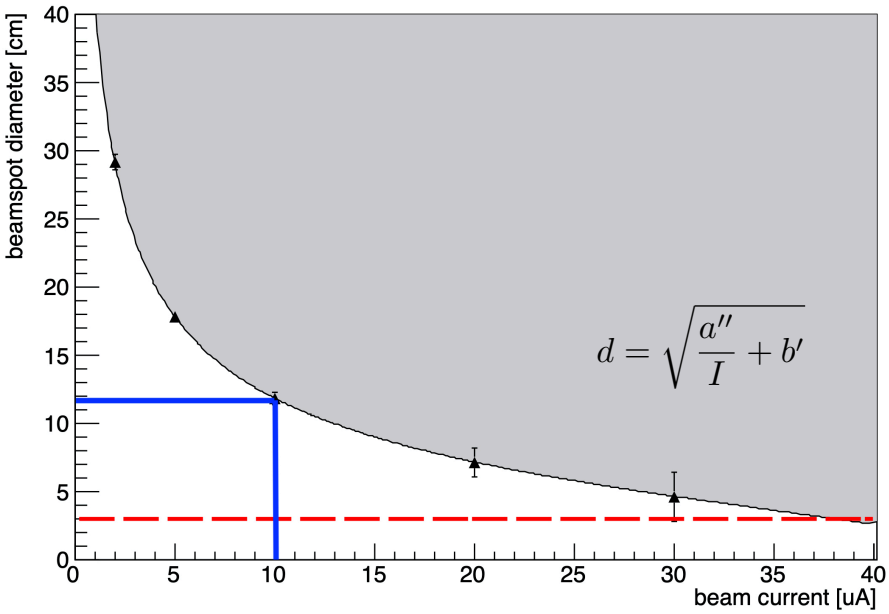

(c)

Figure 8.18 Hyperbolic-like plots to show the limiting values of different useful quantities: the separation line identifies the air activation limit of 1 Bq/g and the shaded area is forbidden. The red dashed line is a 3 cm diameter limit to insures a useful beam; the blue line highlights the operation conditions. In (a) and (b) a double x-scale is shown: at the top the acceleration factor of the atmospheric neutron flux corresponding to the artificial one at the bottom.

$d = \sqrt{\frac{a'}{\Phi} + b'}$	
a' [1/s]	(2.93 ± 0.06) × 10^9
b' [cm^2]	-38 ± 8
$d = \sqrt{\frac{a''}{I} + b'}$	
a'' [cm^2 μA]	(1.78 ± 0.04) × 10^3
b'' = b' [cm^2]	-38 ± 8

Table 8-5 Extrapolation of the parameter values for calculations of the beam spot diameter limits at a given neutron flux or proton beam current.

A neutron flux Φ=1.2×10^7 n/cm^2/s (F = 3×10^9) at a test point 3 m downstream the target is equivalent to a flux Φ'=1.65×10^7 n/cm^2/s (F > 4×10^9) at 2.6 m: this means that the goal can be reached with a maximum available beam spot diameter of d_{max} = *(11.8 ± 0.5) cm* at 2.6 m. This result is cheering and does not preclude the possibility to irradiate large electronic components, since at the end of the experimental hall the diverging beam would be 35 cm wide.

In this context, it is important to stress that the uncertainty on the neutron yield of the target has an impact on the relationship between the neutron flux and the proton beam current needed to get that flux. However, the entire work has been normalized to the expected neutron flux, so possibly some corrections will be necessary in the future only regarding the diameter-current relationship.

At this stage of the facility design, the neutron beam absorber (visible in Figure 8.9, at the end of the experimental hall) is simply made of concrete. As in other similar facilities, it could be a smarter object, made of layers of different materials, and its design will be addressed in the future. Here an ideal absorber ("blackhole") is simulated to estimate the maximum achievable deviation from the previous results on air activation: for the maximum collimator aperture (42 cm diameter at 2.6 m) the blackhole absorber gives a 12% reduction in air activation. This variation does not alter substantially the previous results: for this reason a better absorber is not strictly necessary to mitigate air activation issues, whereas it could be a key-factor to contain dose due to its own activation (see section 8.3.2).

8.2.5 Residual active nuclei in air

As previously mentioned, the card RESNUCLE is used to identify the residual active nuclei in air at specified times. The output produces a long list of radioactive species (Figure 8.19), but the majority of them has a lifetime less than 1 minute, so they quickly become negligible. The most important active nuclei after some minutes are ^{11}C, ^{13}N and ^{41}Ar with the last having the largest half-life (Figure 8.20 and Table 8-6): these results are consistent with literature [27].

At the end of an irradiation, an aeration system will ventilate the experimental hall; users who need to access it will have to wait some minutes for this air change to be completed, to avoid exposure to this source of radiation.

Nuclide	Half-life	Decay mode	Emitted radiation
^{41}Ar	109.61 m	β-	e-: 459.36 keV γ: 1293.64 keV
^{13}N	9.965 m	β+	γ: 511 keV (e+e- annihilation)
^{11}C	20.364 m	β+	γ: 511 keV (e+e- annihilation)
^{15}O	122.24 s	β+	γ: 511 keV (e+e- annihilation)

Table 8-6 Data for significant active nuclides present in air after the EOB.

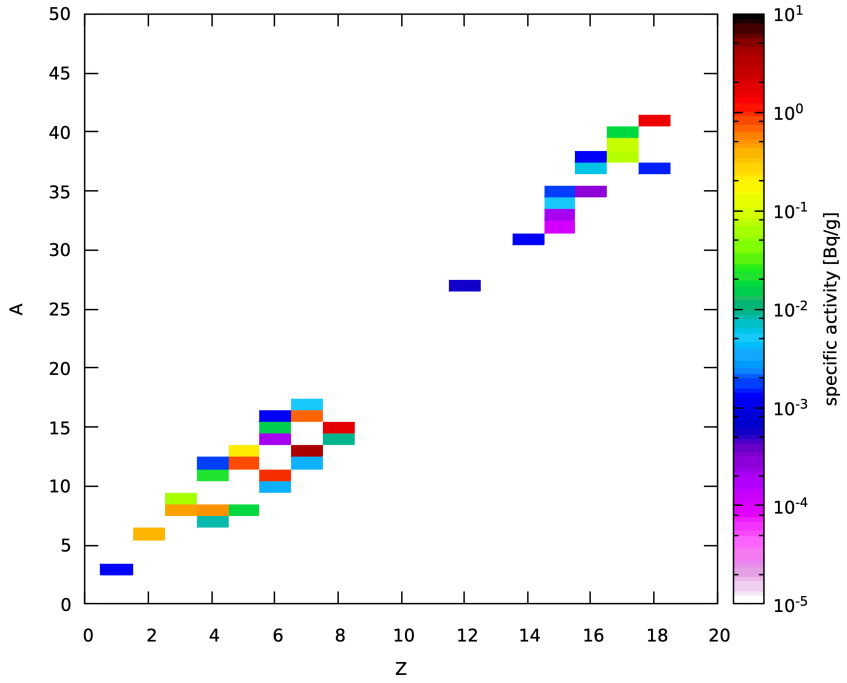

Figure 8.19 Residual nuclei in air at t=EOB (10 μA beam current, maximum collimator aperture). The main contributions come from ^{11}C, ^{13}N, ^{41}Ar and ^{15}O but the last go down very quickly: after 5 minutes the other three give more than 90% of the total activity.

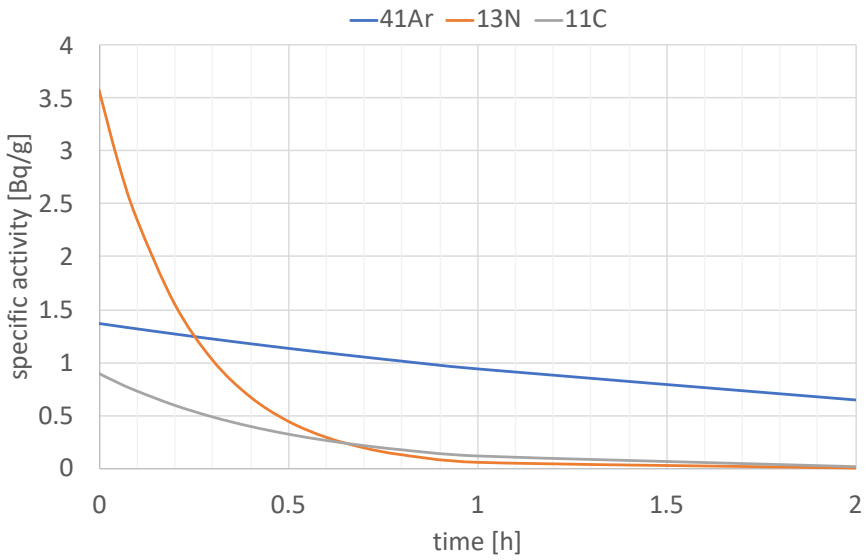

Figure 8.20 Specific activity trend in time (after the EOB) for the most important active nuclei in air (10 μA current, maximum collimator aperture). These 3 nuclei together realize more than 90% of the air activation, 5 minutes after the EOB. The decay times show that ^{41}Ar is the most problematic.

8.3 ANEM material activation studies

The large amount of neutrons produced by the ANEM target is only partially absorbed by the absorber at the end of the beam path. A fraction is backscattered in the experimental area, flooding any experimental equipment located inside. This neutron flux will induce a variety of nuclear reactions in the traversed materials and can leave residual radiation for long time. Some simulations are performed to study this effect.

8.3.1 Simulation setup and first results

FLUKA capabilities in estimating the activation of materials present at accelerator facilities have been benchmarked with successful results (as explained in 7.1).

In order to calculate the residual activation induced in the target material by the proton beam, the use of the neutron custom source, described in section 8.28.2 for air activation analysis, is unsuitable: it would not induce activation in the target. So, the results here presented are calculated using a uniform 3 cm radius proton beam impinging on a composite target. The target is modeled as a Be plate (24 mm thick), followed by a W one (5 mm thick); only a fraction (19%) of the beam section hits the Be plate, the remainder goes to the W plate, in order to reproduce at best the ANEM neutron spectrum. To calculate the activation induced in the materials surrounding the target (in particular the inner surface of the collimator) and the neutron absorber, the neutrons and gamma radiation emitted by the target, according to the FLUKA calculation, is exploited. It is important to notice that, beyond 20 MeV, the FLUKA-calculated neutron spectrum emitted by the composite target differs considerably from the MCNPX-calculated spectrum previously used by the custom source, as shown in Figure 8.21. Nevertheless, the strongest contribution to the neutron-induced activation is due to the low energy component, below 1 MeV, where the two spectra agree. This explain why a “full simulation” (with protons impinging on the target), instead of the neutron-only custom source, is used also to obtain the information relative to the residual activation of the shielding elements (collimator and beam dump).

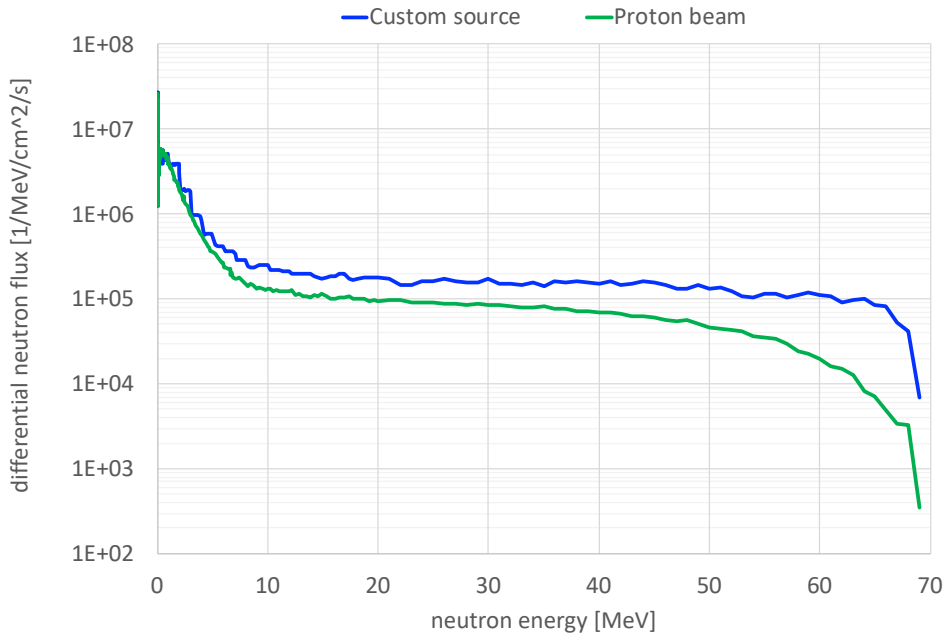

Figure 8.21 ANEM neutron spectrum at the test point, 10 µA current: in blue the FLUKA simulation with a neutron custom source based on the reference field, in green the FLUKA output for protons on the target.

Cards needed in activation studies are activated. The irradiation profile is set to deliver a 10 µA proton current continuously for 5 days (a worst case scenario). Many USRBIN cards are used to score the equivalent dose (DOSE-EQ) in a large region, allowing to plot a map of the dose-equivalent in the whole facility. This quantity represents the possible dose received by a human body located in a given place, for any position inside the geometry. To obtain one of this map, a cooling time is associated to each detector (with DCYSCORE card), obtaining an output expressed as pSv/s, which is subsequently renormalized to µSv/h[10]. The residual nuclei in irradiated materials are also scored via RESNUCLE card, also associated to different cooling times: 5 min, 1 hour, 4 hours, 1 day, up to 1 year.

A map of the equivalent dose rate, 5 minutes after the End Of Beam (EOB), is shown in Figure 8.22[11]: the highly activated ANEM target delivers to the experimental hall a large amount of electromagnetic radiation through the collimator aperture and it takes a long time (tens to hundreds of days) to go down to negligible levels (Figure 8.23). Figure 8.23 also shows the same trend for the three tally positions: this indicates that all tallies are sensitive to the same radioactive species, they only differ in the magnitude values.

[10] See DCYSCORE page in FLUKA-manual [34], note 1.
[11] Data are scored with a USRBIN mesh detector made of 10x10x10 cm^3 blocks: each colored box represents the mean value of a slice along the projected axis.

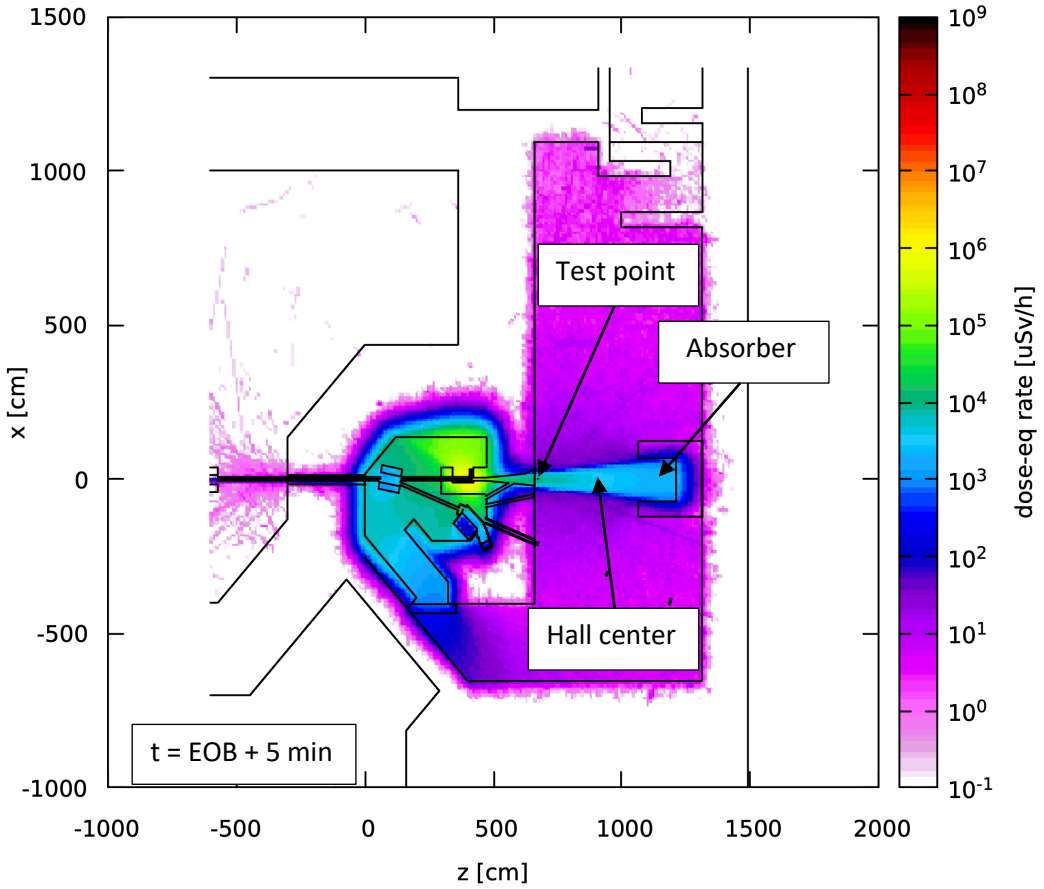

Figure 8.22 Map of the equivalent dose rate 5 minutes after the EOB produced by a proton beam impinging on the ANEM target (10 μA current, 5 days irradiation, y-range [-30,30]). The visible leakage from the bunker door will be addressed at a later time.

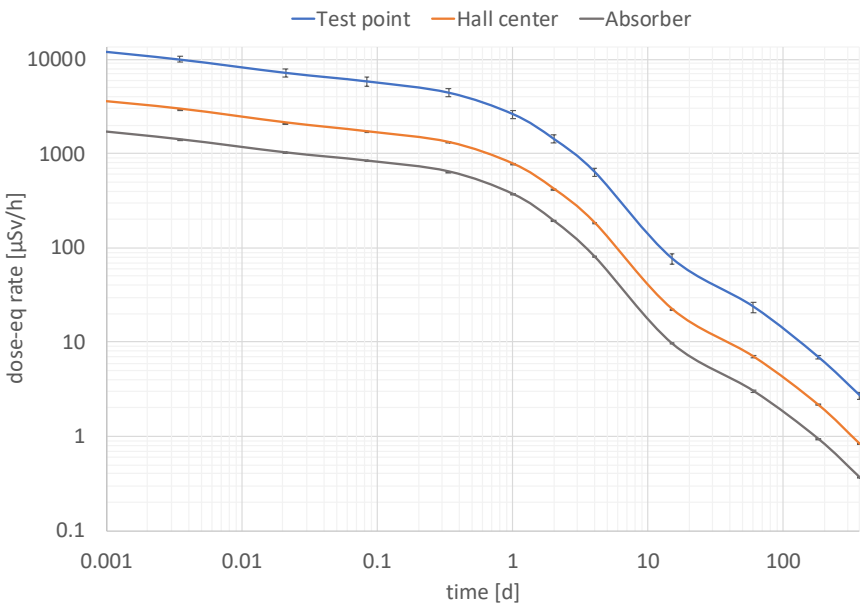

Figure 8.23 Equivalent dose rate trend in time after the EOB for three different positions in the experimental hall (indicated in Figure 8.22). This shows that the residual dose rate decreases slowly and

a dump is needed to stop direct emission from the highly activated target. The three curves show exactly the same trend: this means that the radiation from the target is the dominant contribution near the absorber, too. Errors are < 10%.

The residual nuclei score reveals two main contributions to the residual activity: ^{24}Na, which is generated inside the concrete elements, and ^{7}Be, which resides in the activated ANEM target (Figure 8.25 and Table 8-7). The huge dose contribution of ^{24}Na in accelerator environments is confirmed in many experimental studies [28]: this isotope is mainly formed by thermal neutron capture in the elemental sodium present in the aggregate (the cross-section of this reaction is shown in Figure 8.24) and its half-life is about 15 hours. The remaining contribution to the residual activity, characterized by a long decay time, is not directly attributable to a specific nucleus, but many candidates can contribute, generated mainly in the W(p,X) reaction. These results indicate the need to include in the design of the facility a mobile lead panel to close the collimator after the end of an irradiation, to absorb the residual radiation coming from the target, making the experimental hall, in particular the test point, accessible in a reasonable time.

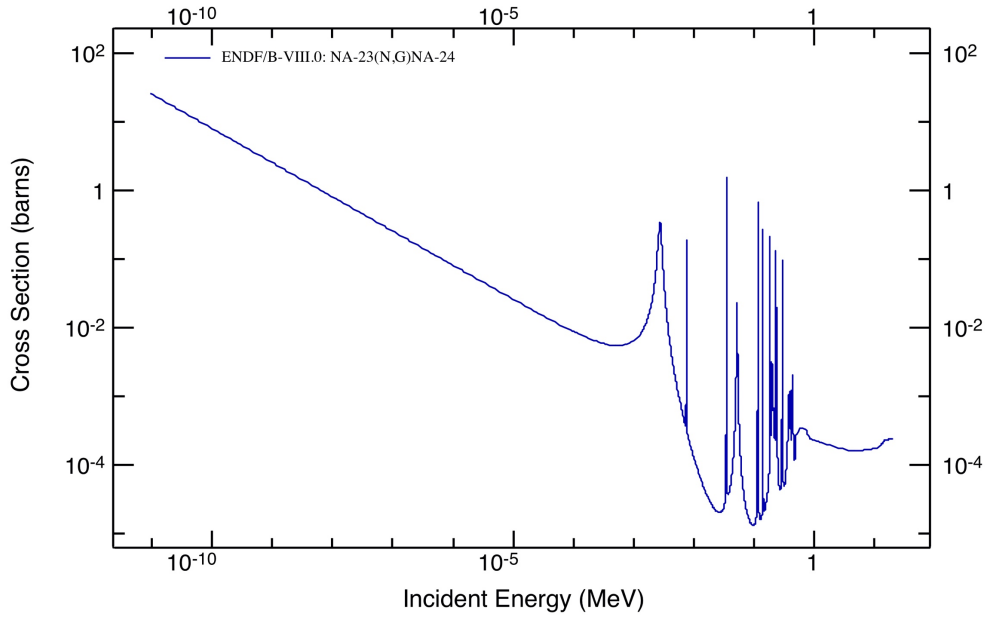

Figure 8.24 ^{24}Na production cross-section by neutron capture.

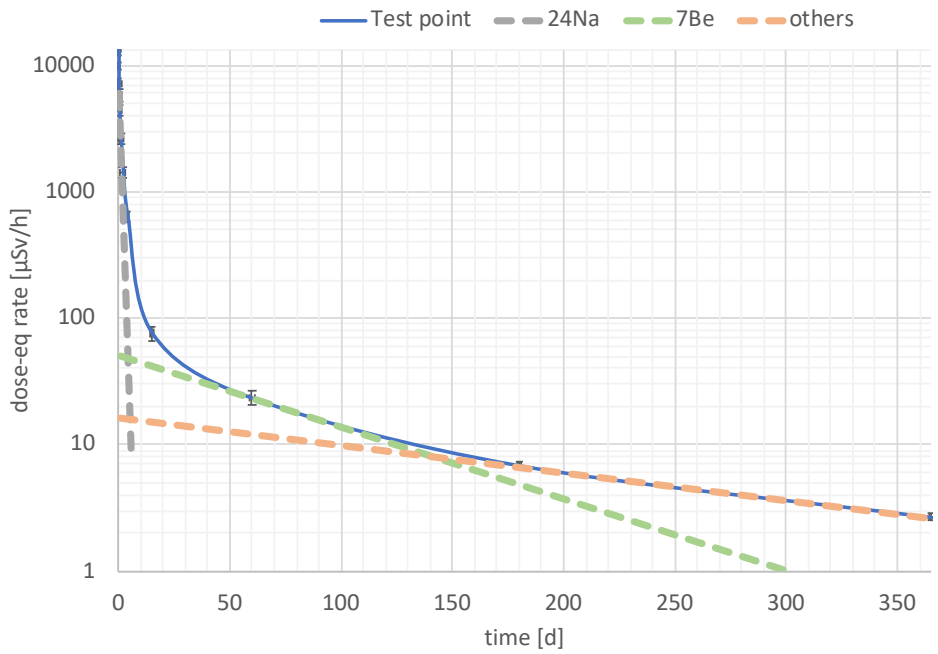

Figure 8.25 Equivalent dose rate trend in time at the test point with contributions from different active nuclei highlighted.

Nuclide	Half-life	Decay mode	Emitted radiation	Location
^{24}Na	14.997 h	β-	e-: 554.6 keV γ: 1.368-2.754 MeV	Concrete
^{7}Be	53.22 d	e-capture	γ: 477.6 keV	Target

Table 8-7 Data on nuclides that are the strongest contributors to the residual dose rate.

8.3.2 Albedo dose contribution

In this work, the neutron absorber used to stop the beam at the end of its path is modeled as a simple cavity in a large concrete block. The chemical composition of concrete can vary widely, but the inherent presence of water typically provides sufficient hydrogen to slow down neutrons to thermal energies. The NEPIR facility will use standard Portland concrete (density 2.3 g/cm^3) whose composition is reported in Table 8-8.

Element	Mass percentage	Element	Mass percentage
H	1.00 %	Al	3.40 %
C	0.10 %	Si	33.70 %
O	53.00 %	K	1.20 %
Na	1.60 %	Ca	4.40 %
Mg	0.20 %	Fe	1.40 %

Table 8-8 Portland elemental composition by weight: the isotopic composition is the natural one.

The concrete floor and wall surfaces of the experimental area will be coated with concrete sealer to prevent dust potentially activated by the neutron beam from being released and dispersed in air. Moreover, the coating prevents anything accidentally poured on the floor to penetrate the concrete, simplifying the collection and disposal operation.

The FLUKA code allows for each region to change the original material to vacuum or blackhole before performing the decay product transport[12]: with this feature an ideal absorber (blackhole) can be simulated in front of the collimator aperture to estimate the dose contribution in the experimental area only due to the neutron absorber and the surrounding walls. The resulting dose-map, represented in Figure 8.26, should be compared with the map in Figure 8.22, that includes the dose from the collimator and the activated target. Near the test point, the dose rate 5 minutes after the EOB is 2 orders of magnitude higher if the radiation from the collimator and the target is not shielded. With closed collimator, a researcher who needs to change the DUT could enter the experimental hall (5 minutes after the EOB, avoiding blue zones in the map) accumulating a maximum of 2.1 µSv of equivalent dose (0.42 µSv/min considering a reasonable time of 5 minutes). A long operation in the experimental area, like a maintenance intervention, would not be possible at a distance of minutes after the EOB.

[12] See ASSIGNMAt page in FLUKA-manual [34].

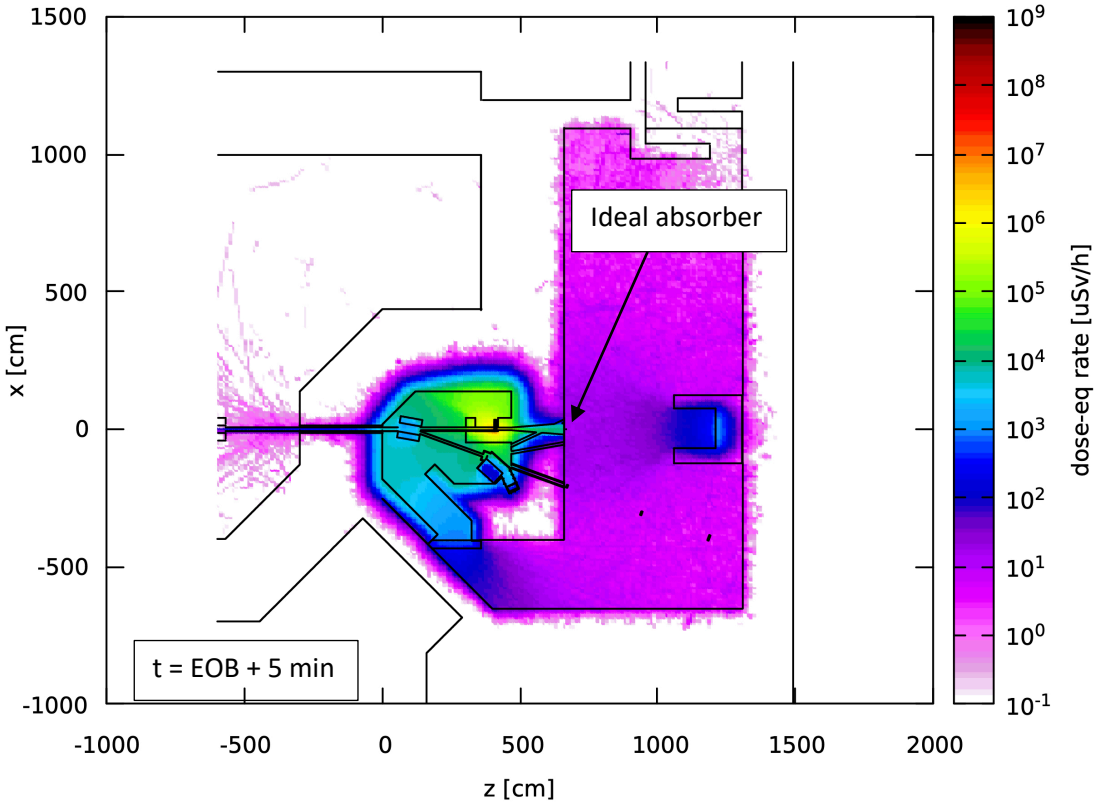

Figure 8.26 Map of the equivalent dose rate 5 minutes after the EOB produced by a proton beam impinging on the ANEM target (10 µA current, 5 days irradiation, y-range [-30,30]) with an ideal absorber at the end of the collimator. The contribution of the activated neutron absorber is clearly visible.

Despite this situation, after the end of an irradiation campaign, when the beam will be off for days or weeks, it is necessary that the experimental hall is freely accessible. According to the presented results, the highly activated concrete absorber continues to release significant amounts of radiation for days (Figure 8.27), before decreasing below the natural background (≈0.3 µSv/h). This requires the neutron absorber to be provided of a mobile shielding mechanism to close it, or a redesign of this object, using different materials, to mitigate the residual activation problem. The RESNUCLE card scores the radioactive nuclei at the EOB: in the concrete absorber the main contribution again comes from ^{24}Na. The persistent component that follows is negligible because below the natural background.

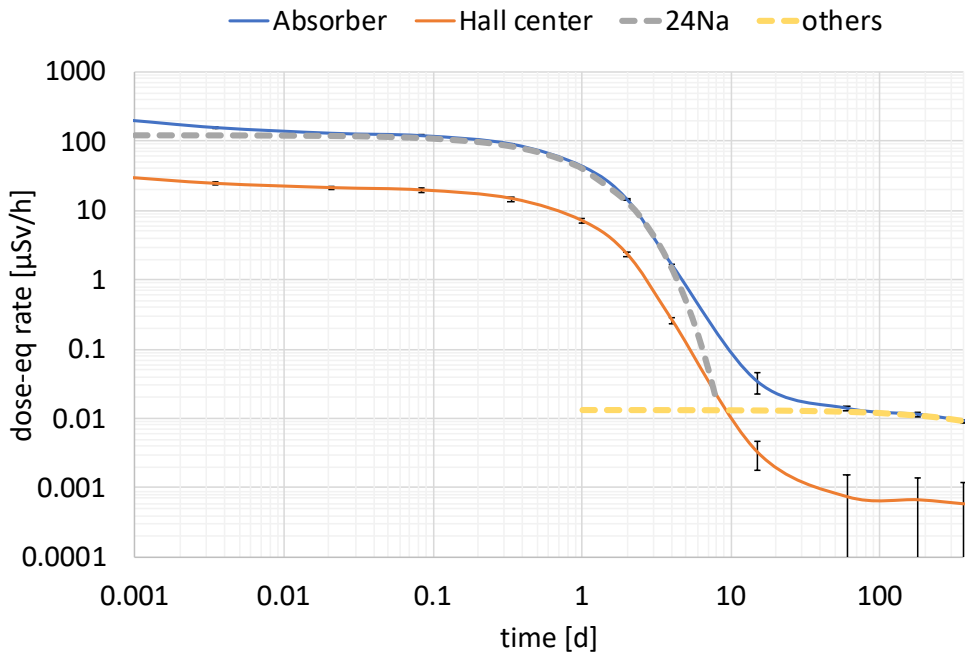

Figure 8.27 Equivalent dose rate as a function of time after the EOB for two different positions in the experimental hall (indicated in Figure 8.22). Contributions from different active nuclei are highlighted (grey and yellow lines). Errors are limited to few % until 10 days, then they increase due to lack of statistics in the hall center.

8.3.3 Future perspective

The results of the previous section show the need to foresee two shielding systems both for the collimator and the neutron absorber. The mechanism to move a lead shielding slab in front of the activated materials will be motorized: in case of engine failure, a worker, who accesses the experimental area 5 minutes after the EOB to manually close the slab, would get about 8 µSv in 10 minutes (avoiding direct view of the target), which is < 0.1% of the year dose limit for a type-B worker (6 mSv/year).

The FLUKA feature that allows to change the material of a region for radiation decay product transport with any material (lead in our case) is not implemented in the FLUKA version available when this work was carried on. The latest respin (released on 4th November 2019) adds this feature, however the implementation of these simulations is left to a future study.

The possibility to move on rails the entire absorber towards the collimator, closing them against each other, has also been considered. A FLUKA simulation of this kind would need a change in the geometry. This is possible assuming a “two-steps” approach: a first step for the production of the radionuclides (with the absorber located at the end of the experimental hall) and the

second step to score the dose rate due to their decay (with the absorber closed against the collimator). This procedure requires some custom-made routines that was developed during this work, but have not been validated yet, so further work is needed to obtain this result.

8.4 Shielding for the ANEM target: some hints

Another radiation protection issue is the activation of equipment and walls inside the bunker which hosts the production targets. The primary proton beam and the emerging neutron flux induce high amount of activation in the flood materials, in particular the target itself. Some simulations are performed exploring different solutions for shielding the ANEM target.

The primary beam is set as described in section 8.3.1 to calculate the activation of the composite ANEM target. A reasonable "physics year" for this beam line is 20 days of irradiation: to simulate a worst case scenario, calculations are performed with an irradiation profile of 20 continued days at the maximum current of 10 μA. The typical setup for activation studies (described in section 8.2.1) and dose-map scoring at different cooling times is implemented. The presence of water in the target cooling system is here ignored; it will give a contribution to dose rate [27], especially next to the circuit pipes, but this effect will be evaluated in the future, once the water circuit system is defined.

Different solutions for the local shielding of the ANEM target are explored. The simplest approach is to use a concrete (or lead) wall 40 cm thick leaving the "north" side free to allow air ventilation around the hot target (Figure 8.28). An alternative approach, inspired by the design of the SPES beam dump [29], is to use a 4π shielding system (see Figure 8.28) made of two concentric boxes of lead (5 cm thick) and polyethylene (30 cm thick) supported by a small concrete wall. This box is provided of a downward gap for forced air cooling.

The equivalent dose rate accumulated by the tally inside the bunker (shown in Figure 8.30) is plotted in Figure 8.29 for the three shielding solutions. They do not show a significantly different trend in time: in any case, the main contribution comes from ^{24}Na generated inside the concrete volume. The equivalent dose rate curve decreases below 10 μSv/h about 10 days after the EOB. For this reason, the access to the bunker should be forbidden for this time interval. Even though none of the considered solutions is much better than the others, the 4π-box solution offers an important advantage: the target can be moved together with its shielding, if it is necessary to extract it from the bunker for maintenance or to replace it with a new target. The persistent component of residual radiation could be reduced with an additional lead layer.

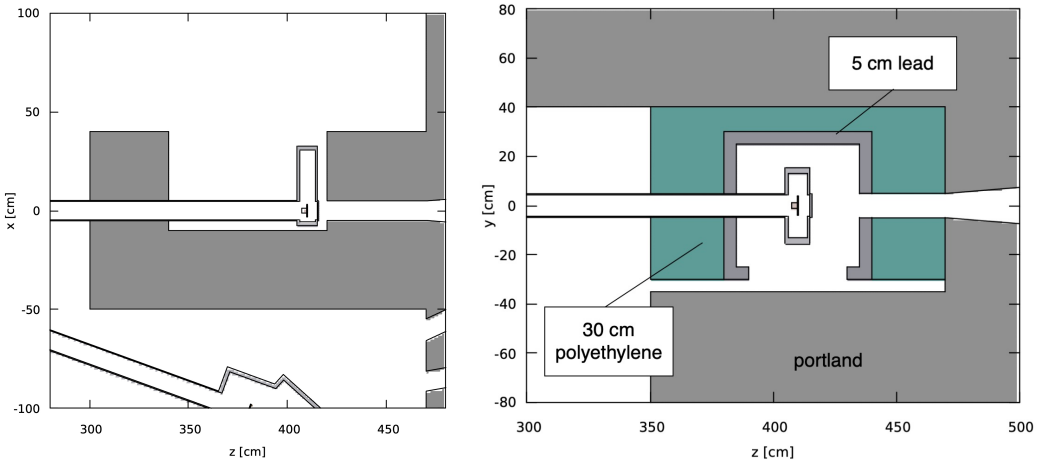

Figure 8.28 On the left, horizontal section of the wall design of the shielding system for ANEM. On the right, vertical section of the box-shielding design (supporting feet for the box are not shown). The proton beam comes from the left in an aluminum vacuum pipe connected to the target chamber.

In any case, if a short maintenance service is necessary inside the bunker (on systems far from the beam pipe, see Figure 8.30), this can be carried on 30 days after the EOB with an average accumulated dose, coming from the ANEM target, lower than 10 µSv/h. If this is not acceptable, further different solutions for a possible better shielding system for ANEM need to be studied.

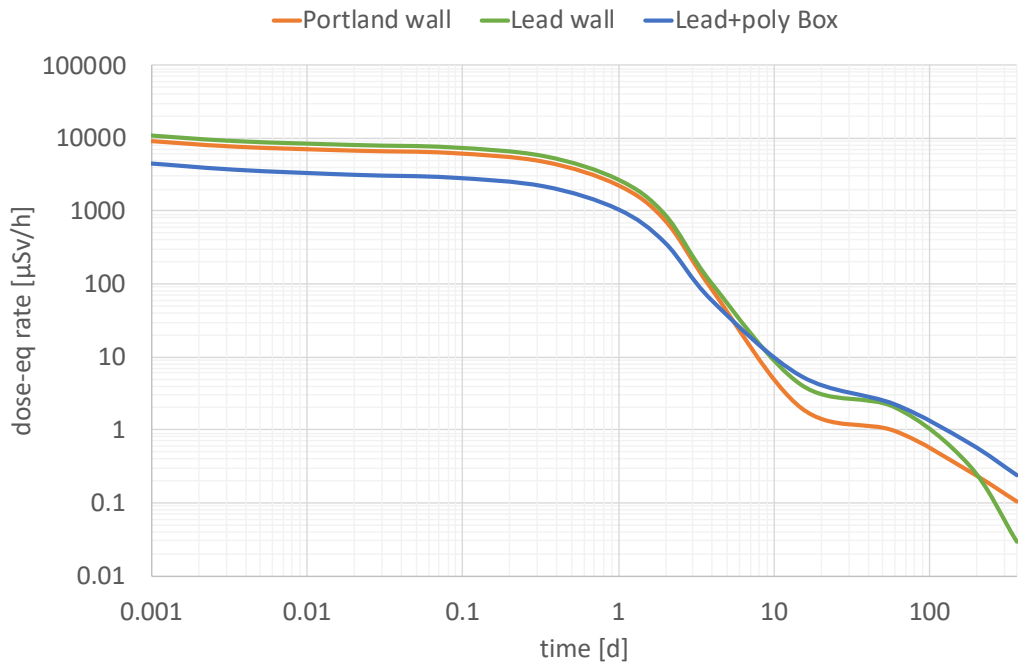

Figure 8.29 Equivalent dose rate trend in time after the EOB inside the bunker for three different shielding designs (20 days irradiation, 10 µA current). The position of the tally is indicated in Figure 8.30. Errors are lower than few %.

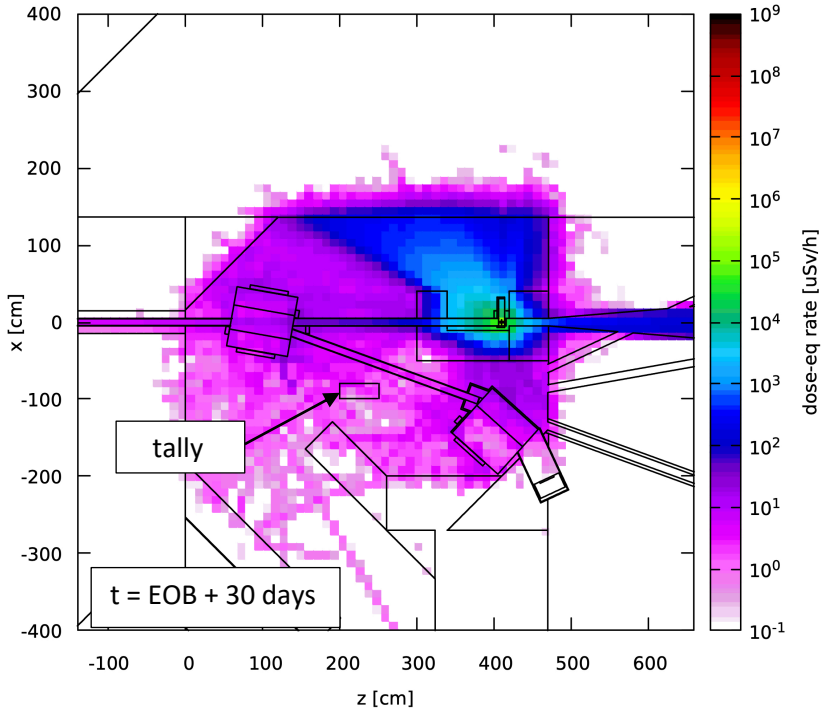

(a)

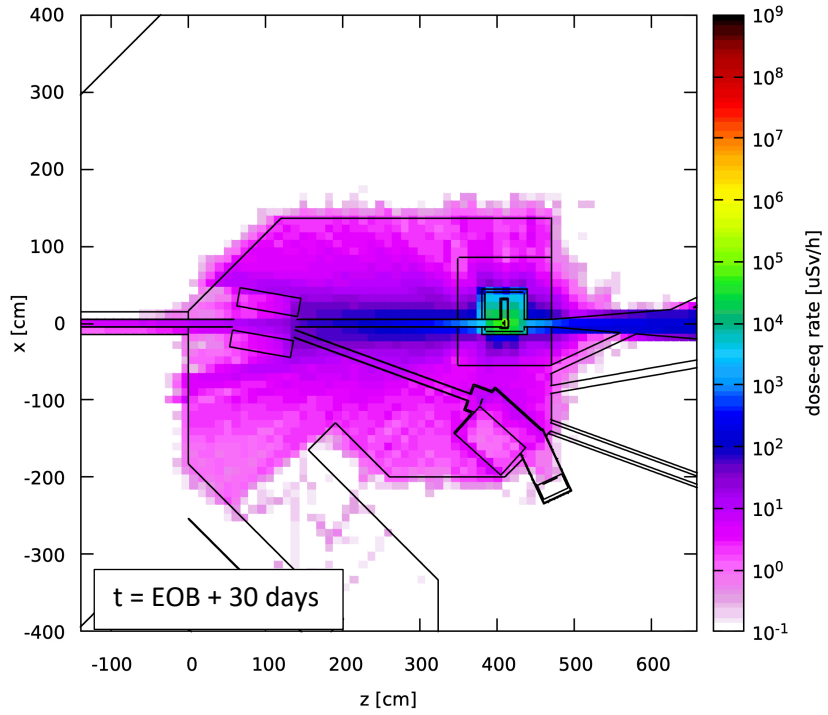

(b)

Figure 8.30 Map of the equivalent dose rate in the bunker 30 days after the EOB produced by a proton beam impinging on the ANEM target (10 μA current, 20 days irradiation, y-range [-30,30]). Two different shielding designs are reported: in (a) a Portland wall leaving one free side (the lead wall solution is very similar to this one) and in (b) a 360° box around the target made of lead and polyethylene. The indicated tally is used for the trend in time.

8.5 Quasi mono-energetic neutron beams

The QMN source of the NEPIR facility will use different proton beam energies and an assortment of thin Li targets (2-5 mm thick), to produce nearly mono-energetic neutrons at several discrete energies.

The resulting neutron energy spectrum in the forward direction is not purely mono-energetic: it does present a high energy peak few MeV below the energy of the impinging protons, but also a broad distribution at lower energy (tail), coming from nuclear breakup that accounts for ~60% of the total energetic neutron production; the thickness of the target influences the width of the quasi mono-energetic peak. The fraction of neutrons in the peak decreases rapidly with emission angle, while the continuous energy tail changes little: this behavior can be exploited to correct data taken in the forward direction by subtracting the effects due to neutrons in the wrong-energy tail, measured by taking data at larger angles [5]. This principle is shown in Figure 8.31.

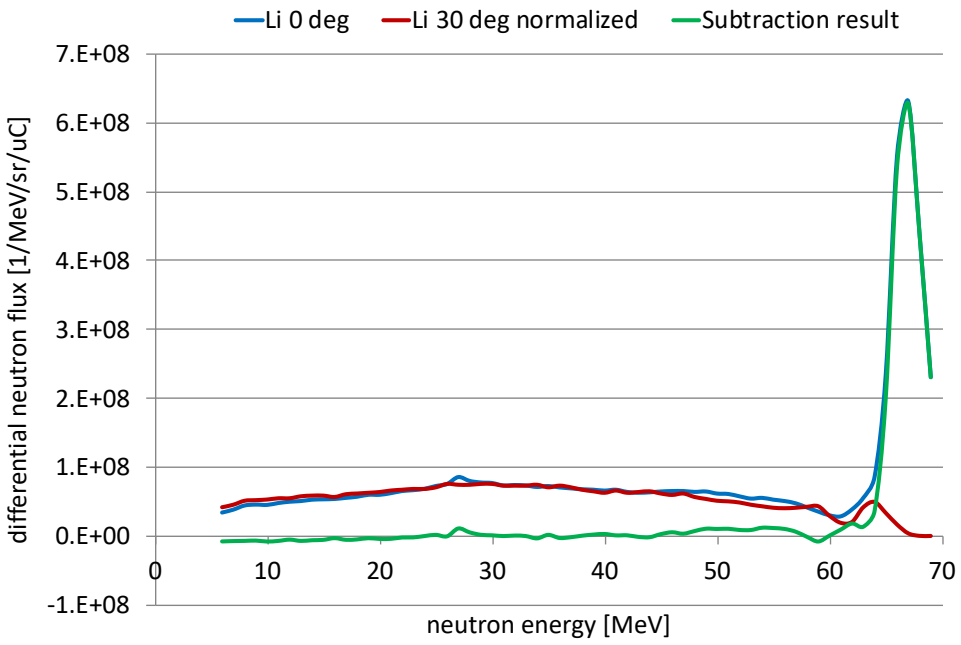

Figure 8.31 Correction (green) of quasi mono-energetic forward Li spectrum (blue) using 30° data with a normalization factor (red).

For energies below 70 MeV, the optimal angle for data correction will be experimentally determined: in this energy range, very few data are available in literature and Monte Carlo calculations are not entirely reliable [30].

At NEPIR, a 70 MeV 10 μA proton current on a 4.7 mm thick Li target is expected to produce a $\Phi \approx 2.3 \times 10^5$ n/cm^2/s flux of quasi mono-energetic neutrons at test point (3.10 m downward the target), under a peak with a FWHM smaller than 3 MeV.

8.6 QMN: a new slit collimator

The collimator system for the QMN target at the NEPIR facility is under study. The existing facilities implement two different approaches (Figure 8.32). At the iThemba Labs (South Africa), a static multi-angular system of cylindrical collimators is built into the wall and five different discrete angles are available, up to 16°. At RCNP (Japan), a more sophisticated system is implemented: the Li target station is movable along the curved proton trajectory inside a bending magnet (always being orthogonal to the beam) and a movable collimator, built into the front shielding wall, can follow the target, allowing to select any emission angle between 0° and 30°. The evident advantage of this approach is the possibility to continuously select the angle for the optimization of the tail correction. Moreover, an iThemba-style multi-angular collimator cannot be defined without reliable Monte Carlo simulations to calculate the optimal angles for the tail correction. On the contrary, the RCNP-like solution does not require this information and allows it to be experimentally determined.

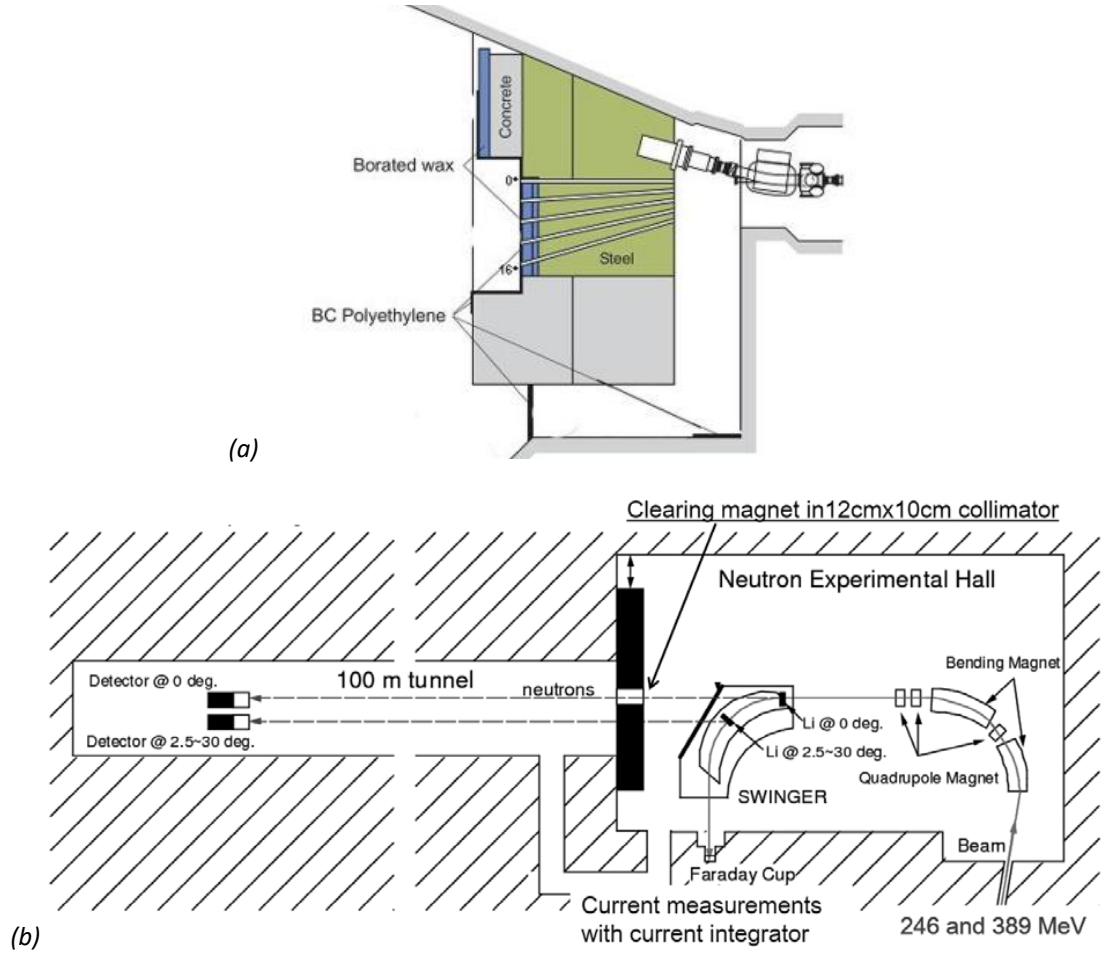

Figure 8.32 Two different collimator systems. In (a) the iThemba approach with a static multi-angular collimator made of multiple cylindrical collimators at fixed angles. In (b) the RCNP approach with a movable target and a single movable collimator to continuously select a specific emission angle.

For the NEPIR facility, a mixed solution is proposed: the Li target can be moved along the proton trajectory inside a bending magnet, while the collimator, built in the concrete wall, is static. However its section is rectangular, assuming the shape of a wide slit, allowing to continuously select an emission angle simply by translating the test point (Figure 8.33). The horizontal dimension of the slit (≈ 40 cm) is calculated to allow angle selection up to 45°. The vertical dimension, not yet defined, is discussed in section 8.6.2.

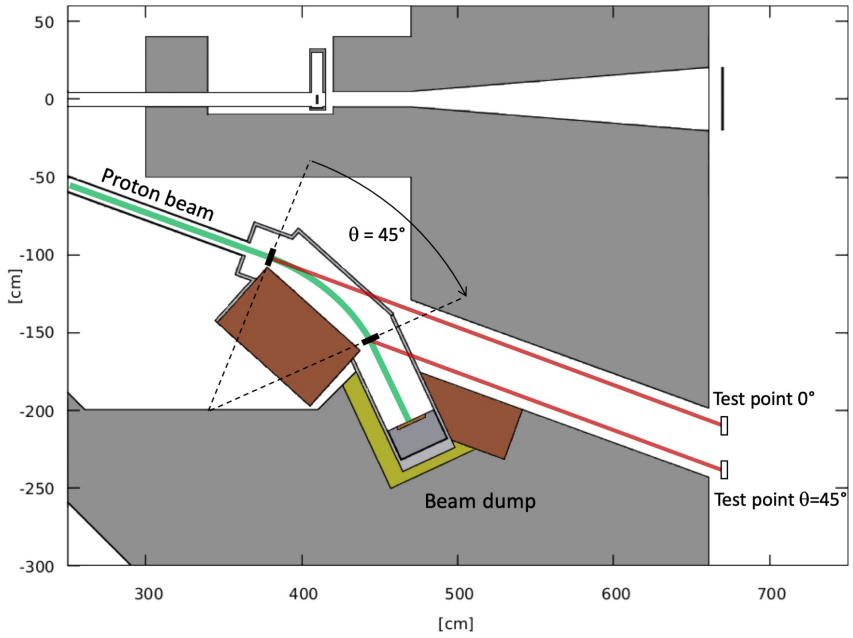

Figure 8.33 NEPIR-1 QMN collimator design. The proton beam comes from the left and enters a magnetic field which bends its trajectory: the Li target can move along this trajectory. The collimator consists in a slit, 40 cm large and 5-10 cm high: the position of the test point continuously selects an emission angle.

8.6.1 Effects of albedo neutrons

The contribution of albedo neutrons to the energy spectrum at the test point is studied using a source with a simplified energy distribution: a rectangular energy spectrum between 60 and 70 MeV. In the simulation, the neutrons are generated at a point centered at the Li target position and sent towards the collimator with a large divergence, in order to well illuminate the concrete wall that hosts the collimator. Downward the collimator, at the test point, a tally is set to score the neutron energy spectrum. An ideal collimator would introduce no changes in the energy distribution. A comparison between the results obtained from a 5 cm diameter cylindrical collimator and the described slit-like collimator (5 cm high) is presented in Figure 8.34. As expected, the energy distribution measured at the test point is not zero for energies below 60 MeV and this contamination is higher for the slit-like collimator than for the alternative cylindrical design. Nevertheless, it is meaningful especially below 55 MeV, where it can be

eliminated exploiting the subtraction method. At higher energies, where the monoenergetic peak of the QMN is located, this contamination is 2-3 order of magnitudes smaller than the amplitude of the peak and for this reason negligible. These results ensure that the neutron spectrum contamination is not a significant problem, so the slit-like collimator is a viable design. This solution does not need any movable collimator (pro), but it does not allow simultaneous measurements at different angles (con).

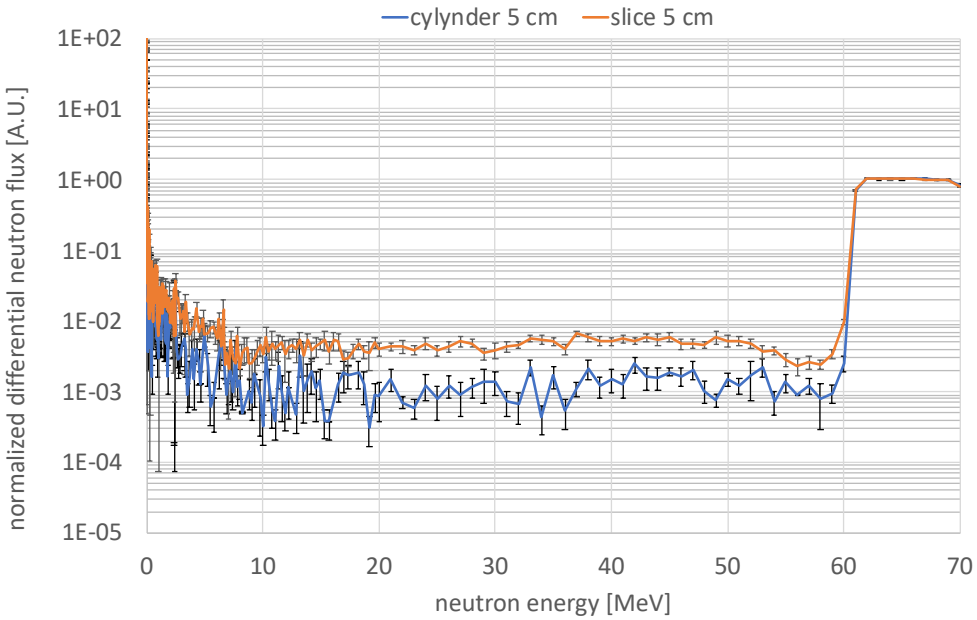

Figure 8.34 Cylindrical VS slit-like collimator: neutron spectrum contamination in the forward direction at the test point. Although in the central energy region the difference is conspicuous, the contamination always stays two order of magnitudes under the peak.

8.6.2 Air activation calculations

The effect of this collimator design on the activation of air in the experimental hall is also studied, in a way that resembles what was done in section 8.2 for air activation produced by the ANEM target. The QMN system is supposed to operate at a maximum proton current of 10 μA, but it is not expected to give particular activation problems since both the neutron yield and the acceptance of the collimator are considerably lower than in ANEM.

The thin target differential neutron yield is strongly angular dependent: the forward neutron spectrum is used in the simulation with a large divergence as a worst case scenario (being the hardest possible spectrum). The available experimental data are in the 7-70 MeV energy: since the component at lower energies can significantly contribute to the activation of air, the output

of an MCNPX simulation is used to build the custom source (FLUKA simulations do not match experimental data, see Figure 8.35).

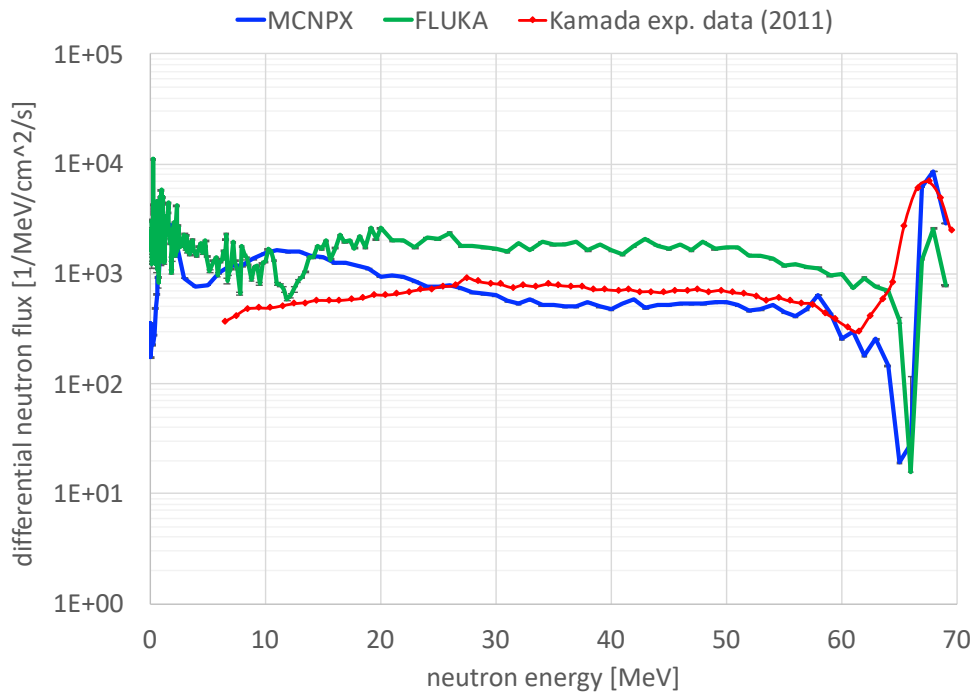

Figure 8.35 Thin Li neutron spectra at 3.10 m for 70 MeV protons (1 µA current): simulated (blue MCNPX, green FLUKA) and measured (red, [5]) data comparison.

A user-written routine is called to sample the energy of the primaries from the given distribution. The necessary cards are activated, as described in section 8.2.1. Again, the results are normalized to give the expected neutron flux at the test point; the distance between the target and the test point in the 0-degrees configuration is 3.10 m.

Three different values of the height of the slit collimator are here explored (5, 7 and 10 cm). The results (Figure 8.36) confirm that the air activation is not an issue, not even in the widest collimator configuration, and show the typical linear dependence on the collimator section area.

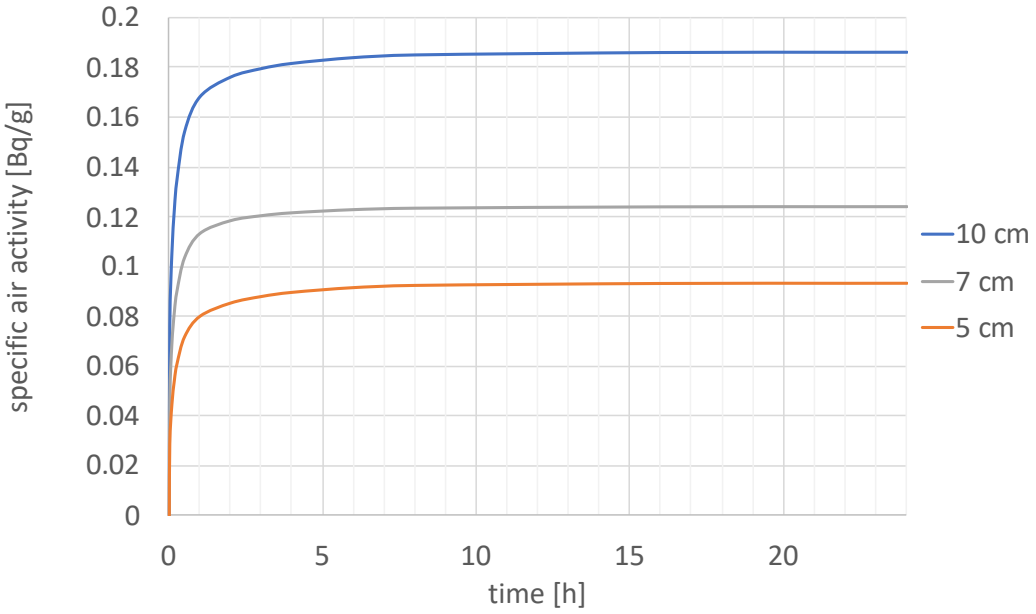

(a)

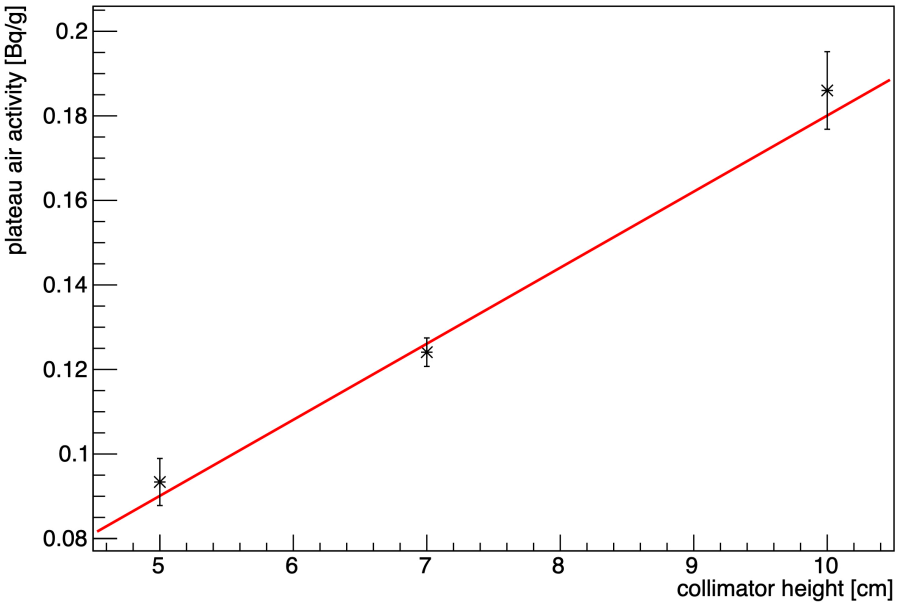

(b)

Figure 8.36 (a) Air activation build-up for different heights of the slit collimator (24-hours irradiation, 10 μA beam current). (b) QMN plateau air activity as a function of the slit height. Here, no errors on heights are reported since the geometry does not include approximations; ; errors on the activity include both a statistical term (< 4%) due to the simulations and a systematic term due to the normalization procedure (≈ 1%).

QMN target	
$A_\infty = m \cdot h + q$	
m [Bq/g/cm]	$(1.8 \pm 0.2) \times 10^{-2}$
q [Bq/g]	0.00 ± 0.01

Table 8-9 QMN plateau air activity A_∞ as a function of height h linear fit results (10 μA beam current).

8.6.3 Beam dump activation

At the QMN target station, the bending magnet is designed to curve the spent protons towards a beam dump. The slit collimator solution, compared to the cylindrical one, reduces in part the shielding between the beam dump and the collimator itself: this can be an issue since the beam dump is expected to be highly activated after an irradiation. At the present stage of design, the beam dump is made of a copper disk (2 cm thick) thermally connected to a water cooling system: impinging protons in Cu produce a high amount of gamma radiation and neutrons. A lead volume close to the Cu component is used to attenuate the electromagnetic radiation, whereas a polyethylene layer is added to slow down neutrons. The entire system is housed in a dedicated cave into the concrete wall of the bunker. In the simulated model, an iron block (more dense than concrete) is located between the beam dump and the collimator aperture to limit as much as possible the radiation from the beam dump directed towards the collimator.

The worst case scenario of a 10 µA beam current illuminating a 10 cm-high slit is simulated. In this case, the primary concern is the possibility for the user to access the experimental area in a reasonable time after the end of an irradiation session, for instance to change a DUT that underwent a catastrophic failure. Since, in this case, air will be exhausted, it is not included in the simulation, to avoid the contribution of its prompt activation.

In the simulation, a primary beam of protons is directed towards the thin Li target; a magnetic field of 1.1 T is activated (MGNFIELD card) and spent protons are directed towards the dump. The neutron spectrum generated by protons impinging on Li in FLUKA does not resemble the experimental one (as shown in Figure 8.35), but here the primary concern is the activation of the beam dump, mainly due to the proton beam. Many USRBIN cards are used to score the equivalent dose in a large region of space at different cooling times and produce residual activity maps of the experimental area and the target bunker (Figure 8.37). The equivalent dose rate, in the tally indicated as p1, is presented in Figure 8.38 as a function of the cooling time: its value quickly decreases below 20 µSv/h allowing a worker to enter the room and change the DUT getting less than 3 µSv in 10 minutes. Instead, at the end of an entire irradiation session, the collimator needs to be closed with a lead slab to make the experimental hall freely accessible in a short time.

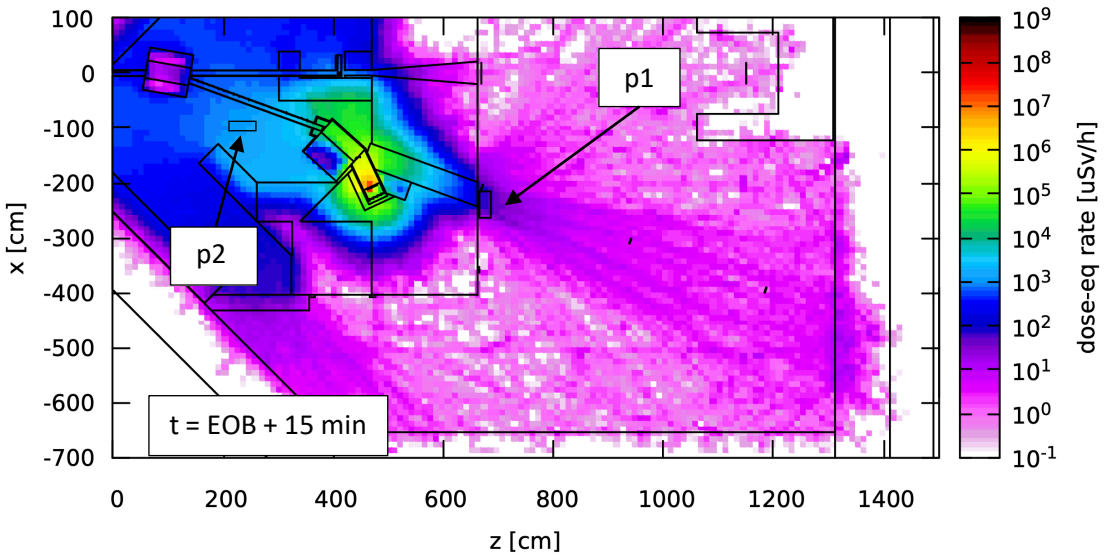

Figure 8.37 Map of the equivalent dose rate 15 minutes after the EOB produced by a 70 MeV proton beam impinging on a 4.7 mm Li target (10 µA current, 1 day irradiation, y-range [-10,10]). The indicated tally is used to score the trend in time.

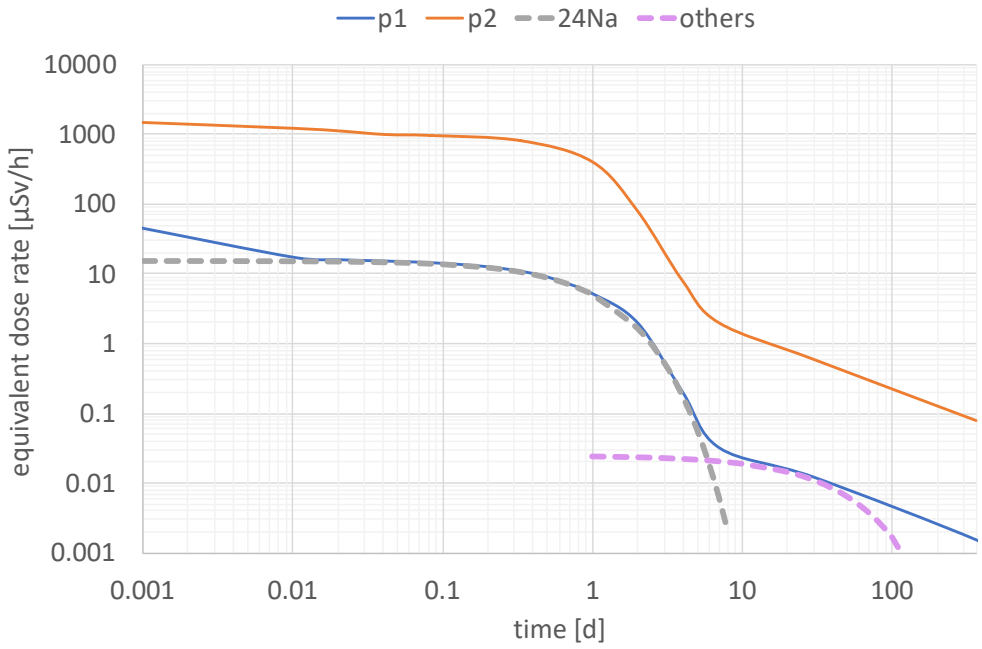

Figure 8.38 Equivalent dose rate trend in time after the end of an irradiation in two positions as indicated in Figure 8.37 (1 day irradiation, 10 µA current, 10 cm-high slit). Errors are < 5%. Calculated contributions from different active nuclei are highlighted.

The dose trend in time shows the signature of ^{24}Na which, outside the bunker, becomes negligible in a few days: this is an indication that the main problem remains the concrete activation due to neutrons. A simulation without the Li target (with the 70 MeV protons going directly onto the Cu beam dump) shows that actually the entire concrete activation is due to

neutrons produced by (p,n) reactions in the Cu disk, so the contribution of the neutrons from the thin Li target is negligible. The contamination in the spectrum at the test point, due to neutrons coming from the beam dump, is limited below 10 MeV. It is similar in each test position and can be subtracted out. Significant amounts of residual dose are expected inside the bunker caused by neutrons coming from the beam dump that are, in this case, difficult to shield. This problem is also related to the ANEM shielding system (here modeled as the simple concrete solution), since it is directly flooded by this neutron radiation and its activation properties are relevant for dose mitigation. At this stage of evaluation, a worker can access the bunker 4 days after the EOB getting less than 10 µSv/h.

8.6.4 A possible improvement

The contiguity of the QMN beam dump and the collimator aperture is in some way critical: here a possible different collimator design is proposed. The idea is to maintain a fixed test point and build a wedge collimator: in this way when the target is moved of an angle θ', at the test point the viewed emission angle is θ > θ' (see Figure 8.39).

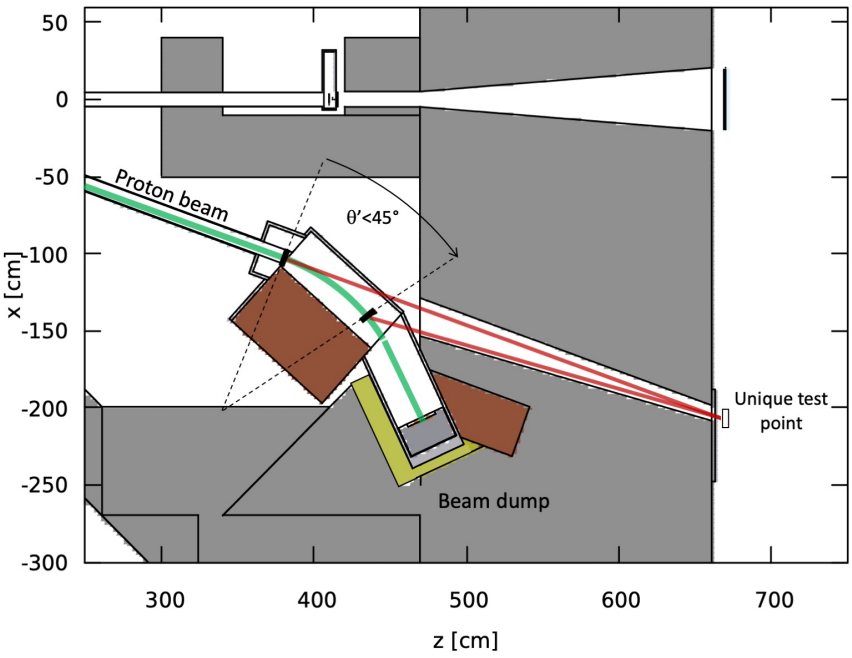

Figure 8.39 Proposed wedge collimator design. Considering a maximum required emission angle of 45°, with a unique test point, the Li target has to be rotated of an angle of 39° inside the bending magnet. The different shape of the collimator allows the distance between the beam dump and the collimator side to increase of 45%.

This system allows an average increase of 45% of shielding material thickness between the beam dump and the collimator aperture. A candidate material for further studies is iron, which can

eventually be also used to coat the inner side of the collimator. Additional polyethylene panels can be installed around the dump to decrease the neutron penetration in concrete and limit the activation due to ^{24}Na closer to the bunker-side surface. Moreover, also the addition of some neutron absorber materials inside the concrete mixture allows a reduction in the dose rate due to material activation (Table 8-10).

Method	**Dose rate reduction factor**
0.8 % B addition by weight	10
0.1 % B addition by weight	9
0.166 g/m^2 B coating	3
0.8 mm Cd coating	2.7

Table 8-10 Methods of reducing dose rates from activity induced in concrete [28].

9 NEPIR-0, the initial stage

NEPIR-0 is the initial, low cost stage of the development of NEPIR. It is completely funded and could be commissioned by 2022. In this stage, there is no independent target bunker in hall A9; a relatively simple thick beryllium white neutron target station is located inside the conduit leading the beam line through the cyclotron shield wall (3 m thick), separating the cyclotron hall from hall A9 (Figure 9.1), at 1 m from the cyclotron hall. Some supplementary shielding is provided at the back wall of hall A9 to absorb the neutron beam and, at the exit of the conduit, to reinforce the cyclotron shield wall.

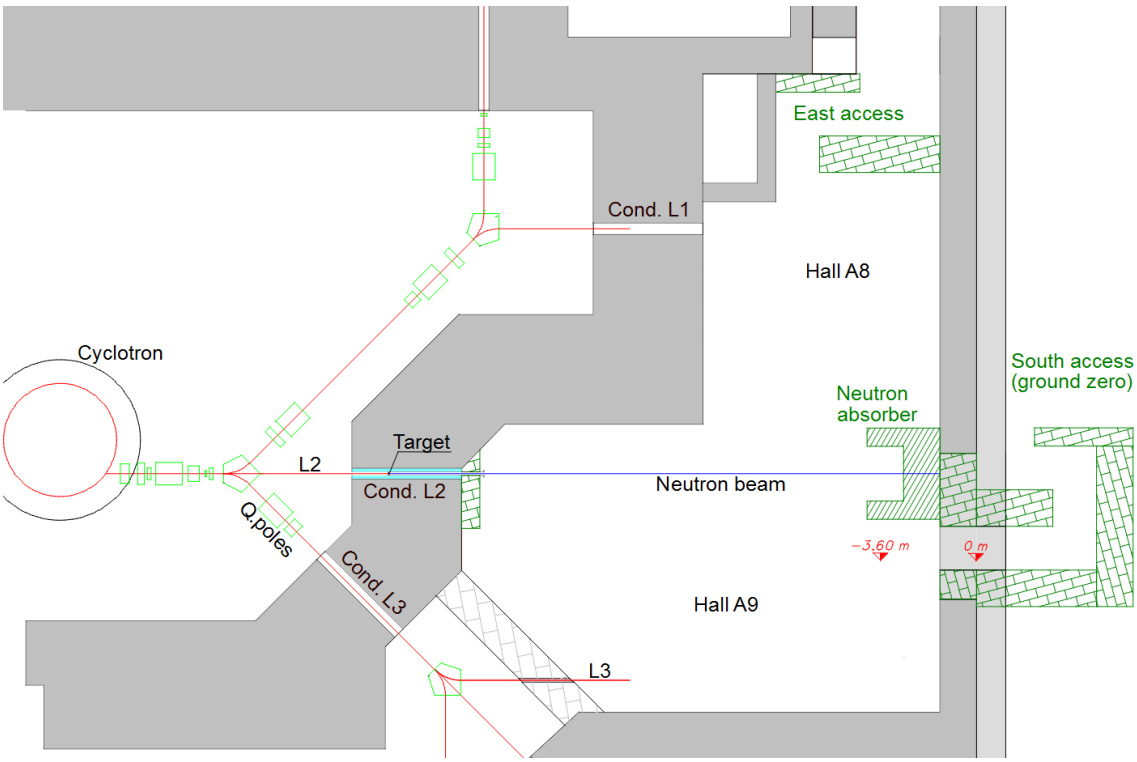

Figure 9.1 Schematic drawing of the floor plan for NEPIR-0. The cyclotron hall is visible on the left, the target is located inside the conduit L2 and the experimental hall is free. The building is partially underground, whereas the access maze on the right is at ground level.

The initial step is to get a measurable flux of neutrons in hall A9 in order to characterize the neutron spectra, using low proton currents. The working goal of NEPIR-0 is to use currents up to 1 µA to perform the activity for the Space Radiation shielding studies and to deliver useful neutron beams to industrial users who wish to characterize the neutron sensitivity of their electronic components and systems.

9.1 The NEPIR-0 neutron production target

The position of the target station is inside the conduit from the cyclotron hall to hall A9, at 260 cm from the test point, as shown in Figure 9.2. The proton vacuum line (Al, 10 cm diameter) passes through the conduit and is accessible through a flange in the experimental hall. The gap between the vacuum pipe and the conduit (30 cm diameter) is filled with High Density Polyethylene (HDPE) beads both to limit neutron propagation towards and from the cyclotron hall and to act as a collimator for the neutrons emitted towards the experimental area.

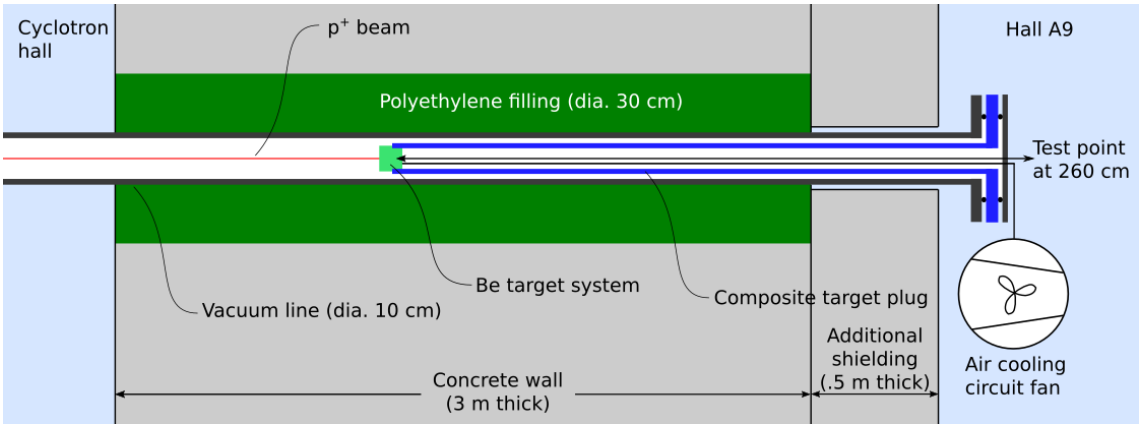

Figure 9.2 Schematic representation (vertical section, not to scale) of the plug holding the target of NEPIR-0, inside the wall (grey) separating the cyclotron hall and hall A9. In green the polyethylene filling housed in the space between the vacuum line and the wall.

A composite plug (shown in blue in Figure 9.2) is inserted into the beam line through the flange in hall A9, and holds the Be target and its cooling system. This plug is also evacuated by a dedicated pumping system.

At NEPIR-0 the 70 MeV proton current is limited to 1 μA, so initially a simple low power (< 100 W) Be cylinder (∅ = 30 mm, thickness = 30 mm) was considered, that could be cooled by a forced air circuit. However, Be is well known to be problematic, as proton irradiation eventually causes swelling: the formation of bubbles and defoliation cause risk of contaminating the cyclotron beam line or dispersing Be dust in the atmosphere. It is of paramount importance that the target be free to expand and that any debris be contained. For this reason, in the NEPIR-0 target design under development [31], the Be cylinder is immersed in a static bath of a liquid metal eutectic alloy of gallium, indium and tin, commercially known as Galinstan (Figure 9.3 and Figure 9.4).

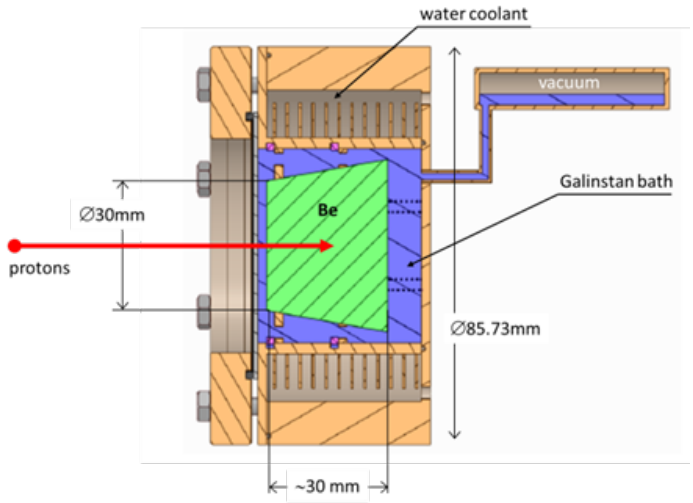

Figure 9.3 Schematic representation (vertical section) of the thick Be target being designed for NEPIR-0. The proton beam comes from the left, crosses a 25 µm thick Havar window (visible in Figure 9.4) and a 1 mm thick liquid alloy layer before it is stopped by the thick Be component (green). The Be is immersed in a Galinstan bath (purple) contained by a copper cladding.

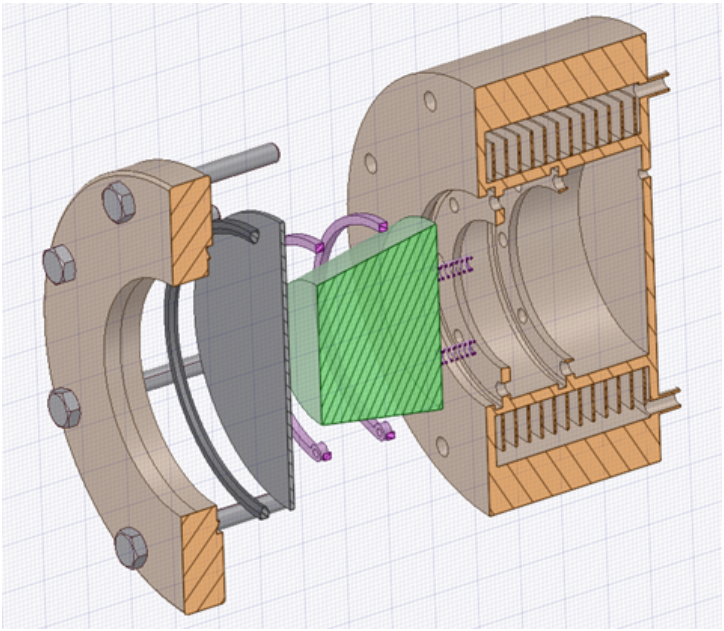

Figure 9.4 Exploded view of the NEPIR-0 target: the finned outer surface of the cladding and a matching copper outer layer define a cooling circuit. The surface of the cladding in contact with the coolant (flowing water) has cooling fins.

The liquid metal, contained by a copper cladding, ensures a good thermal contact with the Be and the internal surface of the Cu cladding, Au-coated to ensure tolerance to Galinstan (capable of eroding Cu). A 25 µm thick, robust Havar membrane separates the liquid metal from the beam line vacuum; this entrance window is cooled efficiently as it is in contact with the liquid metal. The outer surface of the cladding and a matching copper outer layer define a cooling circuit for

a flowing coolant. To improve heat exchange, the outer surface of the cladding has cooling fins. For coolant, water was chosen to allow for a more compact and reliable cooling circuit, with respect to air, suitable also for a higher power version of the target. The water flow in the enclosed circuit is ensured by input and output lines connected to a chiller outside the conduit, in the experimental area.

Figure 9.5 shows the MCNPX simulated neutron spectra for different values of the energy of the impinging protons: at the test point, just outside the conduit, for a 70 MeV proton current of 1 μA, the expected integral neutron flux in the 1-70 MeV energy range is 2.5×10^6 n/cm^2/s.

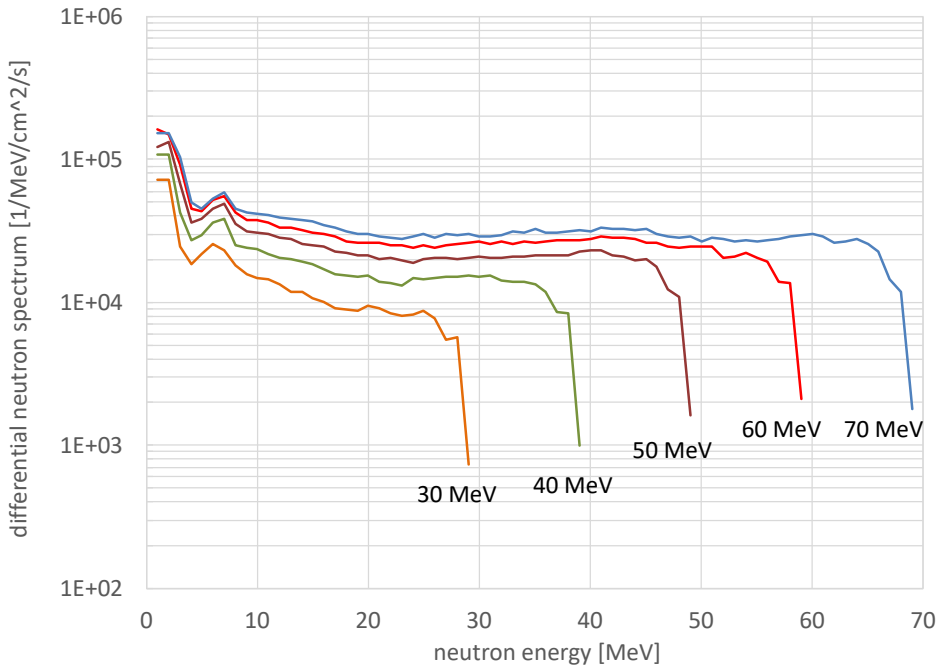

Figure 9.5 MCNPX calculated neutron yield of thick Be for different energies of the impinging proton beam (in the forward direction at 3 m, for 1 μA current).

The MCNPX-calculated energy distributions are somewhat flat, up to a sharp cutoff value close to the energy of the proton beam. This feature can be exploited to irradiate a sample with neutrons produced by proton beams with two different energies. By subtraction of the renormalized distributions, one can calculate the effects due only to the neutrons in the energy interval defined by the two cut-off values. An example is shown in Figure 9.6, where a neutron spectrum obtained by a 60 MeV proton beam is normalized and subtracted from the spectrum related to a 70 MeV proton beam. The effective neutron spectrum corresponds to a box-like distribution in the 55-69 MeV energy interval with an integral flux of 2.8×10^5 n/cm^2/s. The reliability of the spectrum shape is critical for this application, so extensive measurements will soon be performed with a Be sample.

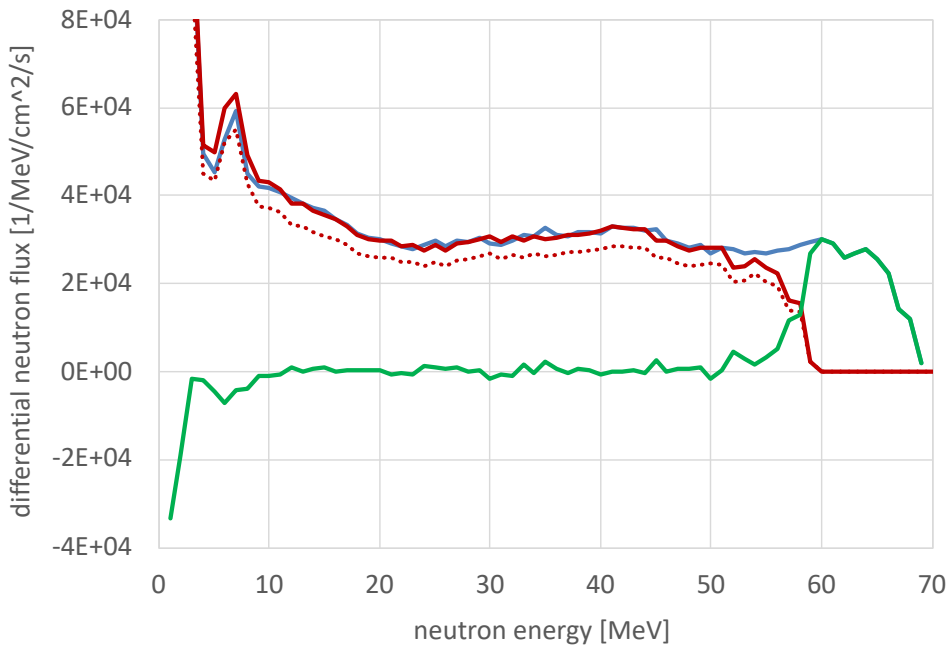

Figure 9.6 Effective neutron spectrum (green) obtained by subtraction of neutron energy spectra generated by 70 MeV (in blue) and 60 MeV (in dashed red) proton beams, the latter renormalized (in red) to match the first one tail.

9.2 NEPIR-0 air activation calculations

The problem of air activation is addressed in the NEPIR-0 configuration. The production target is shielded by concrete, with a total thickness of 250 cm, including the 50 cm additional shielding needed to further reduce prompt radiation (see Figure 9.2). The beam line and the surrounding material act as a neutron collimator to shape the neutron beam. With this design, the great majority of produced neutrons are absorbed inside the wall, but some of them can reach the surface and flood the experimental hall: this slow neutron component is very likely to induce air activation. The hall is not airtight, so again the limit of 1 Bq/g needs to be respected during the entire irradiation. In this case, compared to NEPIR-1, the advantages are a larger volume to dilute radionuclides (about 850 m^3) and a lower beam current (1 μA).

Air activation studies are addressed following the same procedure as in the previous chapter. Simulations are performed for the 70 MeV proton energy: a neutron custom source is used with the worst case scenario spectrum from Be (the one reported in Figure 9.5).

Three different collimator sizes are studied with the geometries shown in Figure 9.7. The 5- and 10-cm solutions need some High-Density polyethylene layers inside the beam pipe and the

former need also a more complicated extraction plug (not shown) since the hole in concrete is smaller than the beam pipe itself.

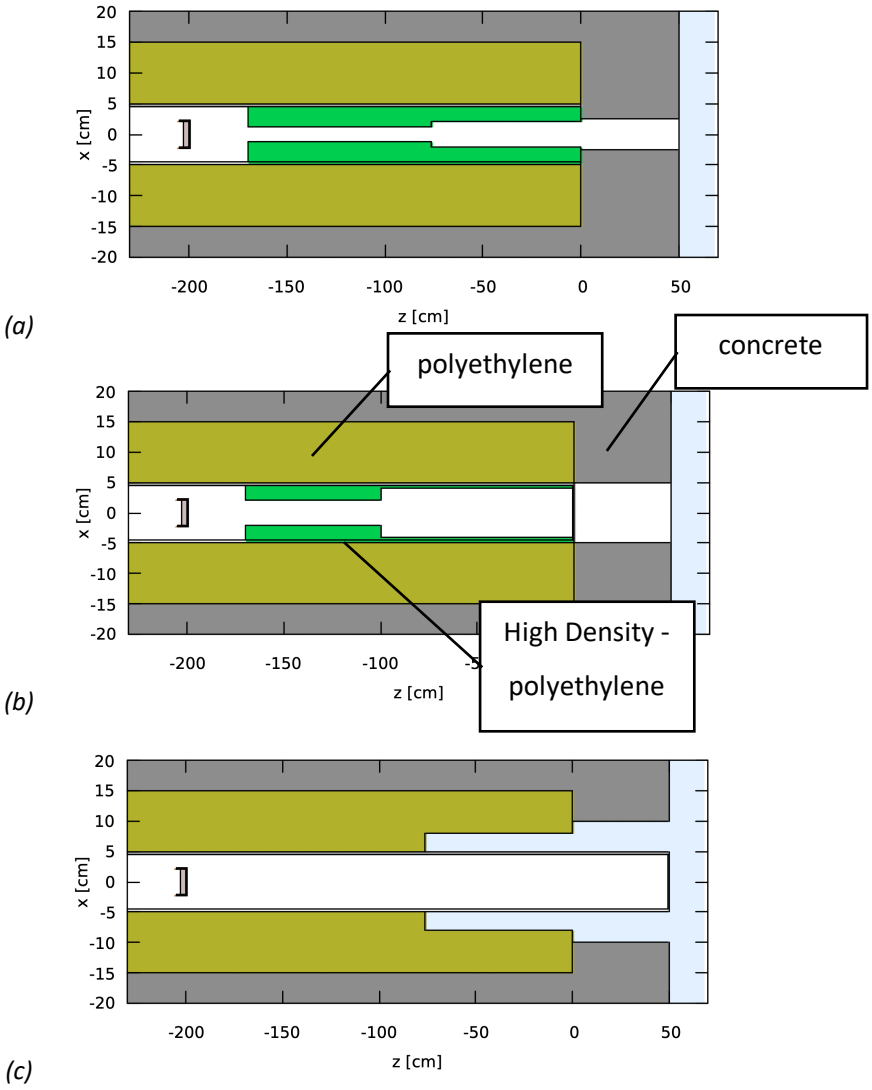

Figure 9.7 Schematic representation (vertical section, different horizontal and vertical scales) of three different collimator apertures of NEPIR-0: the diameters, 2.5 m downstream the target, are 5 cm in (a), 10 cm in (b) and 20 cm in (c). The proton beam comes from the left and interacts with the target producing radiation that is delivered to the experimental hall. In this study, the composite plug to hold the target is neglected.

The activation curves during the build-up period (24 hours) are shown in Figure 9.8: all three plateau levels are lower than the limit of 1 Bq/g, so this line does not present air activation problems. These results shows in particular that, for a 10-cm collimator, the activation of air is 3 times below the limit, which is a good safe margin.

In this analysis, the plateau activity value is not simply linearly correlated with the beam spot area at the test point (Figure 9.9). This effect is probably attributable to more substantial changes between different collimator solutions (e.g. different amounts of polyethylene).

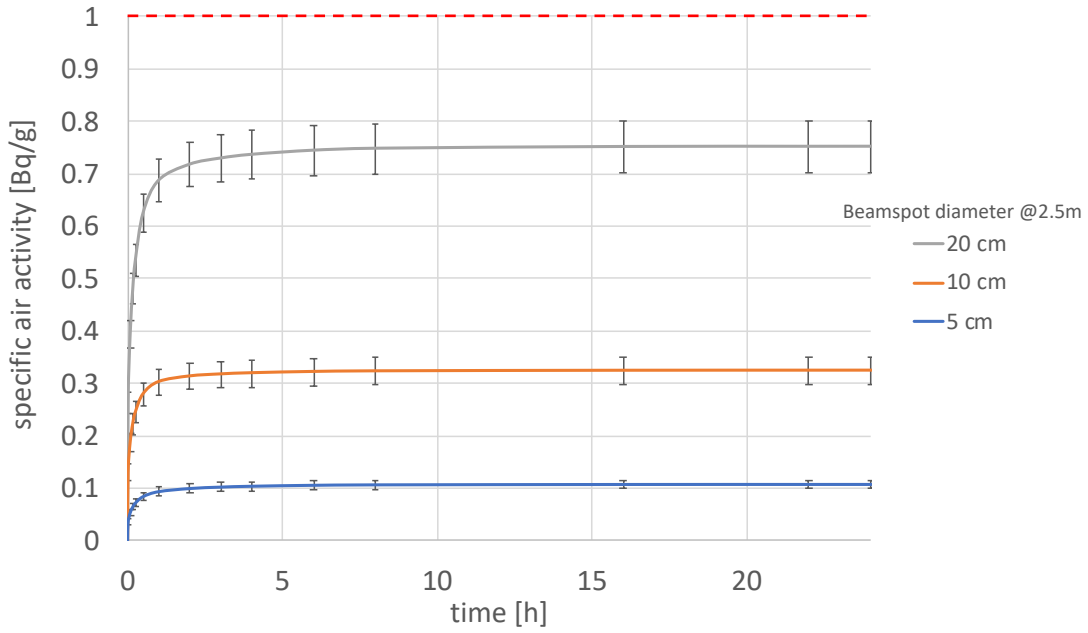

Figure 9.8 Air activation build-up with different collimator apertures (24h irradiation, 1 µA beam current). Errors are < 10%.

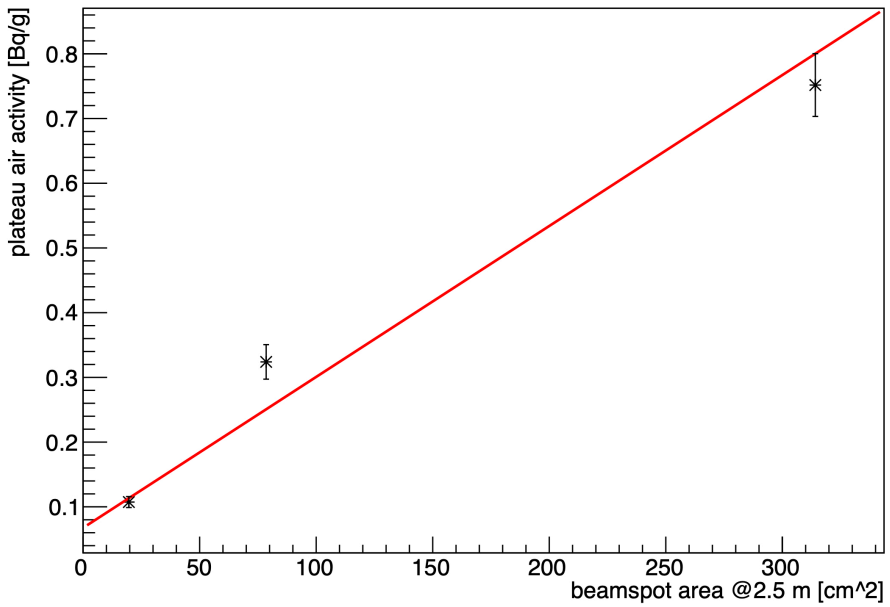

Figure 9.9 NEPIR-0 plateau air activity as a function of the beam spot area at the end of the collimator.

9.3 NEPIR-0 material activation studies

In NEPIR-0, the only activated materials are concrete walls around the target and the absorber at the end of the experimental hall. Simulations are performed with a proton beam impinging on the thick Be target and many USRBIN tallies are used to score the residual dose map after the EOB (Figure 9.10). As expected, the dose levels are significantly lower than those related to the targets previously presented in this work, mainly for the large reduction of the beam current.

Figure 9.11 shows the equivalent dose trend as a function of the cooling time (after 5 days of irradiation at 1 µA current). Again the main contribution comes from ^{24}Na and a residual contribution after 10 days is mainly attributable to the target (^{7}Be), but it is of negligible intensity. In this case, a user can change the DUT accumulating an equivalent dose of about 1 µSv/h; nevertheless, after an entire irradiation session, a lead shielding slab is needed to cover the collimator aperture, absorbing the most persistent radiation directed towards the test point, to ensure free and safe access to the room.

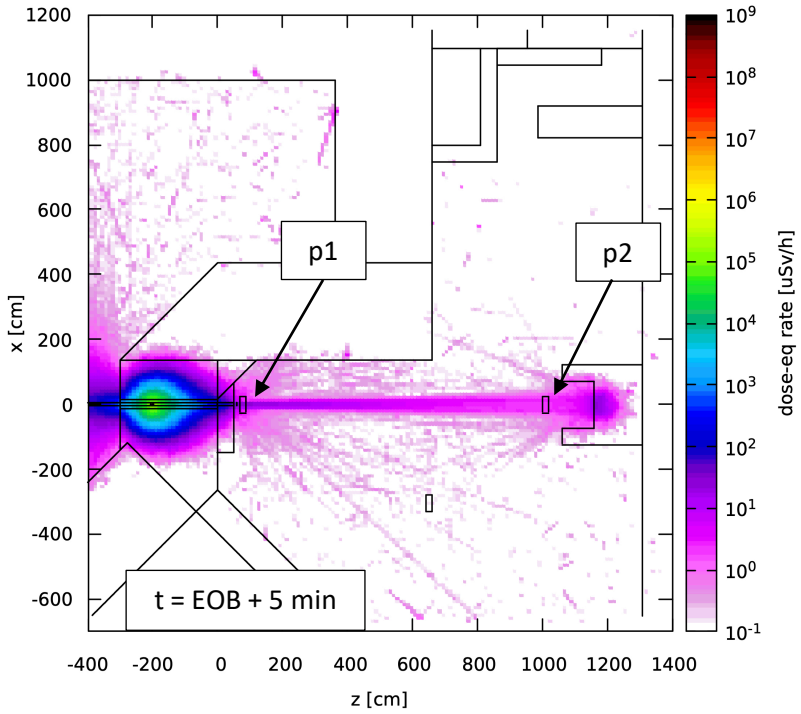

Figure 9.10 Map of the equivalent dose rate 5 minutes after the EOB produced by a 70 MeV proton beam impinging on the Be target (1 µA current, 5 days irradiation, y-range [-10,10]).

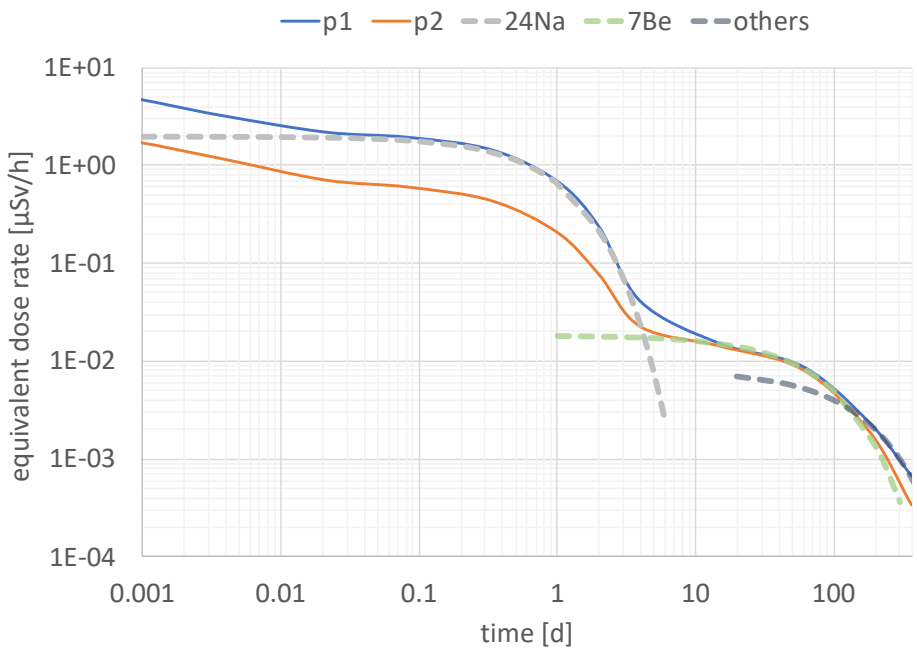

Figure 9.11 Equivalent dose rate trend in time for 2 different positions in the NEPIR-0 experimental hall (indicated in Figure 9.10). Errors are of the order of few %. Calculated contributions from different isotopes are highlighted.

10 Summary and conclusions

In this thesis some radiation protection issues of the NEPIR facility have been studied with the FLUKA Monte Carlo code, in both the initial NEPIR-0 and final NEPIR-1 configurations.

With what concerns NEPIR-1, the problem of air activation in the experimental hall due to the ANEM beam line has been extensively studied: since the hall is not airtight, the air activity inside it needs to stay below 1 Bq/g, which is the limit of radiological relevance. The ANEM system is designed to produce a neutron spectrum similar to the atmospheric one in the 1-65 MeV energy range: a 10 μA beam current is expected to ensure a maximum flux of 1.5×10^{7} n/cm^2/s at the test point, which is about 3×10^{9} times greater than the natural one at sea level, a very competitive acceleration factor. Different collimator apertures have been explored to reach this high neutron flux without exceeding the air activation limit: the upper limit for the collimator output diameter is 11.8 cm. This ensures a maximum beam spot diameter of 35 cm at the end of the experimental hall, which allows the irradiation of large electronic components and entire systems. The air activation study reveals the most problematic active nucleus to be ^{41}Ar, due to its half-life of 109 minutes. This is coherent with some experimental measurements performed in a similar environment. The air in the bunker is continuously collected by the SPES aspiration system, whereas in the experimental hall it is simply vented to the outside environment. In this way, after the beam shutdown, the main source of radiation resides in the activation induced in materials, especially objects which are directly invested by high neutron fluxes (bunker walls, neutron absorber, collimators, etc.).

The dose rate delivered to the experimental hall by the residual activation induced by the neutron beam has been evaluated. The main dose contribution is due to ^{24}Na produced in concrete by thermal neutron capture. However, in front of the collimator aperture, this effect is superimposed to a more persistent background attributable to the activation of the target itself. Simulations show the need to foresee a mobile shielding system, to close the collimator and the neutron absorber to ensure safe access to the room after the end of beam. Two motorized lead slabs can be used, or the absorber can slide on rails against the collimator wall, but further studies are needed before a final choice can be made.

Some simulations for the local shielding system of the ANEM target have also been performed. In this case, the dose inside the target bunker is evaluated at different cooling times to estimate reasonable conditions for the access. The problem of ^{24}Na in concrete is here limited: its contribution to dose, in fact, decreases rapidly between 1 and 10 days, a period of time in which

the access to the bunker must be forbidden. The residual dose after 10 days is more difficult to precisely assess, but all the three shielding solutions here explored have similar trends and limit this value below 10 μSv/h. In particular, the box-shielding made of lead and polyethylene allows one to get closer to the target getting a smaller amount of dose. Moreover, the box design can be mounted on a cart which would allow to take the target out of the bunker, together with its shielding, in case of replacement with a new one.

With regard to the collimator of the NEPIR-1 QMN beam line, the influence of a wide slit geometry on the neutron spectra at the test point is analyzed. The results show that the contamination is negligible: mainly limited to low energies and at least one order of magnitude lower than the neutron tail naturally produced by the QMN target. The air activation in the experimental hall is less problematic than in the ANEM case, since the neutron yield is lower and the collimator aperture smaller. The nominal maximum current of 10 μA can be safely reached: the air activation remains 3 times below the limit of 1 Bq/g for the 10-cm height collimator solution (which is currently the favorite). The dose delivered in the experimental hall after the end of beam is greatly influenced by ^{24}Na activity in concrete, the major source of high neutron fluxes being the proton beam dump, which is very close to the collimator. To mitigate this issue, a different collimator geometry is proposed, which increases of 45% the shielding between the beam dump and the collimator aperture. Further studies are anyway needed to optimize this system, starting from the shielding material composition.

The huge amount of active ^{24}Na in concrete have been shown to be problematic in many situations. This is a well-known problem at proton accelerator facilities, but its importance is always related to how long it is necessary to approach activated walls. A possible solution is the addition of small amounts of boron in the concrete aggregate to absorb thermal neutrons. Moreover, walls can be coated with special paints containing boron or cadmium. Inside the bunker, walls could also be covered by a layer of polyethylene that efficiently slows down neutrons with the subsequent production of many active ^{24}Na isotopes closer to the bunker surface: in this way, their contribution to dose would be increased inside the bunker (where the access will be forbidden) and decreased in the experimental hall (where a user needs to enter shortly after an irradiation to recover the irradiated device).

In this thesis, the simplified and fully funded NEPIR-0 configuration has also been studied. Studies of different collimator geometries show that air activation is not a problem with the nominal maximum current of 1 μA. The main contribution to remnant dose is again attributable to concrete activation and becomes negligible after 10 days. For this reason, it is necessary to

develop an activation shielding system (e.g. lead slabs) to close the collimator, to ensure a safe access to the room.

With the limited funds presently available, NEPIR-0 could be completed and commissioned by 2022. The rapid implementation and success of NEPIR-0 with users, academic and especially industrial ones, will catalyze further support in order to obtain the necessary funds to upgrade to the final configuration of NEPIR. Its first step will be the construction of a dedicated independent target bunker and air containment system, followed by the installation of the beam optics allowing the facility to deliver fast QMN beams. The novel and expensive ANEM target will be installed last, once the design is experimentally validated. The NEPIR facility would be a unique multidisciplinary facility in Europe, very useful for applied, industrial and basic research.

11 References

[1] JESD89A, "Measurement and Reporting of Alpha Particle and Terrestrial Cosmic Ray-Induced Soft Errors in Semiconductor Devices," JEDEC, 2006.

[2] M. S. Gordon et al., "Measurement of the flux and energy spectrum of cosmic-ray induced neutrons on the ground," *IEEE Transactions on Nuclear Science,* vol. 51, no. 6, pp. 3427-3434, 2005.

[3] S. Pomp et al., "High-energy quasi-monoenergetic neutron fields: existing facilities and future needs," EURADOS Report, 2013.

[4] S. Kamata et al., "Tail Correction in Quasi-monoenergetic Neutron Source," CYRIC Annual Report, 2005.

[5] S. Kamada et al., "Measurement of Energy-angular Neutron Distribution for 7Li, 9Be(p,xn) Reaction at EP = 70 MeV and 11 MeV," *Journal of Korean Physical Society,* vol. 59, no. 2, pp. 1676-1680, August 2011.

[6] E. J. Hall and A. J. Giaccia, Radiobiology for the radiologist, Lippincott Williams & Wilkins, 2012.

[7] ICRP, "The 2007 Recommendations of the International Commission on Radiological Protection," ICRP Publication 103, 2007.

[8] C. L. Dunford and T. W. Burrows, "Online Nuclear Data Service," IAEA, Vienna, 1995.

[9] A. Ferrari, P. Sala, A. Fassò and J. Ranft, *FLUKA: a multi-particle transport code,* CERN 2005-10 (2005), INFN/TC_05/11, SLAC-R-773.

[10] G. Battistoni et al., "Overview of the FLUKA code," *Annals of Nuclear Energy,* vol. 82, pp. 10-18, 2015.

[11] A. Fassò, A. Ferrari and P. R. Sala, "Radiation transport calculations and simulations," *Radiation Protection Dosimetry,* vol. 137, no. 1-2, pp. 118-133, 2009.

[12] X-5 Monte Carlo team, "MCNP - A General Monte Carlo N-Particle Transport Code, Version 5," 2003.

[13] V. Vlachoudis, "FLAIR: A Powerful But User Friendly Graphical Interface For FLUKA," in *Proceedings of International Conference on Mathematics, Computational Methods and Reactor Physics*, New York, 2009.

[14] M. Brugger et al., "Benchmark studies of induced radioactivity produced in LHC materials, part I: specific activities," *Radiation Protection Dosimetry,* vol. 116, no. 1-4, pp. 6-11, 2005.

[15] M. Brugger et al., "Benchmark studies of induced radioactivity produced in LHC materilas, part II: remanent dose rates," *Radiation Protection Dosimetry,* vol. 116, no. 1-4, pp. 12-15, 2005.

[16] A. Infantino et al., "Experimental measurement and Monte Carlo assessment of Argon-41 production in a PET cyclotron facility," *Physica Medica,* vol. 31, pp. 991-996, 2015.

[17] D. B. Pelowitz et al., "MCNPX 2.7.A Extensions," LANL, 2011.

[18] T. Aoki et al., "Measurement of Differential Thick-Target Neutron Yields of C, Al, Ta, W(p,xn) Reactions for 50-MeV Protons," *Nuclear Science and Engineering,* vol. 146, no. 2, pp. 200-208, 2004.

[19] H. I. Amols et al., "Physical characterization of neutron beams produced by protons and deuterons of various energies bombarding beryllium and lithium targets of several thicknesses," *Medical Physics,* vol. 4, no. 6, pp. 486-493, 1977.

[20] M. Osipenko et al., "Measurement of neutron yield by 62 MeV proton beam on a thick beryllium target," *Nuclear Instruments and Methods in Physics Research A,* vol. 723, pp. 8-18, 2013.

[21] J. Won Shin et al., "Neutron spectra produced by 30, 35 and 40 MeV proton beams at KIRAMS MC-50 cyclotron with a thick beryllium target," *Nuclear Instruments and Methods in Physics Research A,* vol. 797, pp. 304-310, 2015.

[22] Y. Uwamino et al., "Semi-monoenergetic neutron field for activation experiments up to 40 MeV," *Nuclear Instruments and Methods in Physics Research A,* vol. 271, no. 3, pp. 546-552, 1988.

[23] M. A. Lone et al., "Thick target neutron yields and spectral distributions from the 7Li(p/d, n) and 9Be(p/d, n) reactions," *Nuclear Instruments and Methods,* vol. 143, no. 2, pp. 331-344, 1977.

[24] S. M. Valle et al., "The MONDO project: A secondary neutron tracker detector for particle therapy," *Nuclear Instruments and Methods in Physics Research A,* vol. 845, pp. 556-559, 2017.

[25] G. Vidale, "Prestazioni della targhetta rotante dell'esperimento NEUTARGS," *Bachelor degree thesis,* 2015.

[26] "ANSYS® Academic Research, Release 15.0".

[27] W. P. Swanson and R. Thomas, The dosimetry of ionizing radiation, vol. 3, K. R. Kase et al., Ed., Academic Press, 1990.

[28] IAEA, "Radiological safety aspects of the operation of proton accelerators," IAEA, Vienna, 1988.

[29] M. Maggiore et al., "Status of the high intensity beam facility at LNL-INFN," in *Proceedings of Cyclotrons*, Zurich, 2016.

[30] D. Bisello et al., "The QMN beam line of the neutron-induced Single Event Effects facility at the 70 MeV cyclotron of LNL-INFN," *Physics Procedia,* vol. 60, pp. 271-277, 2014.

[31] R. A. Barrera et al., "CoolGAL: a Galinstan bathed Be fast neutron production target at the NEPIR facility," *submitted for publication to EPJ Web of Conferences,* UCANS8 conference proceedings, Paris, 8-11 July 2019.

[32] J. E. Martin, Physics for radiation protection, Wiley, 2006.

[33] M. Baba et al., "Characterization of a 40-90 MeV 7Li(p,n) neutron source at TIARA using a proton recoil telescope and a TOF method," *Nuclear Instruments and Methods A,* vol. 428, pp. 454-465, 1999.

[34] A. Fassò, A. Ferrari, J. Ranft and P. Sala, "FLUKA-2011 manual," CERN, 2011.